PDF Simulations of Auto-Ignition in Internal Combustion Engines

Zur Erlangung des akademischen Grades
Doktor der Ingenieurwissenschaften
der Fakultät für Maschinenbau
Karlsruher Institut für Technologie (KIT)
genehmigte

Dissertation

von

M.Sc. Ahmed Zoweil

aus Alexandria, Ägypten

Tag der mündlichen Prüfung:	10. Juli 2013
Hauptreferent:	Prof. Dr. rer. nat. habil. Ulrich Maas
Koreferent:	Prof. Dr.-Ing. Ulrich Spicher

Institut für Technische Thermodynamik

Prof. Dr. rer. nat. habil. U. Maas

Abstract

Considering the fundamental role that internal combustion engines play in human life today, it is recognized as one of the most important inventions in the history of mankind. The nature of the combustion processes in the internal combustion engines in terms of turbulent fluctuations and cycle-to-cycle variations provide a strong motivation for adopting stochastic approaches in modeling these processes. In this context, a new methodology for modeling auto-ignition in internal combustion engines has been developed. The methodology is based on solving the transport equation of the joint probability density function (PDF) of the velocity and scalars. The transported PDF approach applies the Lagrangian Monte Carlo method, as a particle method, for generating the statistical distribution in the computational domain.

Due to the dominant role that the chemical kinetics play in controlling the auto-ignition process, the PDF method provides a major advantage because of its ability to incorporate the chemical kinetics in a closed form. Molecular transport is being modeled using different standard turbulent mixing models. The statistical fluctuation of temperature due to heat transfer to the walls of the combustion chamber as well as mass loss due to the engine blow-by effect are also taken into account.

In spark ignition engines, the tendency for knocking has a major influence on the efficiency of the engine. Providing a better understanding and prediction of engine knock will assists engineers to enhance the performance of the SI engine in terms of fuel consumption and pollution control. A multi-zone PDF model has been developed for the simulation of engine knock in a two-stroke engine. The model considers only the end-gas region where the phenomenon of engine knock takes place.

Furthermore, this approach has been applied for modeling the combustion process in the homogeneous charge compression ignition (HCCI) engines. The concept of the HCCI engine is very promising because it combines the advantages of both spark ignition (SI) and compression ignition (CI)engines providing higher efficiencies while maintaining low particle and NO_x emission levels. Still, there are difficult challenges prohibiting HCCI from being adopted in industrial operation such as extending the operational range and controlling the combustion process.

For this purpose, a hybrid CFD-PDF model has been developed. Using different detailed chemical kinetic mechanisms, a gasoline-fueled two-stroke as well as diesel-

fueled four-stroke HCCI engines have been simulated. The validation of the hybrid CFD-PDF model has been done by comparing the pressure curves resulting from the simulation to the experimental measurements showing a very good agreement.

The study of the HCCI engine has been extended to investigate the influence of the variation of several operational parameters (initial temperature and fluctuations of the fresh gas mixture, exhaust gas recirculation, etc.) on the characteristics of the ignition and combustion process.

Kurzfassung

In Anbetracht der grundlegenden Rolle, die der Verbrennungsmotor im menschlichen Leben heutezutage spielt, ist er als einer der wichtigsten Errungenschaften in der Geschichte der Menschheit anerkannt. Die Eigenschaften der Verbrennungsvorgänge in Verbrennungsmotoren in Bezug auf die turbulenten Fluktuationen und Zyklus-zu-Zyklus Variationen bieten eine starke Motivation für die Annahme stochastischer Ansätze zur Modellierung dieser Prozesse. In diesem Zusammenhang ist eine neue Methodik zur Modellierung der Selbstzündung bei Verbrennungsmotoren entwickelt worden. Diese Methodik basiert auf der Lösung der Transportgleichung für die Wahrscheinlichkeitsdichtefunktion (PDF) für die Geschwindigkeit und Skalare. Hierbei wird die sogenannte Monte Carlo-Methode verwendet, welche als Teilchenverfahren zum Erzeugen einer statistischen Verteilung der turbulenten Vorgänge geeignet ist.

Aufgrund der dominanten Rolle, die die chemische Kinetik bei der Selbstzündung spielt, bietet die PDF-Methode den Vorteil die Reaktionen in geschlossener Form zu integrieren. Die turbulenten und molekularen Mischungsprozesse werden durch sogenannte Mischungsmodelle angenähert. Die statistischen Fluktuationen des Skalarfeldes, der Wäremetransport durch die Wände des Verbrennungsraumes und der Masseverlust durch Blow-by werden ebenfalls berücksichtigt.

In Ottomotoren hat die Tendenz für das Motorklopfen einen großen Einfluss auf den Wirkungsgrad des Motors. Ein genaues Verständnis und die Vorhersage des Motorklopfens erlaubt Ingenieuren, die Leistung des Ottomotors bezüglich der Verbesserung des Kraftstoffverbrauchs und des Umweltschutzes zu erhöhen. Ein Mehrzonen PDF Modell wurde entwickelt für die Simulation des Motorklopfens in einem Zweitakt-Motor. Das Modell berücksichtigt dabei nur die Endgasregion, wo das Motorklopfen iniziiert wird.

Darüber hinaus wird dieser Ansatz zur Modellierung des Verbrennungsprozesses für "Homogeneous Charge Compression Ignition" (HCCI) Motoren angewandt. Das Konzept des HCCI-Motors ist sehr vielversprechend, da er die Vorteile von Otto- und Diesel-Motoren kombiniert. Der HCCI-Motor bietet einen höheren thermischen Wirkungsgrad, verbunden mit niedrigen Partikel-und NOx-Emissionen. Dennoch gibt es schwerwiegende Herausforderungen die den Einsatz des HCCI-Motors Serienanwendungen verhindert, wie z.B. deutlich verkleinerte Betriebspunktbereiche (Last, Drehzahl) und die Steuerung des Verbrennungsprozesses.

Zu diesem Zweck wurde ein hybrides CFD-PDF-Modell entwickelt. Mit verschiedenen detaillierten chemischen Mechanismen wurde ein mit Benzin betriebener Zweitakt- als auch ein mit Diesel betriebener Viertakt-HCCI-Motor simuliert. Die Validierung des hybriden CFD-PDF-Modells wurde durch den Vergleich der jeweiligen Druckverläufe aus der Simulation und experimentellen Messungen vorgenommen und zeigt gute Übereinstimmung.

Die Studie des HCCI-Motors wurde erweitert, um den Einfluss verschiedener Betriebsparameter (Anfangstemperatur und Fluktuationen des Frischgases, Abgasrückführung (AGR), etc.) auf den Zünd- und Verbrennungsprozess zu untersuchen.

Contents

Notation

Latin Symbols

Symbol	Description
a_i	Drift factor for particle velocity
A_{geo}	Geometrical cross section of the ring clearance of the piston
b_j	Drift factor for particle scalar
B	Constant in the Langevin velocity model
B_{cyl}	Bore diameter of the combustion chamber
c,	Velocity scale model constant
C,	Dimensionless constant of probability for turbulent viscosity model
C_o	Kolmogorov constant
C_3, C_4	Constants of the Hohenberg model for heat transfer coefficient
C_m	Average piston speed
C_μ	Constant for k-ϵ turbulence model
$C_{\epsilon 1,\epsilon 2}$	Constants for k-ϵ turbulence model
C_p	Specific heat capacity at constant pressure
$\overline{C_p}$	Mean specific heat capacity at constant pressure
$C_{\epsilon 1}, C_{\epsilon 2}$	Model constants for the ϵ equation
C_ϕ	Turbulent mixing model constant
D^u	Diffusion factor for particle velocity
D^j	Diffusion factor for particle scalar
E_A	Activation energy of a chemical species
$E\langle\phi\rangle$	Mathematical expectation of a random variable ϕ
f_ϕ	Probability density function
$f_{u,\phi}$	Joint probability density function of velocity and scalars
$f_{u\|\phi}$	Marginal probability density function of velocity at constat ϕ
F_ϕ	Distribution function of a random variable ϕ
$F_{U\phi}$	The mass density function of a random variable
F_N	Discrete mass density function
G_{ij}	Model constant in Langavin velocity model
h	Specific enthalpy
$\widetilde{h''}$	Density-averaged specific enthalpy fluctuation
J	Molecular diffusion flux density

k	Turbulent kinetic energy
ℓ, ℓ_m	Characteristic length scales
$\dot{m}_l$	Blowby mass flow rate
M	Total mass of particles
$\overline{M}$	Mean molar mass
M_θ	Molecular mass of species θ
ΔM	Mass of a single particle
n	Number of chemical species
N	Number of stochastic particles
N_s	Number of mixing stochastic particles pairs
P	Pressure
P_k	Production rate of the turbulent kinetic energy
$P(\psi)$	Probability of the random variable ψ
Pr	Prandtl number
$\dot{q}$	Heat flux
Q_ϕ	Function of a random variable ϕ
$\underline{r}$	Position vector
r	Crank radius
R	Universal gas constant
Re	Reynolds number
S_h	Source term of enthalpy
S_α	Piston Displacement
S_θ	Source term of a chemical species
Sc_k	Turbulent schmidt number for k
Sc_ϵ	Turbulent schmidt number for ϵ
t	Time
T	Temperature
T_{p_t}	Particle temperature
T_{wall}	Combustion chamber wall temperature
u_i'	Velocity fluctuation with respect to $\langle U_i \rangle$
u_i''	Velocity fluctuation with respect to $\widetilde{U}_i$
U_i	Velocity component i
$\langle U_i \rangle$	Reynolds-averaged velocity
$\widetilde{U}_i$	Density-averaged velocity
$\underline{V}$	Velocity space of a random variable
V	Total volume of the combustion chamber
V_c	Clearance volume of the combustion chamber
V_h	Swept volume of the combustion chamber
x_i	Physical space coordinates
y_θ	Specific mass fraction
w_θ	Specific molecular mass
W_i^u, W_j^ϕ	Stochastic Wiener process for the velocity and scalars

Greek Symbols

Symbol	Description
α_c	Crank angle
α_p	Decay factor of particle temperature
α_w	Heat flux coefficient
β	Constant of Curl and Modified Curl model
δ_{ij}	Kronecker symbol
ϵ	Dissipation rate of turbulent kinetic energy
ε	Compression ratio
ζ	Mixture fraction
θ	Chemical species
ϑ	Turbulent velocity scale
κ	Isentropic exponent
λ_s	Ratio between connecting rod and crank shaft length
μ	Dynamic viscosity
μ_c	Concentration number
μ_m	m^{th} moment of of a probability function
μ_t	Turbulent dynamic viscosity
ν_t	Turbulent kinematic viscosity
ϱ	Gas phase density
σ	Number of random scalar variables in the state-space
σ_t	Turbulent Prandt or Schmidt number
τ_{ij}	Viscous stress tensor
ϕ	Random variable in state-space
ϕ''	Fluctuation of a scalar
$\widetilde{\phi}$	Density-averaged scalar
φ	Mass fraction of a chemical species
$\underline{\psi}$	Sample state-space variable
ω_t	Turbulent frequency
$\omega^{(n)}$	Importance weight factor
Ω	Chemical reaction velocity

Abbreviations

Symbol	Description
$ASTM$	American society for testing and materials
$ATDC$	After top dead center
$BTDC$	Before top dead center
CAI	Controlled auto-ignition
CFD	Computational fluid dynamics
CI	Compression ignition
DNS	Direct numerical simulation
EGR	Exhaust gas recirculation
GDI	Gasoline direct injection
GLM	Generalized Langavin model
$HCCI$	Homogeneous charge compression ignition engine
IC	Internal combustion
IEM	Interaction by exchange model
$JPDF$	Joint probability density function
MDF	Mass density function
MON	Motor octane number
NO_x	Nitrogen oxides
PDF	Probability density function
PM	Particle matter
$RANS$	Reynolds averaged Navier-Stokes
RON	Research octane number
SI	Spark ignition
SLM	Simplified Langavin model
TEL	Tetraethyl lead
TDC	Top dead center
TML	Tetramethyl lead
UHC	Unburned hydrocarbons

List of Tables

List of Figures

Chapter 1

Introduction

1.1 Motivation and objective

The internal combustion (IC) engine is the major power source for road transportation today. The limitation of natural oil resources, concerns about global warming, and the poor air quality in cities are the driving forces for looking for alternative transportation concepts such as electric cars and fuel cell vehicles. Still IC engines are going to play a major role within the next 10-15 years in road transportation due to the potential for the increase of efficiency and the reduction of pollutant emissions [111] . In addition, available infrastructure, reliability, production costs and customer acceptance are other factors providing IC engines a competitive edge over other alternative energy generation concepts. Therefore, research and development activities on IC-engines are of significant importance to achieve the goals of climate preservation and pollutant emission minimization.

In the context of this work, the phenomenon of auto-ignition in different IC engine types will be treated. The aim of this work is to introduce a reliable computational model capable of simulating auto-ignition processes in IC engines.

Considering the high loads over the entire speed ranges of today's engines, the optimization of the existing engines by downsizing or turbo-charging as well as developing new engine concepts such as gasoline direct injection (GDI), controlled auto-ignition (CAI), or homogeneous charge compression ignition (HCCI) engines is a challenge for engine developers [33].

In spark-ignition (SI) engines, auto-ignition, known as engine knock, is observed in the form of uncontrolled auto-ignition in the unburned gas region during flame propagation in the combustion chamber. The occurrence of auto-ignition can cause severe damage to engine components [51]. Engine knock may take place at full or high loads over the entire speed range. The understanding of the phenomenon

of engine knock is still in an early stage, although there have been considerable activities in this area. Describing and even predicting engine knock is a tedious task, requiring detailed knowledge of chemical and physical processes occurring in the combustion chamber.

One common anti-knock measure is the mixture enrichment at high loads to decrease the temperature in the cylinder. However, enriching the mixture leads to a deterioration of the thermodynamics processes with the disadvantage of increased fuel consumption and increased particle emissions [51]. Further design and parameter modifications to reduce knock probability of modern engines at high loads cause a reduction of engine efficiency and an increase of pollutant formation at part loads [46].

It is apparent from the above that, in modern engines, knocking is generally the limiting factor for increasing performance and efficiency at high loads for the entire speed range. Therefore, the computability of this phenomenon will be of great benefit to designers in order to reduce development costs meanwhile achieving better compliance with the strict environmental legislations.

An alternative engine concept which will be treated in this work as well is the homogeneous charge compression ignition (HCCI) engine. This engine type has been drawing a considerable attention of researches in the last decades. Like SI engines, HCCI engines operate on the principle of a dilute premixed charge. However, in contrast to the SI engines there is no spark ignition. The mixture reacts and auto-ignites simultaneously in the combustion chamber under the influence of the temperature and pressure during the compression stroke around top dead center (TDC) [33]. HCCI has no flame propagation, instead, the fuel-air mixture burns almost simultaneously. The combustion duration of the HCCI is very low. Therefore, highly diluted mixtures must be used. This can be achieved by using excessive air or Exhaust Gas Recirculation (EGR) [19, 20]. The mixture is usually preheated in order to reach auto-ignition conditions near the end of the combustion stroke.

HCCI engines have the potential to reach high compression ratios as high as compression ignition (CI) engines while producing low nitrogen oxides (NO_x) and particulate matter (PM) emissions. The elimination of throttling losses improves the efficiency of the engine and fuel consumption. HCCI engines are capable of operating with gasoline, diesel, and most of the alternative fuels. In some regards, HCCI engines incorporate the advantages of both, SI and CI engines.

On the other hand, there are still basic technical barriers to make HCCI engines applicable to a wide range of vehicles and viable for high volume production. The

main challenges are [128]:

- Controlling the ignition timing and burning rate over a larger range of engine speeds and loads.
- Extending the operating range to high engine loads.
- Engine damage due to higher amounts of heat release and pressure peaks.
- Minimizing hydrocarbon and carbon monoxide emissions.

Overcoming these technical challenges requires an improved understanding of the in-cylinder processes and understanding of influences of certain engine parameters, such as engine speed or air/fuel ratio and combustion control techniques such as exhaust gas recirculation (EGR), on the development of the combustion process.

Several numerical techniques, such as the direct numerical simulation (DNS) method, Reynolds averaged Navier-Stokes (RANS) method, or the transported probability density function (t-PDF) method, can be used to model auto-ignition in IC engines. Due to the high dimensionality of the of auto-ignition model, it is computationally prohibitive to apply the DNS method [35, 105, 124, 130]. On the other hand, in the RANS method, the chemical source term in the Reynolds averaged species transport equation must be modeled [10]. Several models have been proposed to achieve chemical closure. However, for flows with finite-rate chemistry and at high turbulence levels, the use of averaged temperature and concentration produce excessively large errors [124].

For the purpose of this work, the PDF method has been adopted because it is characterized by including the chemical source term in a closed form. Therefore, in the joint PDF formulation of the velocity and species, the important processes of convection and reaction can be accounted for without assumptions or approximations [100, 102]. On the other hand, other terms in the PDF conservation equation arise requiring closure, e.g. the molecular mixing term.

The dimensionality of the PDF conservation equation increases with the number of chemical species and other scalars included in the computational system. Therefore, conventional grid-based numerical techniques such as finite difference and finite volume methods are computationally prohibitive. The particle based Monte-Carlo approach adopted in this model has the advantage that computational effort increases only linearly with the number of scalars in the model, which makes this method more attractive to use when simulating reactive flows with complex chemical reaction systems as in the case of auto-ignition in internal combustion engines.

1.2 Organization of the Thesis

In chapter 2, the governing equations of the turbulent reacting flow are presented. Chapter 3 discusses the basic principles of the PDF method. In chapter 4, the hybrid CFD-PDF model is described in more details.

In Chapter 5, the theoretical background of the engine knock phenomenon in spark ignition is introduced. The developed model for engine knock will be applied to a case study which is presented and discussed in chapter 6

Chapter 7 presents the theoretical background of auto-ignition in homogeneous charge compression ignition engines.

In Chapter 8, the developed model for HCCI engines will be validated with two test cases: a four stroke HCCI diesel-fueled engine and a two stroke HCCI gasoline-fueled engine. The latter test case is followed by a parameter study to analyze the effect of different operational parameters on the combustion process.

In Chapter 9, the results of this work are concluded and suggestions for further research are proposed.

Chapter 2

Mathematical Principles of Turbulent Combustion Modeling

In this chapter, the partial differential equations describing the behavior of a turbulent reactive flow field are reviewed. These equations represent the conservation of mass, momentum, energy, and chemical species concentrations. For engineering purposes, usually the mean values of the flow properties are needed. Therefore, these equations are time averaged yielding the Reynolds-averaged conservation equations[104]. For ideal gases, the system of equations is closed by applying the state equation. Due to the averaging process, some terms in the equations can not be explicitly determined. Some approaches are proposed in order to model the unclosed terms in the averaged conservation equations.

2.1 The conservation equations

Also known as the continuity equation, the equation for mass conservation can be expressed as follows:

$$\frac{\partial \varrho}{\partial t} + \frac{\partial}{\partial x_i}\left(\varrho U_i\right) = 0 \ , \tag{2.1}$$

where ϱ is the density and U_i is the velocity and x_i the cartesian coordinate with $(i = 1, 2, 3)$. Implicit summation over repeated indices is assumed.

Neglecting the external forces like the gravitational acceleration, the conservation of momentum is represented by

$$\frac{\partial}{\partial t}\left(\varrho U_j\right) + \frac{\partial}{\partial x_j}\left(\varrho U_i U_j\right) = -\frac{\partial \tau_{ij}}{\partial x_j} - \frac{\partial P}{\partial x_i} \quad , \tag{2.2}$$

where P is the pressure and τ_{ij} the viscous stress tensor, which, for a newtonian

fluid, contains only simple shear effects and can be written as:

$$\tau_{ij} = -\mu \left(\frac{\partial U_i}{\partial x_j} + \frac{\partial U_j}{\partial x_i} \right) + \frac{2}{3} \mu \frac{\partial U_k}{\partial x_k} \delta_{ij} \ , \tag{2.3}$$

where μ is the dynamic viscosity.

For the conservation of the chemical species, denoted below by θ, with ($\theta = 1, ..., n$) and n is the total number of chemical species, the following equation is applied:

$$\frac{\partial}{\partial t}(\varrho \varphi_\theta) + \frac{\partial}{\partial x_i}(\varrho U_i \varphi_\theta) = -\frac{\partial J_i^\theta}{\partial x_i} + \varrho S_\theta \ , \tag{2.4}$$

where φ_θ is the mass fraction of the chemical species, J_i^θ and S_θ denote the molecular diffusion flux and the chemical source term respectively. The balance equation of the specific enthalpy is derived from total energy only including internal energy. Potential and kinetic energy are neglected [11, 54]. The equation reads,

$$\frac{\partial}{\partial t}(\varrho h) + \frac{\partial}{\partial x_i}(\varrho U_i h) = \tau_{ij} \frac{\partial U_i}{\partial x_j} + \frac{\partial P}{\partial t} + U_i \frac{\partial P}{\partial x_i} - \frac{\partial J_i^h}{\partial x_i} + \varrho S_h \ , \tag{2.5}$$

where h is the enthalpy, J_i^h is the heat diffusion flux and S_h is the source term of the enthalpy.

Combining the set of equations from 2.1 to 2.5 with the equation of state,2.6, leads to a complete deterministic description of the turbulent reactive flow.

$$P = \varrho R T \sum_{\theta=1}^{n} \frac{\varphi_\theta}{M_\theta} \tag{2.6}$$

where P is the pressure, R the universal gas constant, T the temperature and M_θ is the species molecular weight.

2.2 Averaging of the conservation equations

In a turbulent flow, the flow velocity $U(\underline{r}, t)$ can be expressed as a sum of a time-averaging component $\langle U(\underline{r}, t) \rangle$ and a time varying fluctuating component $u'(\underline{r}, t)$ with a zero mean value as follows,

$$U(\underline{r}, t) = \langle U(\underline{r}, t) \rangle + u'(\underline{r}, t) \quad \text{and} \quad \langle u'(\underline{r}, t) \rangle = 0 \tag{2.7}$$

which is known as the Reynolds-averaging. Another averaging approach preferred for modeling of reactive flows, due to the large density variations, is the

density-weighted Reynolds-averaging or the Favre-averaging. Using the Favre-average, a flow property, such as the flow velocity, can be split into a mean value $\widetilde{U(\underline{r},t)}$ and a fluctuation $u''(\underline{r},t)$ [70]

$$U(\underline{r},t) = \widetilde{U(\underline{r},t)} + u''(\underline{r},t) \quad \text{and} \quad \widetilde{U} = \frac{\langle \varrho U \rangle}{\langle \varrho \rangle}. \tag{2.8}$$

Applying the Favre-averaging to the equations (2.1) to (2.5), a set of equations describing the mean flow properties are obtained [65]:

$$\frac{\partial \langle \varrho \rangle}{\partial t} + \frac{\partial}{\partial x_i}\left(\langle \varrho \rangle \widetilde{U}_i\right) = 0 \tag{2.9}$$

$$\frac{\partial}{\partial t}\left(\langle \varrho \rangle \widetilde{U}_j\right) + \frac{\partial}{\partial x_i}\left(\langle \varrho \rangle \widetilde{U}_i \widetilde{U}_j\right) = -\frac{\partial}{\partial x_i}\left(\langle \varrho \rangle \widetilde{u_i'' u_j''}\right) + \frac{\partial \langle P \rangle}{\partial x_j} - \frac{\partial \langle \tau_{ij} \rangle}{\partial x_j} \tag{2.10}$$

$$\frac{\partial}{\partial t}\left(\langle \varrho \rangle \widetilde{\varphi}_\theta\right) + \frac{\partial}{\partial x_i}\left(\langle \varrho \rangle \widetilde{U}_i \widetilde{\varphi}_\theta\right) = -\frac{\partial}{\partial x_i}\left(\langle \varrho \rangle \widetilde{u_i'' \varphi_\theta''}\right) - \frac{\partial \langle J_i^\theta \rangle}{\partial x_i} + \langle \varrho \rangle \widetilde{S}_\theta \tag{2.11}$$

$$\frac{\partial}{\partial t}\left(\langle \varrho \rangle \widetilde{h}\right) + \frac{\partial}{\partial x_i}\left(\langle \varrho \rangle \widetilde{U}_i \widetilde{h}\right) = -\frac{\partial}{\partial x_i}\left(\langle \varrho \rangle \widetilde{u_i'' h_\theta''}\right) + \frac{\delta \langle P \rangle}{\delta t} + \langle U_i \frac{\delta P}{\delta x_i} \rangle - \frac{\partial \langle J_i^h \rangle}{\partial x_i} + \langle \varrho \rangle \widetilde{S_h} \tag{2.12}$$

Due to the averaging operation in equations (2.9) to (2.12), the details concerning the state of the flow contained in the instantaneous fluctuations are lost. New additional unknowns appear in the averaged equations, the Reynolds stresses, $\widetilde{u_i'' u_j''}$, the species mass fraction transport $\widetilde{u_i'' \varphi_\theta''}$, and the averaged source terms $\widetilde{S}_\theta$ and $\widetilde{S_h}$. Due to the strong nonlinearity of the conservation equations, the additional unknowns can not be expressed in terms of the first moment. Therefore, modeling of these terms is necessary in order to close the averaged conservation equations.

2.3 Closure models of the averaged conservation equations

The most common turbulent models based on the time-averaged Reynolds equations can be classified as follows,

2.3.1 Mixing length model

The mixing length model attempts to describe the stresses in terms of simple algebraic formula for the dynamic turbulent viscosity μ_t which can be expressed as a product of a turbulent velocity scale ϑ and a length scale ℓ

$$\mu_t = \nu_t \varrho, \tag{2.13}$$

which can also be defined as

$$\mu_t = C\varrho\vartheta\ell \tag{2.14}$$

where C is a dimensionless constant of proportionality. Most of the turbulent kinetic energy is contained in the large eddies. Therefore, the turbulent length scale ℓ is characteristic for these eddies, which has a strong connection with the behavior of the mean flow properties. For a simple two dimensional flow, ϑ can be expressed as,

$$\vartheta = c \cdot \ell \left| \frac{\partial U}{\partial y} \right| \tag{2.15}$$

where c is a dimensionless constant. Combining equations (2.14) and (2.15), a new length scale ℓ_m is derived and ν_t can be expressed as,

$$\nu_t = \ell_m^2 \left| \frac{\partial U}{\partial y} \right| \tag{2.16}$$

which is called the Prandtl's mixing length model. The Reynolds stresses can be expressed by

$$-\langle\varrho\rangle\widetilde{u_i''u_j''} = \varrho\ell_m^2 \left| \frac{\partial U}{\partial y} \right| \frac{\partial U}{\partial y} \tag{2.17}$$

The same approach can be used for predicting the turbulent transport of scalar flow properties as follows:

$$-\langle\varrho\rangle\widetilde{u_i''\varphi''} = \frac{\mu_t}{\sigma_t}\frac{\partial\varphi}{\partial y} \tag{2.18}$$

where σ_t is the turbulent Schmidt number for mass transport and turbulent Prandt number for heat transport. Recommended values for σ_t: 0.9 in near wall flow, and 0.7 in axi-symmetric jets [107]. The mixing length models are useful in flows where the turbulence properties develop proportional to the a mean flow length scale. This model can provide good predictions for thin shear layers. However, it is not capable for describing flows with separation and recirculation [123].

2.3.2 The k-ϵ Model

In this model, which is based on the Boussinesq's eddy-viscosity theory [53], two additional transport equations for the turbulent kinetic energy k and for the rate of dissipation of the turbulent kinetic energy ϵ are solved. However, the derived equations for k and ϵ can not be solved directly because of unknown terms. These terms, i.e. the second moments in the transport equations are modeled by gradient diffusion processes. Using k and ϵ, the velocity scale ϑ and the length scale ℓ are defined as follows:

$$\vartheta = k^{1/2} \tag{2.19}$$

$$\ell = \frac{k^{3/2}}{\epsilon} \tag{2.20}$$

To define the turbulent viscosity μ_t, a similar approach as in the mixing length model is being adopted based on the analogy between the molecular and turbulent diffusion. Applying eq. (2.14), the dynamic turbulent viscosity can be expressed as:

$$\mu_t = C_\mu \varrho \frac{k^2}{\epsilon}, \tag{2.21}$$

where C_μ is a dimensionless constant and k and ϵ are defined by:

$$k = \frac{1}{2}\widetilde{u_i'' u_i''} \tag{2.22}$$

$$\epsilon_{ij} = \nu_t \langle \widetilde{\frac{\partial u_i''}{\partial x_j} \frac{\partial u_i''}{\partial x_j}} \rangle, \tag{2.23}$$

The transport equations for k and ϵ in an unstationary and inhomogeneous flow can be modeled from the Navier-Stokes equations where different model assumptions are applied [60, 66, 67]. The modeled k equation takes the following form:

$$\frac{\partial}{\partial t}\left(\langle\varrho\rangle\, k\right) + \frac{\partial}{\partial x_i}\left(\langle\varrho\rangle\, \widetilde{u_i}'' k\right) = \frac{\partial}{\partial x_j}\left[\left(\mu + \frac{\mu_t}{Sc_k}\right)\frac{\partial k}{\partial x_j}\right] + \langle\varrho\rangle\left(P_k - \epsilon\right), \tag{2.24}$$

where Pr is the turbulent Prandt number, Sc_k is the turbulent Schmidt number of the turbulent kinetic energy, and P_k is the production rate of the turbulent kinetic energy.

$$P_k = -\langle\varrho\rangle\, \widetilde{u_i'' u_j''} \frac{\partial \widetilde{U}_i}{\partial x_j} \tag{2.25}$$

and is modeled as follows:

$$P_k = \frac{\mu_t}{\langle\varrho\rangle}\left(\frac{\partial \widetilde{U}_j}{\partial x_i} + \frac{\partial \widetilde{U}_i}{\partial x_j}\right). \tag{2.26}$$

The transport equation for ϵ reads [126]

$$\frac{\partial}{\partial t}\left(\langle\varrho\rangle\, \epsilon\right) + \frac{\partial}{\partial x_i}\left(\langle\varrho\rangle\, \widetilde{u}_i'' \epsilon\right) = \frac{\partial}{\partial x_j}\left(\left(\mu + \frac{\mu_t}{Sc_\epsilon}\right)\frac{\partial \epsilon}{\partial x_j}\right) + \langle\varrho\rangle\, \frac{\epsilon}{k}\left(C_{\epsilon 1} P_k - C_{\epsilon 2}\epsilon\right) \tag{2.27}$$

where the standard values for the model constants are shown in Table 2.1.

The $k-\epsilon$ turbulence model is the most widely used and validated turbulence model. It has achieved a notable success in calculating a wide variety of thin shear layer and recirculating flows without need to case-by-case adjustment of model constants. For a wide range of engineering applications, especially those including confined flows where the Reynolds shear stress is most important, this model shows an excellent performance. However, the $k-\epsilon$ model shows a moderate performance in other cases such as in curved boundary layers and swirling flows [14, 70].

C_μ	Sc_k	Sc_ϵ	$C_{\epsilon 1}$	$C_{\epsilon 2}$
0.09	1.0	1.3	1.44	1.92

Table 2.1: Applied constants values of the standard $k-\epsilon$ model [3]

2.4 Reaction closure models

Modeling of turbulent reactive flows requires solving the averaged conservation equation for species transport (eq. 2.4). This equation contains an averaged chemical source term S_θ which has a strong non-linear nature with respect to the temperature [59], and thus,

$$\widetilde{S}_\theta \neq S_\theta(\widetilde{\varphi}). \tag{2.28}$$

Therefore, the averaging of the chemical source term leads to misleading results about chemical reaction development especially in modeling kinetically controlled processes. The influence of turbulence on the mean rate of reaction may be treated by different types of combustion models. A first model is based on the ideas of the eddy dissipation concept, which assumes the mean turbulent reaction rate is determined by the intermixing of cold reactants with hot combustion products [74]. A second model is the eddy break up model [113] in which it is assumed that the reaction rate is given by mixing because the chemical reactions are very fast in comparison to the transport process. A third combustion model is based on the flamelet assumption, i.e. the turbulent flame should be composed by an ensemble of laminar flamelets [12, 94, 95, 114]. The length and time scales in the reaction zone are assumed to be smaller than the characteristic turbulent length and time scales, respectively. A fourth model adopts the Probability Density Function (PDF) [30] in which chemical source term exists in a closed form.

Chapter 3

Theoretical Background of the PDF Methods

As presented in chapter 2, the averaged conservation equations produce unclosed terms representing the transport of the variance of the momentum and scalars. Different models have been introduced for closing the equations system. The PDF method is one approach for modeling turbulent reactive flows [88, 98, 102]. As will be presented in this chapter, this approach has the advantage of having the rate of chemical reaction in closed form. In this context, a PDF form can be presented with a prescribed shape or to be generated by deriving a transport equation for the joint PDF of velocity and scalars.

3.1 Basic definitions

Considering the stochastic nature of turbulent reactive flows, it is more convenient to model this kind of flow using probabilistic techniques. From experimental observations of turbulent flows, when repeated measurements are taken of a certain flow property such as the temperature, the species concentrations, or the flow velocity at a certain location and time, the results obtained may be different. Although the same initial and boundary conditions as well as the deterministic equations governing the flow, described in chapter 2, remains unchanged, the flow is not determined. The reason behind the deviation of the experimental measurement is that the boundary and initial conditions are only nominally determined. In fact, slight fluctuations in the surrounding temperatures, pressure or even in the equipment setup due to manufacturing tolerances are amplified by the turbulence and may lead to significant changes in the flow characteristics [102].

The distribution function F_ϕ is the starting point for the statistical description

of a certain random variable ϕ. It describes the probability of a region of the sample space ψ in which an event can take place. F_ϕ is a non-decreasing function which varies from 0 to 1 as ψ varies from $-\infty$ to $-\infty$ and is expressed as

$$F_\phi(\psi) = Prob(\phi \leq \psi) \tag{3.1}$$

From the distribution function, the probability density function f_ϕ can be derived as follows

$$f_\phi(\psi) = \frac{\partial}{\partial \psi} F_\phi(\psi) \tag{3.2}$$

$f_\phi(\psi)$ can also be defined as the expected value of the delta function,

$$f_\phi(\psi) = \langle \delta(\phi - \psi) \rangle \tag{3.3}$$

The probability density function has three main properties:

$$f_\phi(\psi) \geq 0 \tag{3.4}$$

$$\int_{-\infty}^{\infty} f_\phi(\psi) d\psi = 1 \tag{3.5}$$

and

$$f_\phi(-\infty) = f_\phi(\infty) = 0 \tag{3.6}$$

In engineering applications, the detailed description of the flow in time and space may not be of practical interest. Instead, one would likely average the time-dependent output to obtain what is typically desired such as average fuel consumption, average power, or average pollutant formation [124]. In this context, the mean E, also known as the expectation, of a random variable ϕ is generally defined by

$$E(\phi) = \langle \phi \rangle = \int_{-\infty}^{\infty} \psi f_\phi(\psi) d\psi \tag{3.7}$$

Consequently, for a function Q of random variable ϕ, a mean value can be expressed by the relation

$$\langle Q(\phi) \rangle = \int_{-\infty}^{\infty} Q(\psi) f_\phi(\psi) d\psi. \tag{3.8}$$

The fluctuation of of the variable ϕ is defined by:

$$\phi^{'} = \phi - \langle \phi \rangle \tag{3.9}$$

and the variance is defined as the mean square fluctuation

$$var(\phi) = \langle \phi^{'2} \rangle = \int_{-\infty}^{\infty} (\psi - \langle \phi \rangle)^2 f_\phi(\psi) d\psi \tag{3.10}$$

generally, the m^{th} moment of a random function is

$$\langle \phi'^m \rangle = \int_{-\infty}^{\infty} (\psi - \langle \phi \rangle)^m f_\phi(\psi) d\psi \tag{3.11}$$

A mathematical expectation can not be measured. Therefore, it is necessary to have a relationship between measurable quantities and the mathematical expectation [102]. The ensemble average $\langle \phi \rangle_N$ is used as a representation of the mean value of N measurements of a variable ϕ and is defined by

$$\langle \phi \rangle_N = \frac{1}{N} \sum_{n=1}^{N} \phi^n \tag{3.12}$$

and for a sufficiently large N, the mathematical expectation of the ensemble average of ϕ then is

$$E(\langle \phi \rangle_N) = \langle \phi \rangle. \tag{3.13}$$

analog to equation (3.3)

$$f_{\phi N}(\psi) = \frac{1}{N} \sum_{n=1}^{N} \delta(\phi - \psi^{(n)}) \tag{3.14}$$

and the mathematical expectation of $f_{\phi N}(\psi)$ can be determined as follows [102],

$$E(f_{\phi N}(\psi)) = f_\phi(\psi) \tag{3.15}$$

The ensemble average $f_{\phi N}(\psi)$ is represented by a set of delta functions of magnitude of $\frac{1}{N}$, while $f_\phi(\psi)$ may be a continuous function. For a sufficiently large number N, the ensemble average can be used as a good approximation of the mathematical expectation because the probable error decreases with the square root of N [102].

The probability density functions of the variables ϕ_1 and ϕ_2 are defined by f_{ϕ_1} and f_{ϕ_2} respectively. These probability functions contain information about ϕ_1 and ϕ_2 only but they do not contain joint information. Therefore, assuming that ϕ_1 and ϕ_2 are two independent variables, their joint probability density function $f_{\phi_1\phi_2}$ can be defined by,

$$f_{\phi_1\phi_2} = f_{\phi_1} \cdot f_{\phi_2} \tag{3.16}$$

The joint probability density function of the variables ϕ_1 and ϕ_2 contains information about the simultaneous events of both variables in the spaces ψ_1 and ψ_2 where $(\psi_1 < \phi_1 < \psi_1 + d\psi_1)$ and $(\psi_2 < \phi_2 < \psi_2 + d\psi_2)$.

$$f_{\phi_1\phi_2} = Prob(\psi_1 < \phi_1 < \psi_1 + d\psi_1 \bigwedge \psi_2 < \phi_2 < \psi_2 + d\psi_2) \tag{3.17}$$

A marginal PDF is a special case of the joint PDF. It represents the probability of variables when all other variables are known. For example, the marginal PDF of the variable ϕ_1 can be defined by

$$f_{\phi_1}(\psi_1) = \int_{-\infty}^{\infty} f_{\phi_1\phi_2}(\psi_1, \psi_2) d\psi_2 \tag{3.18}$$

The conditional expectation plays an important rule within PDF methods. The conditional expectations describe the statistical relationship between different events. It is defined as the probability of an event to occur under the condition that another event will occur as well. As will be explained later in this chapter, in the PDF transport equation some terms appear in form of conditional expectations to describe the two point processes. For the exact description of the two point processes, such as the molecular diffusion, statistical information is needed not only about the local state, such as the velocity or the scalars, but also for the gradients of these variables. Generally, the conditional expectation of the variable ϕ_1 with respect to the variable ϕ_2 can be defined as follows,

$$\begin{aligned} &Prob(\psi_1 \leq \phi_1 < \psi_1 + d\psi_1 \mid \phi_2 = \psi_2) \\ &\quad = \frac{Prob(\psi_1 \leq \phi_1 < \psi_1 + d\psi_1 \bigcap \psi_2 \leq \phi_2 < \psi_2 + d\psi_2}{Prob(\psi_2 \leq \phi_2 < \psi_2 + d\psi_2)} \end{aligned} \tag{3.19}$$

Accordingly, the conditional PDF $f_{\phi_1|\phi_2}(\psi_1 \mid \psi_2)$ can also defined as

$$f_{\phi_1|\phi_2}(\psi_1 \mid \psi_2) d\psi_1 = \frac{f_{\phi_1\phi_2}(\psi_1, \psi_2) d\psi_1 d\psi_2}{f_{\phi_2}(\psi_2) d\psi_2} \tag{3.20}$$

For a given function $Q(\phi_1, \phi_2)$, the conditional mathematical expectation can be calculated using the conditional probability density function definition. For a given ϕ_2=ψ_2

$$\langle Q(\phi_1) \mid \phi_2 \rangle = \int_{\psi_1} Q(\psi_1) f_{\phi_1\phi_2} d\psi_1 \tag{3.21}$$

3.2 Presumed PDF methods

This approach is based on assuming the shape of the PDF based on empirical knowledge. One way to construct the joint PDF is to assume that the joint PDF of different variables is the product of the one-dimensional PDF of each.

$$P(\psi_1, \psi_3, \psi_3, ..., \psi_n) = P(\psi_1) \cdot P(\psi_1) \cdot P(\psi_1) \cdot .... \cdot P(\psi_n). \tag{3.22}$$

However, in this case the physical meaning of this assumption is questionable because of assuming independency between variables such as the temperature and the density.

The one-dimensional PDFs can be obtained from experiments. Fig. 3.1 shows an example of the PDFs of the fuel mass fractions at different locations in a turbulent mixing layer. In the outer flow, the probability for the existence of pure fuel or pure air is high. On the other hand, the probability for the existence of a mixture of fuel and air is low. In the mixing layer, the opposite effects can be observed, meaning the probability to find a maximum value of a mixture of fuel and air is high.

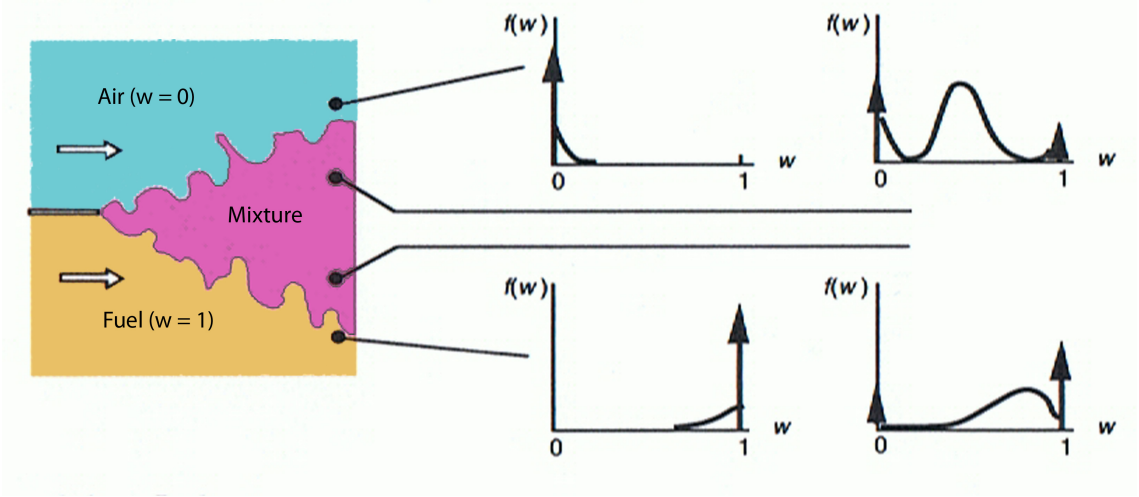

Figure 3.1: fuel-air mixture distribution in a turbulent flame [124]

For the analytical representation of the presumed PDF functions, a truncated gaussian, or β function, is usually adopted [6, 13, 93]. These form functions are determined by free parameters, which are the mean value and the variance of the calculated variables. For these two moments, two conservation equations are derived from the Navier-Stokes equations.

The usual procedure in this approach is as follows:

- Derive the conservation equations of the mean and the variance.
- Select the analytical function to determine the PDF form.
- Define the turbulence model for the description of the turbulent diffusion of the mean and the variance.
- Calculate the chemical source term and the density by integrating the PDF function.

3.3 Transported PDF method

An alternative method is based on deriving a conservation equation for the time evolution of the PDF. This approach has the advantage of having the chemical source term in closed form. There are two levels of complexity in this method. The first level is to calculate a PDF for the scalars only [57, 84]. The second level extends the analysis to cover the joint PDF of velocity and scalars. In this chapter, the joint PDF of velocity and scalar approach will be discussed in more details.

3.4 The joint PDF of velocity and scalars

As has been presented in chapter 2, a turbulent reactive flow can be fully described by the velocity and a set of scalars. The set of scalars includes the species concentrations and the enthalpy. Each component of the velocity vector can be defined as a random variable in velocity space. The same can be applied for the scalars in the scalars space. Together, they define a joint one point probability density function in the state-space of velocity and scalars. The combined space has $(3+\sigma)$ random variables, three velocity components in addition to σ number of scalars. Let $f_{U\phi}$ represents the joint PDF in the joint space of velocity and scalars $(\underline{V}, \underline{\psi})$. The probability of an event at a certain time and a certain position can be represented by the following relation:

$$f_{U\phi}(\underline{V}, \underline{\psi}) d\underline{V} d\underline{\psi} = Prob(\underline{V} \leq \underline{U} \leq \underline{V} + d\underline{V}, \underline{\psi} \leq \underline{\phi} \leq \underline{\psi} + d\underline{\psi}) \tag{3.23}$$

where $\underline{U}$ is the velocity vector in the in the velocity space $\underline{V}$ and $\underline{\phi}$ represents the vector of scalar properties in the scalar space $\underline{\psi}$

By analogy to eq. 3.18, the marginal PDFs of the velocity and scalars can be written respectively as follows

$$f_U(V) = \int_{-\infty}^{\infty} f_{U\phi}(V, \psi) d\psi \tag{3.24}$$

$$f_\phi(\psi) = \int_{-\infty}^{\infty} f_{U\phi}(V, \psi) dV \tag{3.25}$$

For the application of the JPDF transport system of an instationary (time dependent) or inhomogeneous (position dependent) flow with variable density, it is useful to define a new variable called "The mass density function" (MDF), which is defined as.

$$F_{U\phi} = \varrho(\psi) f_{U\psi}. \tag{3.26}$$

As will be introduced later in this chapter, the solution of the PDF transport system will be done using a particle method (Monte Carlo approach) [104]. In this context, a numerical particle represents a specific portion of the the overall space. The importance of the MDF can be realized from the following property relations

$$\int_{-\infty}^{\infty} F_{U\phi}(V,\psi) dV d\psi = \langle \varrho \rangle, \tag{3.27}$$

$$\int_{-\infty}^{\infty} F_{U\phi}(V,\psi) Q(V,\psi) dV d\psi = \langle \varrho \rangle \widetilde{Q}, \tag{3.28}$$

where $\widetilde{Q}$ is the Favre average of the function Q,

$$\widetilde{Q} = \frac{\langle \varrho Q \rangle}{\langle \varrho \rangle} \tag{3.29}$$

and from eq 3.30,

$$\int_{-\infty}^{\infty} F_{U\phi}(V,\psi) dV d\psi dv = M, \tag{3.30}$$

where M is the total mass in the system. In a discrete representation of the PDF, the total mass M is distributed equally over a number of particles N.

$$\Delta m = M/N, \tag{3.31}$$

where Δm is the mass of a single particle. In the computational domain, the n^{th} particle has a velocity defined by $U^{(n)}$, a composition $\phi^{(n)}$ and a position $x^{(n)}$. The state of the particle can be defined using the so called state vector represented in the $(6+\sigma)$-dimensional joined space of the velocity-composition-position $(\underline{V}, \underline{\psi}, \underline{x})$.

Analogously to the PDF, the discrete mass density function can be defined as,

$$F_N(V,\psi,x) =_{\triangle} m \sum_{n=1}^{N} \delta(V - U^{(n)}) \delta(\psi - \phi^{(n)}) \delta(x - x^{(n)}). \tag{3.32}$$

By analogy to the probability density function, the expectation of the discrete mass density function reads

$$\langle F_N(V,\psi,x) \rangle = F(V,\psi,x). \tag{3.33}$$

While the mass density function is not considered as a probability density function because the normalization condition is not fulfilled, the quantity F/M has all the properties of the PDF. In other words, $(F/M)\, d\underline{X} d\underline{V} d\underline{\psi}$ represents the probability of

a particle with a mass $\triangle\ m$, of a volume dX, and located at position described by the vector $\underline{X}$. This particle is moving with a velocity $\underline{U}$ within the interval$[\underline{V}, \underline{V} + d\underline{V}]$ and is carrying the scalar properties described by the vector $\underline{\phi}$ within the interval $[\underline{\psi}, \underline{\psi} + d\underline{\psi}]$ [72].

The computational domain is usually divided into cells. The cells should be sufficiently small to assume statistical homogeneity and contain sufficiently large number of particles.

3.5 JPDF transport equation

In chapter 2, the system of averaged conservation equations for mass, momentum, enthalpy, and species concentrations was introduced. Due to the averaging process, some terms in these equations are not in a closed form. Some models were presented as an approximation of the unclosed terms such as the $k - \epsilon$ model for turbulence modeling. A challenging problem of the averaged conservation equations is the chemical source term. Based on the the deterministic conservation equations, a transport equation for the joint one point PDF of velocity and scalars can be derived [102]. This equation reads as follows,

$$\underbrace{\varrho(\psi)\frac{\partial f}{\partial t}}_{\text{I}} + \underbrace{\varrho(\psi)V_j\frac{\partial f}{\partial x_j}}_{\text{II}} + \underbrace{\left[(\varrho(\psi)\right]g_j - \frac{\partial \langle P\rangle}{\partial x_j}\frac{\partial f}{\partial V_j}}_{\text{III}} + \underbrace{\frac{\partial}{\partial \psi_\theta}\left[\varrho(\psi)S_\theta(\psi)f\right]}_{\text{IV}} =$$
$$\underbrace{\frac{\partial}{\partial V_j}\left[\left\langle -\frac{\partial \tau_{ij}}{\partial x_i} + \frac{\partial p'}{\partial x_i}|V,\psi\right\rangle f\right]}_{\text{V}} + \underbrace{\frac{\partial}{\partial \psi_\theta}\left[\left\langle -\frac{\partial J_i}{\partial x_i}|V,\psi\right\rangle f\right]}_{\text{VI}} \tag{3.34}$$

In eq. 3.34, the term I represents the rate of change of the probability density function f. The term II represents the change of the PDF in the physical space due to convection processes. The term III describes the transport in the velocity space due to the gravity forces as well as the mean pressure gradients on the development of the PDF, while the term IV describes the transport in the composition space due to the chemical reactions. The term V describes the effects of the fluctuating turbulent pressure gradients and the viscous stresses in the velocity space. Finally, the term VI represents the effects of the molecular transport in the composition space. The Terms on the left-hand-side of the equation (I-IV), including the chemical source term, exist in a closed form. This solves the major problem of averaging the source term in the averaged Navier-Stokes Equations. On the other hand, the terms on the

right-hand-side (V,VI) exist in the form of conditional expectations. These terms are not closed because the one point PDF does not carry information about the gradient fluctuations. Therefore, terms V and VI need to be modeled. Generally, it can be said that the velocity-composition PDF equation is useful, since the main processes of convection and chemical reactions are solved exactly. Concerning the unclosed terms, different models have been developed. These models can better describe the processes in unclosed form in the PDF transport equation in comparison to the models used for closing the mean chemical reactions. In the following section, different models for the unclosed terms in V and VI will be discussed.

It is evident that the PDF transport equation is a function of many independent variables. Each variable represents a dimension either in the physical space or in the state space. Principally, it is possible to solve the PDF transport equation using the conventional discretization methods such as the finite volume method or the finite element method. However, due to the large number of variables of the computational system, it will not be feasible to use these deterministic methods to solve the transported PDF conservation equation because the computational resources required are enormous [99].

On the other hand, it is more practical to adopt a statistical approach, e.g. the Monte Carlo methods, to solve the PDF transport equation. In Monte Carlo methods, the high dimensional mass density function is represented by a large number of numerical particles. In this method, the accuracy of the system depends on the number of particles in the computational domain. By increasing the number of the particles the calculation time increases only linearly, which is a great advantage of the Monte carlo method. However, the accuracy is proportional to $\sqrt{N}$, where N is the number of particles. This means if 100 particles lead to an error of 10% , then, 10000 are needed to reduce the error to 1% [37, 102]. Thus, the Monte Carlo method converges slowly.

3.6 Monte Carlo method

As introduced above, eq. 3.34 represents the conservation equation of the one-point joint velocity-scalar PDF of turbulent reactive flows. This equation is a partial differential equation in many variables include time, space, velocity, and the thermochemical scalars. For a three dimensional problem the number of dimensions is $6 + \sigma$ (3 dimensions in the physical space, 3 dimensions in the velocity space, and σ dimensions in the scalar space).

As discussed in the previous section, applying the Monte Carlo method is more convenient for this type of problems. This approach is based on representing the computational domain via a sufficient number of Lagrangian spatially equally distributed statistical particles. The particles carry information about the position, the velocity, the density, and the thermochemical properties. The particle properties evolve according to certain particle models. The evolution of the ensemble of the particles corresponds to the evolution of the modeled PDF [99]. Each of these mathematical particles has a constant mass of Δm in the case of a rectilinear grid. For an axi-symmetrical grid, the mass of the particle depends on its distance from the centerline of the flow domain. The distribution of the particles in the domain is equivalent to the actual density distribution of the fluid particles in the physical space.

The computational domain is divided into smaller units named cells. The particles are distributed in these cells in an arrangement that satisfies certain conditions: firstly, the mass of the flow particles in the area in the physical space represented by a cell is equal to the total mass of the the particles in the same cell. Secondly, there are enough particles in the cells to ensure an accurate statistical representation of the flow characteristics in the same area. However, the particles are not bonded to the grid cells. They have there own position, velocity and scalar values and move freely between the cells of the computational domain, see fig. 3.2.

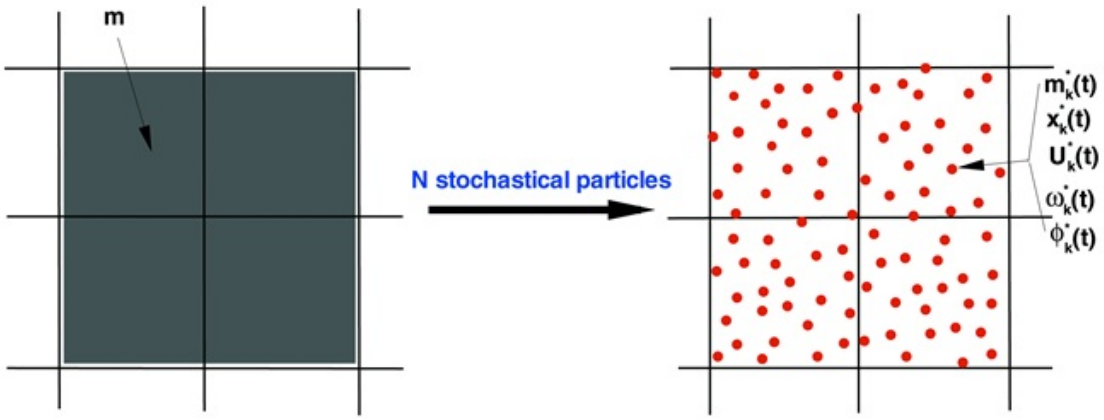

Figure 3.2: Monte Carlo particle discretization

Assuming that each particle has a position X_i a velocity U_i and scalar values of ϕ_θ, the particle properties evolve according to the following differential equations,

$$dX_i(t) = U_i(t)dt \tag{3.35}$$

$$dU_i(t) = -a_i dt + D^u dW_i^u \tag{3.36}$$

and,

$$d\phi_\theta(t) = -b_\theta d(t) + D^\phi dW_\theta^\phi \tag{3.37}$$

where a_i and b_θ are the drift factors for the velocity and the scalars respectively. D^u and D^ϕ are the diffusion factors which are assumed to be isotropic. dW_i^u and dW_θ^ϕ are stochastic Wiener increments [63, 127]. The specific expression for the drift and the diffusion terms for the velocity and the scalars will be discussed in more details later in this chapter with example models representing the evolution of particle velocity according to the Simplified Langavin model (SLM) and the evolution of the scalars using different models such as the "Interaction by Exchange with the Mean model" (IEM).

The detailed description of the coefficients contains two different kinds of mean quantities. First, the Eulerian mean quantities which can be estimated from the particle properties like the velocity denoted by $\widetilde{U}_i$ and the scalar properties represented by $\widetilde{\phi}_\theta$. Secondly, the modeled terms contain a mean turbulent frequency that determines the rate at which the modeled processes evolve. The mean turbulent frequency can not be estimated from the particle properties and has to be supplied externally.

One method to calculate the mean pressure field is to use a fully-contained PDF model incorporating an algorithm for estimating the mean pressure field [71]. In the work presented here, another approach is adopted which is based on solving the mean pressure field externally using an Eulerian finite volume method [24]. This approach is called the Hybrid CFD-PDF method which will be discussed in detailed in the next chapter.

3.7 Modeling the unclosed terms in the JPDF transport equation

As has been seen, in eq. 3.34 there are some terms (V and VI) which exist in the form of conditional expectations. In order to solve the JPDF transport equation, these unclosed terms need to be modeled.

3.7.1 Modeling of the velocity evolution

Referring to eq.3.34, the term V reads as follows,

$$\underbrace{\frac{\partial}{\partial V_j}\left[\left\langle -\frac{\partial \tau_{ij}}{\partial x_i}+\frac{\partial p'}{\partial x_i}|V,\psi\right\rangle f\right]}_{\mathrm{V}} \tag{3.38}$$

and it describes the evolution of the velocity due to viscous stresses and pressure fluctuations. The viscous effects lead to a reduction of the velocity fluctuations and the turbulent kinetic energy will be dissipated [22]. On the other hand, the pressure fluctuations lead to a reduction in the anisotropy of the turbulence [61] , as well as a relaxation of the velocity distribution to a gaussian distribution [118]. These processes can be modeled using a Langevin-process which is a stochastic model for fluid particle velocities based on Navier-Stokes equation [49] and reads

$$\frac{\partial}{\partial V_j}\left[\left\langle -\frac{\partial \tau_{ij}}{\partial x_i}+\frac{\partial p'}{\partial x_i}|V,\psi\right\rangle f\right] = -G_{ij}\frac{\partial}{\partial V_j}\left[(V_j-\widetilde{U_j})f\right]+\frac{1}{2}B\frac{\partial^2 f}{\partial V_j V_i}, \tag{3.39}$$

Using the simplified Langevin model (SLM) , the constants B and G can be derived from the turbulence theory [77].

$$B = C_0\epsilon. \tag{3.40}$$

with $C_0 = 2.1$ being an empirical constant. Under the assumption of isotropic turbulence, the model should satisfy that the turbulence kinetic energy fades away according to the relationship

$$\frac{\partial k}{\partial t} = -\epsilon. \tag{3.41}$$

To fulfill this condition, the constant G_{ij} takes the following form [102]

$$G_{ij} = -\left(\frac{1}{2}+\frac{3}{4}C_0\right)\frac{\epsilon}{k}\delta_{ij}. \tag{3.42}$$

The simplified Langevin Model (SLM) for the PDF method corresponds to the $k-\epsilon$ model of the averaged Navier-Stokes-equation. This model can be developed to calculate an anisotropic flow or to take into account complex processes such as the boundary layer effects. In this case a so called generalized Langevin model (GLM) can be applied. In the GLM approach, the constant G_{ij} is presented as a function of the reynolds stresses $\langle u_i'' u_j''\rangle_\rho$ and the gradients of the mean velocity $\tilde{U}_i/x_j$. For a detailed review of the theory and application of the Langevin model, refer to [29, 49, 86, 103, 105]

3.7.2 Modeling of scalar micro-mixing

In turbulent reactive flows, it is important to consider the effects of turbulent mixing. On the macro scale, the turbulent convection leads to the development of large gradients of the scalars. On the other hand, on the molecular level, molecular diffusion leads to the reduction of these scalar gradients. With the increase of turbulence in the flow, molecular diffusion become more influential leading to a faster reduction of the fluctuations of the scalars in the flow. In the PDF transport equation eq. 3.34 scalar mixing processes, expressed in term VI, represents the transport of scalars in the composition space due to the effects of the fluctuating pressure gradients and the molecular diffusion and exists in a unclosed form

$$\underbrace{\frac{\partial}{\partial \psi_\theta}\left[\left\langle -\frac{\partial J_i}{\partial x_i}|V,\psi\right\rangle f\right]}_{\text{VI}}. \tag{3.43}$$

3.7.3 Properties of turbulent mixing models

The model developed for turbulent micro-mixing should satisfy several conditions. e.g. [127],

- Conservation of mass and scalars:

  In turbulent mixing, mass and scalers are conserved. Therefore, it is important that the mixing model satisfy this property. Otherwise, the mass and element balance conditions will be violated.

- Decay of the scalar variance:

  The decay rate should be supplied externally, because the joint PDF of velocity and scalars does not provide information on the decay rate. The decay rate of the micro-mixing is modeled to be proportional to the decay rate of the turbulent kinetic energy. The constant of proportionality C_ϕ takes the value of 2.0 as a standard value [81].

- Boundness of the scalars:

  The mixing model should always consider the minimum and maximum values of certain scalars in order to avoid the appearance of unphysical values. For example, some of the scalars such as the mass fractions, can only take a limited value between 0 and 1. The mixing model should always satisfy this condition.

- Linearity:

  This principle applies only in the case of non-reactive flows with equal scalar diffusivity and implies that any linear combination of scalars will develop according to the same set of equations.

- Independence:

  The principle of independence requires that the statistical of one scalar is not affected by the distribution of the other scalars.

- Relaxation to a Gaussian distribution:

  Not only a decay in the variance takes place but also an evolution of the shape of the PDF to a gaussian shape. From experimental investigations [58] as well as direct numerical simulations [35] of inert mixing homogeneous isotropic turbulence, it has been seen that a binary initial distribution of the PDF evolves to a gaussian shape.

- Localness in the state space:

  Mixing of particles is governed by the location of the particles in the state space. Molecular diffusion takes place between particles that lie close to each other in the state space due to the fact that the scalar field is always a continuous function in space [117].

3.7.4 Interaction by exchange with the mean model

The main idea behind this model, known as IEM model, is based on the linear relaxation of the fluctuations of particle properties toward the mean value with an exponential relaxation [23, 28, 29]. The model can be described by the following equation

$$\Delta\phi_j^i = -\frac{1}{2}C_\phi\omega_t(\phi_j^i - \widetilde{\phi_j^i})\Delta t \tag{3.44}$$

where ω_t is the turbulent frequency which can be determined from eq. 3.45 and C_ϕ is a decay factor

$$\omega_t = k/\epsilon \tag{3.45}$$

The IEM model, schematically shown in fig 3.3, is easy to apply and has been applied for many simulations [7, 82, 83]. On the other hand, it has some disadvantages e.g. the functional form of the PDF does not evolve. Therefore, assuming

a case with initial δ-functions of two scalars, the subsequent evolution of the PDF remains two δ-function approaching each other.

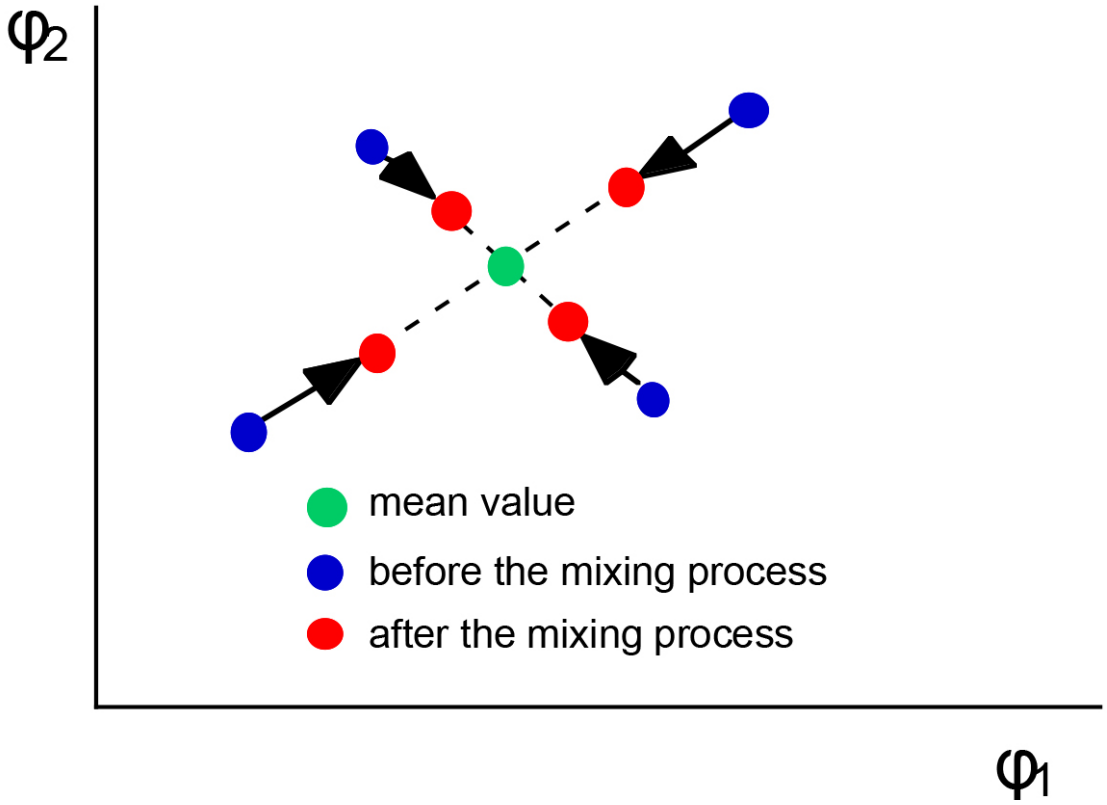

Figure 3.3: IEM model for turbulent mixing

3.7.5 Coalescence/Dispersion models

The coalescence/dispersion mixing model is based on an analogy between mixing and breakup of parcels of fluids in a turbulent single-phase flow and the coalescence and breakup of droplet in a two-phase turbulent flow. This model is often called Curl model. This model belongs to the class of pairwise-exchange models, where the effects of mixing are represented by a pairwise interaction of particles.

The standard Curl model [25], shown in fig 3.4, is defined as follows: a pair of randomly selected particles (m, n) with scalar properties $\phi_j^m t$ and $\phi_j^n t$ are chosen. The two particles exchange their scalar properties during an interval of Δt as follows

$$\phi_j^m(t + \Delta t) = \phi_j^m(t) + \frac{1}{2}(\phi_j^n(t) - \phi_j^m(t)) \tag{3.46}$$

$$\phi_j^n(t + \Delta t) = \phi_j^n(t) + \frac{1}{2}(\phi_j^m(t) - \phi_j^n(t)) \tag{3.47}$$

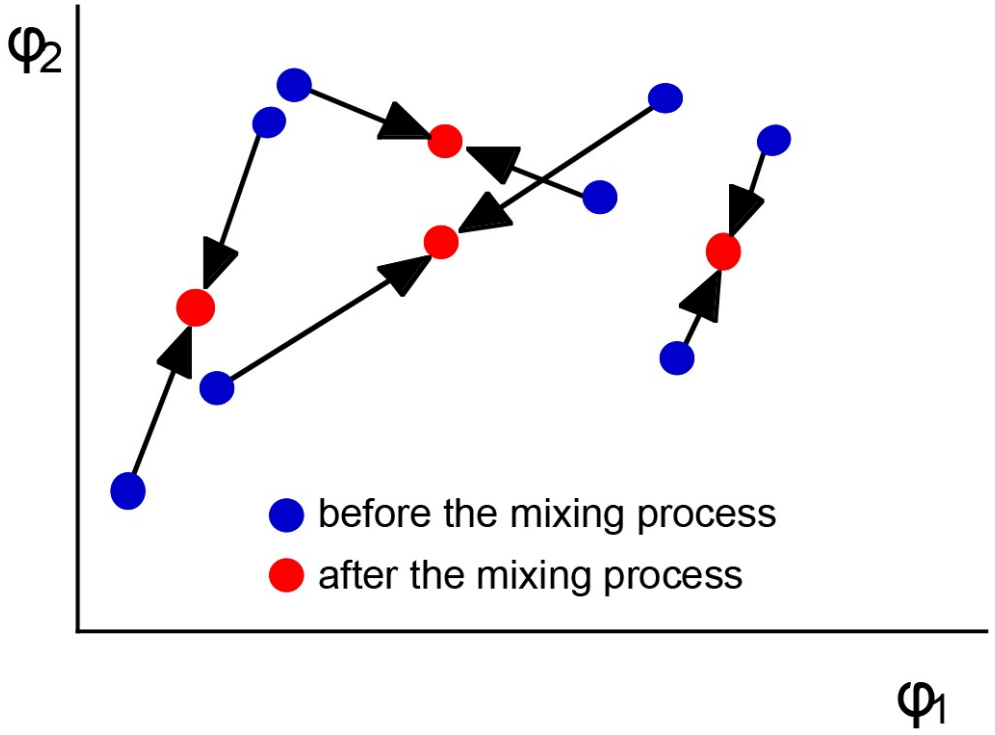

Figure 3.4: Curl model for turbulent mixing

Although Curl model leads to the relaxation of the PDF shape, the new state after mixing lies in the middle between the starting states. Therefore, only discrete points in the state space are possible [101]. A modified form was proposed by Dopazo [28], and Janika [57]. In this modification, the degree of mixing can vary between no-mixing and complete mixing. Therefore, all possible composition states are present in this case. The modified Curl model reads as follows

$$\phi_j^m(t+\Delta t) = \phi_j^m(t) + \frac{1}{2}\zeta(\phi_j^n(t) - \phi_j^m(t)) \tag{3.48}$$

$$\phi_j^n(t+\Delta t) = \phi_j^n(t) + \frac{1}{2}\zeta(\phi_j^m(t) - \phi_j^n(t)) \tag{3.49}$$

where θ controls the degree of mixing and varies randomly between 0 and 1 which corresponds to no mixing and complete mixing respectively.

For an ensemble N particles, the number of interacting pairs N_s depends on the time interval Δt and the turbulent frequency ω_t where,

$$N_s = \beta C_\phi \omega_t \Delta t N \tag{3.50}$$

The constant β is set to the value 3 in the modified curl model to guarantee the reduction of the variance [122] according to equation 3.51. Fig 3.5 shows a schematic diagram of modified curl model.

$$\frac{d\langle \phi^{'2} \rangle}{dt} = \frac{\langle \phi^{'2} \rangle}{\tau_\phi} \tag{3.51}$$

where

$$\tau_\phi = \frac{1}{C_\phi . \omega_t} \tag{3.52}$$

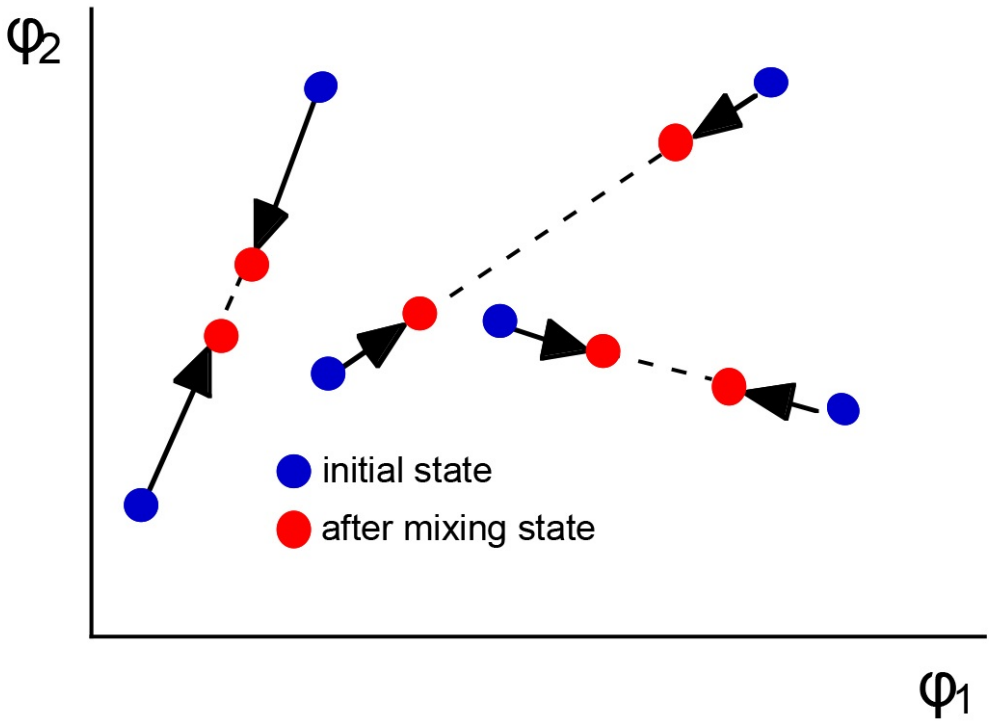

Figure 3.5: Modified curl model for turbulent mixing

Chapter 4

Hybrid transported PDF Method

In the previous chapter, the mathematical background of the transport PDF method has been discussed. The related submodels with which the turbulent reactive flow can be modeled and simulated were presented. Integrating the different submodels produces the so-called hybrid transport PDF method. In the following section in this chapter, the practical implementation of the hybrid transport PDF method will be presented.

4.1 Numerical implementation

This approach is based on the hybrid CFD-Monte Carlo method of Correa and Pope [24] in which a hybrid algorithm is implemented such that an Eulerian finite volume model is used for solving the mean particle properties such as the mean velocities, mean turbulent kinetic energy, mean turbulent dissipation, and mean pressure field. On the other hand, the Eulerian joint velocity-scalar mass density function is represented by a spatially distributed ensemble of Lagrangian particles (the Lagrangian Monte Carlo model). The mean values obtained from the Eulerian finite volume model will be supplied to the Lagrangian Monte Carlo model which will be responsible for the calculation of the evolution of the joint velocity-mass density function. The Lagrangian algorithm is coupled to a chemistry scheme that calculates the evolution of the thermo-chemical terms such as the temperature, the chemical species mass fractions (in case of reactive flows), and the density. These thermo-chemical terms will be supplied to the Eulerian algorithm to close the calculation loop, see fig 4.1.

As mentioned before, the Lagragnian domain is being divided into cells in which the values of the velocity, the turbulent kinetic energy, and the turbulent dissipation obtained from the the finite volume algorithm are transferred to the grid nodes of the

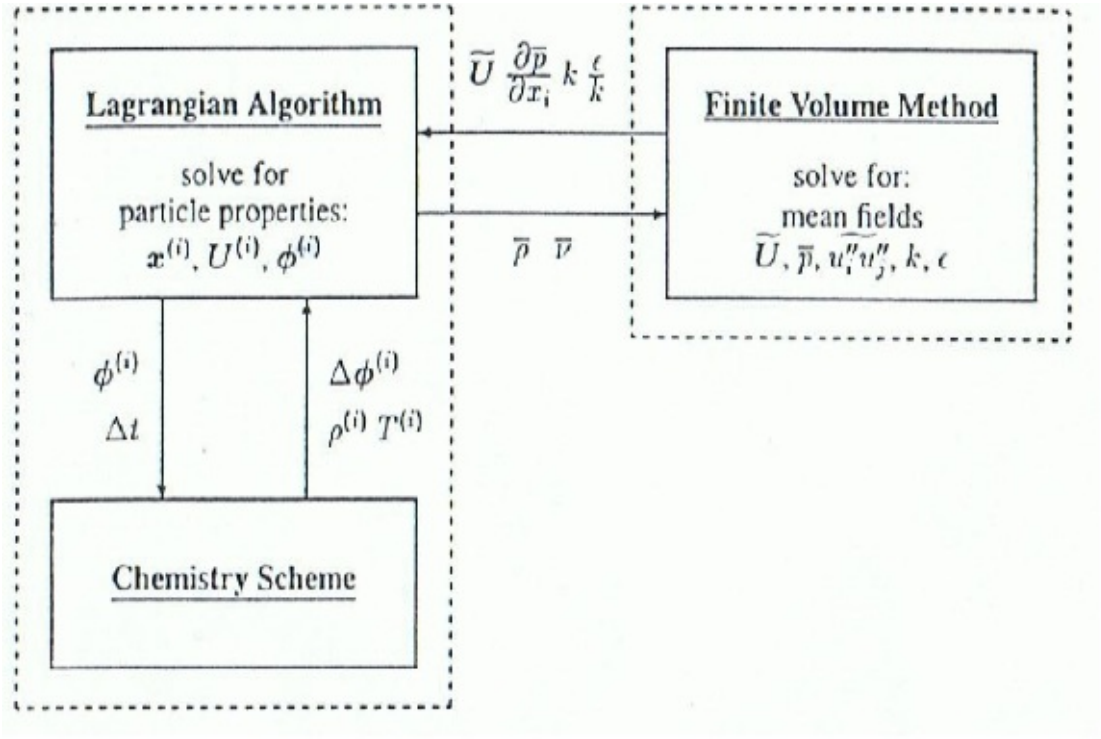

Figure 4.1: Hybrid PDF Algorithm [127]

cells. Then, these mean values are distributed on the Lagrangian particles according to their position in the cell. After the particle velocities in the Monte Carlo field are updated from the mean velocities and turbulent kinetic energy obtained from the Eulerian finite volume calculations, the velocity distribution is modified in order to maintain the correctness of the mean velocity. As a result of the hybrid method, the mean velocity and pressure field correspond to each other but they are both based on the density field of the previous Monte Carlo calculation. The density field given by the particle distribution as well as the mean flow and pressure fields, are coupled by an iterative solution that switches between the finite volume model and the Monte Carlo model. In cases where the flow field is sensitive to changes in mean density, the convergence of the hybrid method to a stable solution can be obtained only if the coupling between the new Monte Carlo density field and the finite volume model is under strong underrelaxation. The convergence in this case will be slow because more iterations between the models will be required. Another important requirement of the Monte Carlo algorithm is to ensure that the density in the Lagrangian field, which is defined as the ratio between the sum of the weights of the particles in a cell and the corresponding cell volume, can estimate the mass density function

accurately. In a rectilinear grid, where cells do not have equal volumes, the larger cells will have larger volumes than the smaller ones. If all particles in the domain are to represent the same amount of mass Δm , then the number of particles in the cells will be dependent on the local physical density represented by that cell. In other words, cells with lower density contain lower number of particles, which reduces the statistical accuracy in these cells. The same analysis can be applied for axi-symmetrical domains as well. In axi-symmetrical domains, the cells near the symmetry axis may have a smaller volume with respect to the cells far from the symmetry axis. In order to avoid the undesirable variation of the statistical accuracy in the computational domain, an importance weight factor $\omega^{(i)}$ will be introduced and multiplied to the particle mass. The new particle weight will be $\omega^{(i)}\Delta m$. These weight factors will be chosen such that the total weight to volume ratio in the domain remain correct while maintaining a statistically reasonable number of particles in the cells. This approach is explained in details by Haworth and El Tahry [50].

As mentioned before, the particle density representation, on one hand, and the mean velocity and pressure field on the other hand, are not coupled directly in the hybrid method. During the Lagrangian calculations, particles can move freely between the cells in the domain. This may lead to a change in the weight to volume ratio in the cells, while there is no physical mechanism to enforce its correctness. Therefore, another correction algorithm is introduced to correct the particle weights or positions such that a correct weight to volume ratio is ensured during the Monte Carlo calculation. In this correction algorithm, particles are moved from the cells with too high weights to the borders with the adjacent cells.

By applying the new importance weight factor to the particle mass, the particles will represent different amount of masses. Therefore, the favre average for a certain scaler ϕ can be obtained according to the following equation:

$$\tilde{\phi} = \frac{1}{W}\sum_{n=1}^{N} w^{(n)}\phi^{(n)} \tag{4.1}$$

where $W = \sum_{n=1}^{N} w^n$ represents the total weight of the particles.

4.2 Method of fractional steps

As being discussed in the previous chapter, the joint velocity-scalar mass density function is a multi-dimensional function. The development of this function relies on many parameters such as convection, pressure gradient, molecular viscosity, micro-

mixing, and chemical reactions. All these variables affect the evolution of the PDF function simultaneously.

The evolution of the PDF in the Monte Carlo method is not solved in one step but divided into several steps. The method adopted for the numerical implementation of the PDF is called the method of fractional steps. In this method, each step leads to the evolution of the PDF in one of the probability spaces of the function (physical space, velocity space, or scalar space).

The convection step and the integration of the mean pressure gradient term can not be separated in an arbitrary way because the distribution of mass and momentum in space determines the mean pressure field [127].

To preserve the first order accuracy of the solution, the convection step is divided into two smaller substeps of $\Delta t/2$. In Monte Carlo algorithm implemented in the program, the evolution of the PDF is separated into the following fractional steps [102]:

1. Convection in the physical space

$$\Delta x_i^{(n)} = U_i^n \frac{1}{2} \Delta t \tag{4.2}$$

2. Evolution in velocity space using Langevin model with Δt

3. Evolution in scalar space by micro-mixing model with Δt

4. Convection in the physical space

$$\Delta x_i^{(n)} = U_i^n \frac{1}{2} \Delta t \tag{4.3}$$

5. Convection in scalar space due to chemical reactions with Δt

Chapter 5

Auto-Ignition in Spark Ignition Engines

In chapters 2,3, and 4, the theoretical background of the turbulent reactive flow as well as the mathematical modeling based on the Monte Carlo-PDF method has been presented. This chapter will focus on the implementation of this methodology to a real life application which is the modeling of uncontrolled auto-ignition phenomenon in spark-ignition engines, known as engine knock.

In spark ignition engines, a homogeneous fuel-air mixture is supplied into the combustion chamber during the intake stroke. In the compression phase, near the end of the stroke, the ignition of the mixture is initiated using an electrical spark plug. Due to the heating up of the mixture, a pre-mixed turbulent flame develops and propagates in the combustion chamber leaving behind burned gases. The heat released due to the propagation of the flame front through the cylinder leads to an increase in the temperature and pressure behind the flame. The progressive increase of the reaction rate and the flame speed further compress and heat the unburned gases in front of the flame. This means that as the flame grows and propagates across the combustion chamber, the temperature and pressure in the endgas region rise above the value it would have in absence of combustion [2, 9, 44, 52, 62].

Due to cycle-to-cycle variation of air-fuel mixture and the distribution of fuel in the combustion chamber, the shape and the speed of the propagating flame varies accordingly [79, 92]. If the spark ignited flame is capable of moving across the combustion chamber until it fully consumes the charge, a so called normal combustion takes place. However, under high operating conditions, usually full loading, an abnormal combustion may occur in which a portion of the endgas in front of the flame suddenly auto-ignites before it has been reached by the flame. This type of abnormal combustion is called engine knock, as illustrated in fig 5.1.

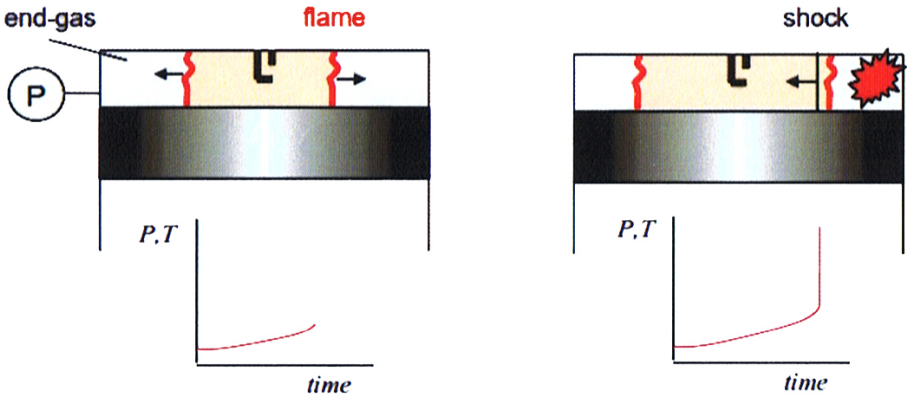

Figure 5.1: schematic diagram of engine knock [21]

A lot of attention has been given in the past to study the knocking phenomenon. The reason for the considerable interest to investigate and understand knocking is its high influence on engine performance. Knocking in spark ignition (SI) engines is one of the major challenges in achieving higher thermal efficiencies. The impact of knock on the engine may be very dangerous. The high pressure oscillations may lead to damaging engine parts or to reduce its durability. Therefore, higher Compression ratios and advancing spark timing are limited by the probability of knock occurrence [68, 119].

5.1 Fundamentals of the knock phenomenon

The term engine knock refers to the noise accompanying the uncontrolled auto-ignition in the endgas region due to the pressure waves generated [51]. Analyzing the phenomenon of knocking has led to the conclusion that there are three different modes of auto-ignition in the endgas region which may take place.These modes are known as deflagration, thermal explosion, and detonation.

In the deflagration mode, small flames are initiated locally in the endgas region and propagate with a subsonic velocity. This mode is associated with no or light knocking. While increasing temperature and pressure in the endgas, deflagration may develop to become a thermal explosion. The endgas may reach a condition were the remaining endgas auto-ignites nearly simultaneously. This mode of auto-ignition is associated with high heat release and pressure waves leading to knocking usually with a medium intensity. The third type of auto-ignition is detonation in

which shock waves are generated from the locally developed deflagration flames leading to additional heating and compression of the endgas [32, 91].

Fig 5.2 shows the influence of knocking on the pressure development in three engine cycles representing normal combustion, light knocking, and heavy knocking respectively. As can be seen, when knocking occurs, high frequency pressure oscillations are observed. In this example, as the spark timing was advanced in case c, higher knocking values are observed in comparison to case b.

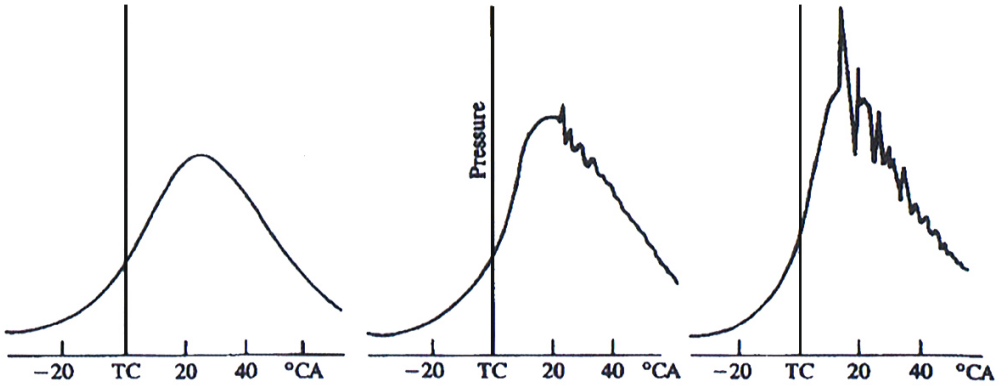

Figure 5.2: pressure curves for (a) normal combustion (b)light knocking (c)severe knocking [31]

Due to cycle-to-cycle variations, the severity of engine knock varies substantially. As can be seen in fig 5.3 , the pressure fluctuations of one hundred consecutive cycles in one cylinder of a multi-cylinder engine varies randomly between no knock to severe knocking. The maximum amplitude of the pressure fluctuations is used as an indicator for the intensity of knocking [80].

As has been mentioned above, knocking occurs in the endgas region ahead of the propagating flame in the form of an explosion. This sudden explosion releases much of the fuel's chemical energy stored in the endgas in a very short time leading to a local extensive increase of the pressure or shock waves. The shock waves generated travel in the cylinder at supersonic speed [43].

5.1.1 Physics and chemistry of knocking

Auto-ignition in the endgas of a gasoline fuel-air mixture will take place when the heat generated by the chemical reactions is higher than the heat loss to the surroundings. As a result, the temperature of the mixture will increase leading to a rapid

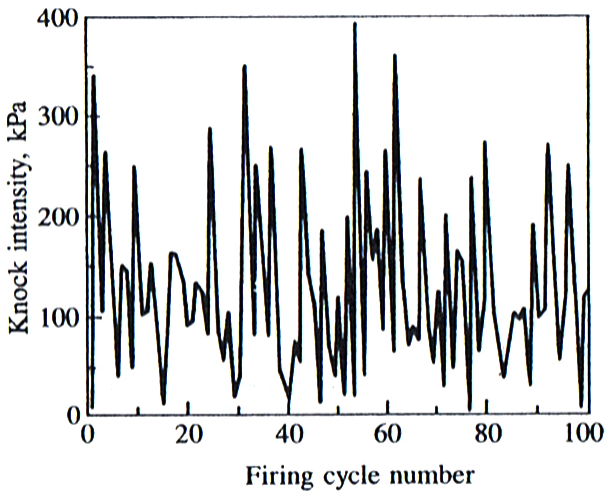

Figure 5.3: knock intensity of one hundred consecutive cycles [69]

acceleration of the chemical reaction due to their exponential temperature dependence. In complex combustion systems, the chemical reaction mechanism consists of a large number of simultaneous and interactive single reactions. However, regardless of the type of fuel, the reaction system must follow certain phases. The first phase is called the chain initiation. In the initial phase, highly reactive intermediate species, named radicals, are created from the stable fuel and oxygen molecules. The second phase is the chain propagation in which the radicals reacts with the reacting molecules producing more radicals which accelerates the chain reactions. The final step is chain termination where the radicals react with other intermediate species to produce stable molecules [124].

Autoignition in production engines usually takes place at temperatures ranging between 800 K to 900 K due to heat loss to the surroundings. At these temperatures, the high temperature oxidization mechanisms fails because the decomposition of H_2O_2 needed for chain branching is very slow at these temperatures leading to higher ignition delay time. Therefore, low temperature oxidization reaction mechanisms are more suitable to describe the chemical kinetics leading to engine knock[97]. The chemical reaction steps are as follows:

$$
\begin{array}{lcllcll}
RH & + & O_2 & \rightarrow & R\cdot & + & HO_2\cdot \quad (1)\\
R\cdot & + & O_2 & \rightleftarrows & RO_2\cdot & & \quad (2)\\
RO_2\cdot & & & \rightarrow & HOOR'\cdot & & \quad (3)\\
HO_2R'\cdot & + & O_2 & \rightleftarrows & HO_2R'O_2\cdot & & \quad (4)\\
HO_2R'O_2\cdot & + & RH & \rightarrow & HO_2R'O_2H & + & R\cdot \quad (5)\\
HO_2R'O_2H & & & \rightarrow & HO_2R'O\cdot & + & HO\cdot \quad (6)\\
HO_2R'O\cdot & & & \rightarrow & OR'O & + & HO\cdot \quad (7)\\
HO_2R'O_2\cdot & & & \rightarrow & HO_2\dot{R}''O_2H & & \quad (8)\\
HO_2\dot{R}''O_2H & & & \rightarrow & HO_2R''O & + & HO\cdot \quad (9)\\
HO_2R''O & & & \rightarrow & OR''O\cdot & + & HO\cdot \quad (10)
\end{array}
$$

with reaction (1) being the initiation step, followed by (2) and (3), the first O_2 addition and an internal H abstraction. Reactions (4) and (5) denote the second O_2 addition and an external H abstraction, respectively. After that several chain propagation and branching steps follow (6)-(10). For more details about the low oxidization chemical mechanisms, please refer to [15, 16, 17, 73]. Hereby, $R\cdot$ denotes an organic radical. This mechanism can explain the so-called two-stage ignition in which the reaction is associated with a small increase in the temperature followed by a second and complete ignition characterized by high temperature oxidization [124].

The tendency for knocking depends on the speed of the chemical reactions which in turn depends on the ability to produce H-abstraction and alkyl radical necessary for accelerating the chain reaction. The structure of the fuel molecules in terms of the bond between carbon and hydrogen atoms ($C-H$ bonds) determines the activation energy needed to brake the bond. The activation energy depends on the type of $C-H$ bond. As can be seen in eq. 5.1, the reaction speed varies exponentially in relation to the activation energy [5, 8, 39]. This means that a slight reduction in the activation energy required leads to a very high acceleration of the reaction speed.

$$\Omega \propto (\frac{-E_A}{RT}) \tag{5.1}$$

5.1.2 Knock tendency of fuels

The tendency of an engine for knocking does not depend only on the operational and design parameters. The resistance of the fuel to knock is a major factor in defining the knock characteristics of an engine. Different fuels have different tendencies to knock under the same conditions. To determine the knock sensitivity of a fuel, a

measure called the octane number is adopted. Under predefined operating conditions, the resistance to knock of a fuel is compared to a mixture of n-heptane C_7H_{16} and iso-octane $C_8H_{18}(2,2,4-trimethylpentane)$ shown in fig 5.4. By definition, the octane number of pure heptane is zero and of iso-octane is 100. A blind of these two hydrocarbons is used to define the octane number of fuels based on the ratio between both components in the mixture.

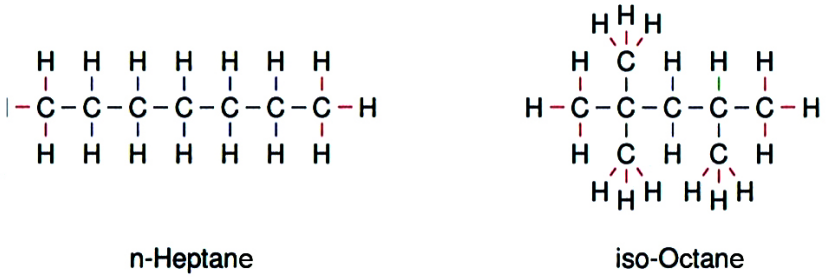

Figure 5.4: chemical structure of iso-octane and n-heptane [110]

The most famous octane number rating methods are the research method (ASTM D-2699) and the motor method (ASTM D-2700). Both methods are carried out in a standardized single-cylinder engine called the CRF engine. In table 5.1, the operating conditions for the motor and research tests are presented.

	RON	MON
Engine speed (RPM)	600	900
Inlet air temperature ($°C$)	52	149
Coolant temperature ($°C$)	100	100
Oil temperature ($°C$)	57	57
Ignition timing	13° BTDC	19°-26° BTDC
Spark plug gap (mm)	0.508	0.508
Inlet air pressure	atmospheric pressure	
Air-fuel ratio	adjusted to maximum knock	
Compression ratio	adjusted to get maximum knock	

Table 5.1: Test conditions for Octane-number measurements [51]

As can be seen in table (5.1), The operating conditions for the motor test, in terms of higher operating speed and inlet temperature as well as the earlier ignition timing are considered to be more severe than the operating conditions of the research test. Therefore, the research octane number RON is usually higher than

the motor octane number MON. The difference between the two values is called the fuel sensitivity.

The research and motor tests can not always predict how the fuel will behave under different loads and speeds as well as different environment conditions. Therefore, a road octane number was developed. The road octane number usually lies between the research and the motor octane numbers and can be related to RON and MON via the following equation.

$$RoadON = a(RON) + b(MON) + c \tag{5.2}$$

where the constants a, b, and c, are determined experimentally [51].

5.1.3 Anti-knock fuel additives

In order to improve the knock resistance of gasoline fuels, certain chemical additives are added to the fuel. These additives aim at improving the anti-knock quality of the fuel at less expense than modifying the hydrocarbon composition by refinery processes. The most effective anti-knock agent are lead alkyls. In 1923, the use of tetraethyl lead TEL ($(C_2H_5)_4Pb$) has lead to doubling the compression ratio, and thus, increasing the thermal efficiency to 40%. In 1960 tetramethyl lead TML $(CH_3)_4Pb$ was introduced which allowed a better distribution of octane in the combustion chamber and lead to a higher octane number gain in comparison to TEL, especially in highly aromatic fuels with a low sulfur content. Due to the toxic nature of lead to the environment, low-lead and unleaded gasoline fuels were introduced in the 1970s [64]. Since then, many countries have restricted or completely prohibited the use of alkyl lead in gasoline.

The use of unleaded gasoline has promoted the search for other additives that can increase the octane number of the fuel. This lead to introducing new gasoline fuels blended with oxygen containing organic compounds, known as the oxygenates. The use of the oxygenates, such as methanol CH_3OH and ethanol C_2H_5OH which are known for their higher resistance to knocking, improves the octane number of gasoline. Methanol can be produced from non-petrolic sources such as biomass or natural gas which offers a strategic advantage of being available for longer periods of time. In specially designed engines, methanol can be used as a main fuel providing high compression ratios [76].

5.1.4 Influence of operating conditions on engine knock

The onset of engine knock depends mainly on the temperature and pressure history in the endgas. Therefore, it is important to analyze the effect of different operating parameters on the development of the temperature and pressure in the endgas as being presented in fig 5.5. Increasing the compression ratio ε leads to higher peak pressure and temperature in the combustion chamber and consequently increases the tendency for knocking of an engine. Furthermore, the higher the intake temperature, the higher the endgas temperature which in tern leads to higher knocking tendency [38]. The same effect can be observed when increasing the intake pressure. Higher engine speeds is a trade-off between higher turbulence and flame speed in the combustion chamber but on the other hand less time for heat transfer to the walls.

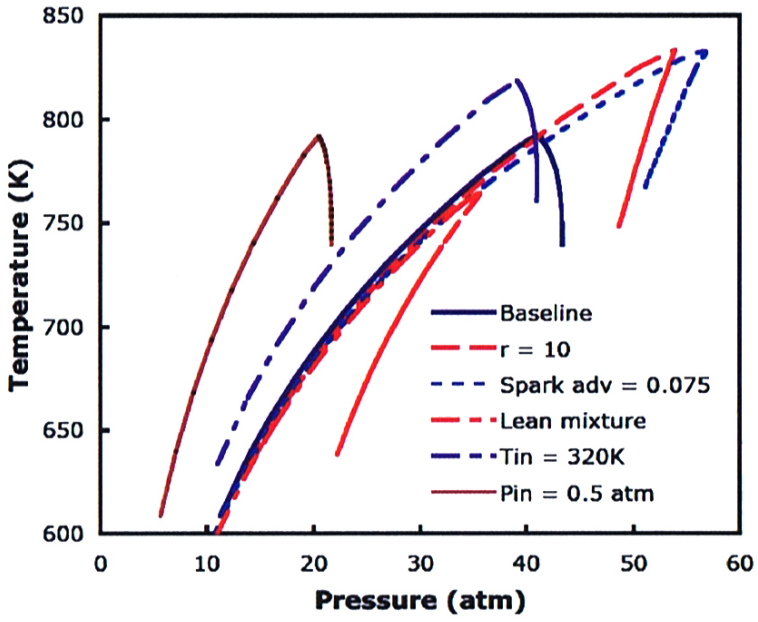

Figure 5.5: trajectories of temperature relative to the pressure during the compression phase of a gasoline engine for different initial and boundary conditions [108]

.

Chapter 6

Modeling of Engine Knock in Spark-Ignition Engines

In this work, a statistical multi-zone model based on the transported pdf method for predicting engine knock will be presented. The computational domain represents only a part of the endgas region in the combustion chamber which is located far from the propagating flame, see fig 6.1. In this multi-zone t-pdf model, the effect of turbulent mixing as well as the thermal and physical interaction between the boundary layer of the computational domain and the surroundings is considered. As will be discussed later in this chapter, the boundary layer may represent the walls of the combustion chamber or the endgas adjacent to the computational domain. In the following sections of this chapter, the different features of the developed engine knock model will be presented in details.

6.1 Monitoring points

As discussed earlier in chapter 5, the knocking phenomenon in SI engines is initiated at lower temperatures following the low-temperature oxidization chemical mechanism. Therefore, it is observed that knocking takes place far from the propagating flame and near the walls of the combustion chamber where the temperature in the endgas is relatively low compared to the region adjacent to the flame and the fuel-air mixture has enough time to reach its ignition delay time [124].

Therefore, in order to calculate engine knock it is plausible to reduce the computational domain to focus only on certain selected regions in the combustion chamber where engine knock is expected to occur. One of the features of this computational model is the ability to define sub-regions of the endgas which are selected arbitrary and are independent of each other. These sub-regions are called in the context of

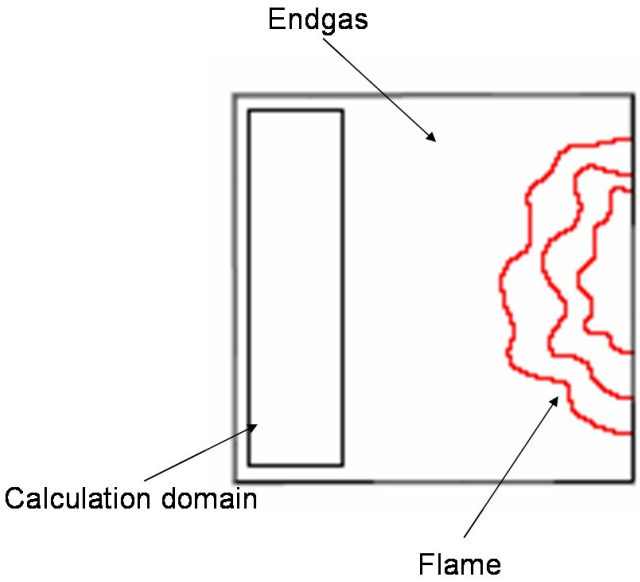

Figure 6.1: Schematic diagram representing the calculation domain

this work the monitoring points. A schematic diagram of the monitoring points is shown Fig. 6.2. In this model each of the defined sub-domains will be treated individually in terms of domain structures, initialization of particle properties, and the thermal and physical characteristics of the boundaries based on the location sub-domain which will be discussed in more details in the following section

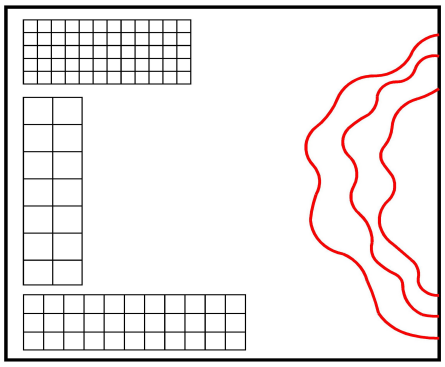

Figure 6.2: Schematic diagram of the monitoring points

6.2 Boundary conditions

Defining the boundary conditions relies on the location of the computational domain, or the monitoring points mentioned in the previous section, in the combustion cham-

ber. The location of the boundary of a monitoring point determines the temperature to be assigned to this boundary during calculations. Two types of boundaries are possible: the walls of the combustion chamber and the rest of the endgas.

If the boundary of the sub-domain is in direct contact with the walls of the combustion chamber, a constant wall temperature is assigned to the boundary during the entire calculation time. On the other hand, due to the fact that the calculation domain is far from the flame, the sides of the domain in contact with the endgas are assumed not to be influenced by the flame and no heat transfer will take place at this boundary.

In addition to the above, in the t-pdf model, the statistical particles are allowed to move in the computational domain and eventually leave it from the boundaries which are in contact with the endgas. In each calculation step, the new position of the particle is determined. If the new position of some particles lies outside the given borders of the computational domain, these particles are removed from the calculation system. On the other hand, when a particle moves towards the cylinder walls, it collides with the wall and is reflected back inside the domain with the same velocity without any loss of momentum (elastic collision).

6.3 Particle number control

It has been mentioned above, that particles which move outside the computational domain will be removed from calculation system. In order to avoid the increase in the statistical error due to the reduction in the number of particles in the cells, new particles will be created in the cells using a particle number control system.

After the convection step is calculated in each time step, the number of particles remaining in the cells are counted and compared to a user-defined minimum number of particles. If the number of particles is lower than the given minimum level of particles, new particles will be created in the cells to reach the initially defined number of particles. The position of the particles will be defined using a random generation algorithm. The particle properties and velocities will be assigned to the particles based on their position in the cells ensuring that the mean value remains conserved. Weight factors will be given to the particles in order to ensure the consistency between the physical and mathematical density in the cells.

6.4 Piston movement

The engine knock model presented here takes into account the movement of the piston during the combustion cycle. The volume of the calculation domain is modified according to the position of the piston in the combustion chamber. For the calculation of the position of the piston, the following equations is applied [96]:

$$S_\alpha = r.[(1 - \cos\alpha_c) + \frac{1}{\lambda_s}.(1 - \sqrt{1 - \lambda_s^2.\sin^2\alpha_c}) \tag{6.1}$$

where $S_\alpha$is the instantaneous displacement of the piston and λ_s is the ratio between the length of the connecting rod and the crank shaft as can be seen in fig 6.3

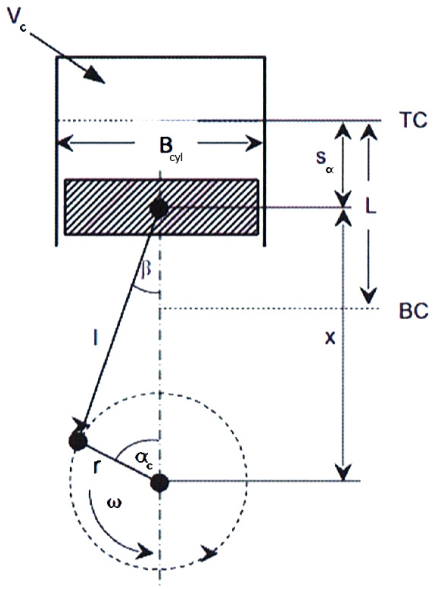

Figure 6.3: Schematic diagram of the crankshaft drive [96]

The volume of the combustion chamber can be determined by

$$V(t) = V_c + \frac{\pi}{4}B_{cyl}^2.r.[(1 - \cos\alpha_c) + \frac{1}{\lambda_s}.(1 - \sqrt{1 - \lambda_s^2.\sin^2\alpha_c}) \tag{6.2}$$

where V_c is the clearance volume which is defined as

$$V_c = \frac{V_h}{\varepsilon - 1} \tag{6.3}$$

V_c and ε represent the swept volume and the compression ratio respectively.

Due to the movement of the piston, the volume of the calculation domain changes. Accordingly, the position of the particles should be modified in order

to preserve their positions inside the calculation domain. Therefore, at the beginning of a new calculation step after the volume of the domain has been changed, the particle positions are recalculated based on the ratio between the volumes of domain in the previous and current time steps as illustrated in fig 6.4.

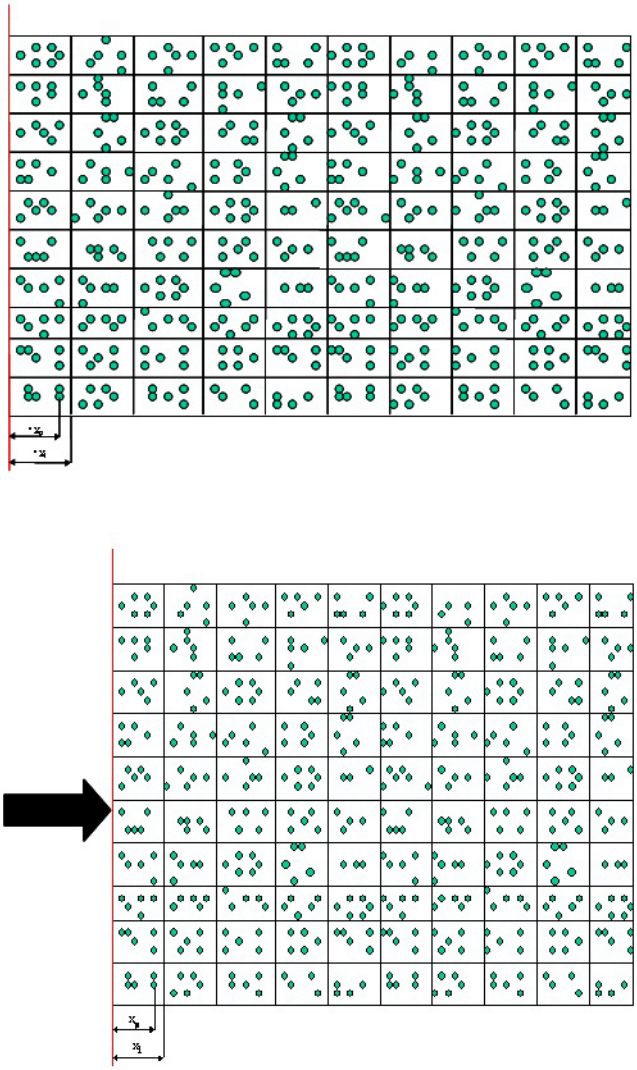

Figure 6.4: Maintaining particle position after piston movement

6.5 Heat transfer to the cylinder walls

The temperatures associated with the combustion processes in the internal combustion engine may reach very high levels, more than 2000K, with respect to the temperature of the surrounding environment. Therefore, the effect of the heat transfer

through the wall of the combustion chamber to the surroundings plays an important role in the modeling of the combustion processes in internal combustion engines.

In this work, a heat transfer model has been developed which adopts the statistical nature of the overall model. In other words, the heat transfer model will be built based on the interaction between the stochastic particles of the PDF model and the cylinder walls of the combustion chamber. The basic idea of this model is that the particles in the cells adjacent to the wall, the boundary layer cells, are considered to have thermal interaction with the cylinder wall.

The following equations describe the wall heat transfer model

$$T_{p_{t+\Delta t}} = T_{p_t} - \Delta T_{p_{t+\Delta t}} \tag{6.4}$$

where

$$\Delta T_{p_{t+\Delta t}} = \alpha_p (T_{p_t} - T_{wall}) dt \tag{6.5}$$

where $T_{p_{t+\Delta t}}$, T_{p_t},$\Delta T_{p_{t+\Delta t}}$, the updated particle temperature, the old particle temperature, and change in the particle temperature respectively. T_{wall} the cylinder wall temperature, and dt is the time step. The decay factor α_p is determined from the idle run pressure curve of the engine obtained from (Schieel et al. 2001) [109].

6.6 Test case of engine knock

In this section, the developed engine knock model will be validated. For this purpose, the experiment study with a one cylinder two stroke engine with optical accessability have been considered. Table 6.1 lists the main data of the engine

Type	ILO 372, 2-stroke SI engine
No. of cylinders	1
Bore	80 mm
Stroke	73.84 mm
Swept volume	$371.16 cm^3$
Con-rod length	148 mm
Engine speed	1000 rpm
Geo. compression ratio	ca. 20.7
Eff. compression ratio	ca. 9.0
Fuel	Octane number 95

Table 6.1: Engine data [109]

6.6.1 Setup of the simulation model

The main parameters of the setup of the calculation model are listed in table 6.2

Initial Temperature	310 ±15 K
No. of cells in X	10
No. of cells in Y	10
No. of particles/cell	50
Calc. Start	100 BTDC
Calc. end	100 ATDC
Time step size	1.0E-5

Table 6.2: Simulation data of engine knock test case

In this simulation, a 2D PDF model has been adopted. it is assumed that the computational domain represents a part of endgas which is far away from the propagating flame and is not directly influenced with it. The pressure development curve obtained from the experimental measurements has been submitted as an input parameter in each time step of the calculation. Figure 6.5 shows the pressure curve obtained from the experimental measurements of schieel et al. 2001 [109].

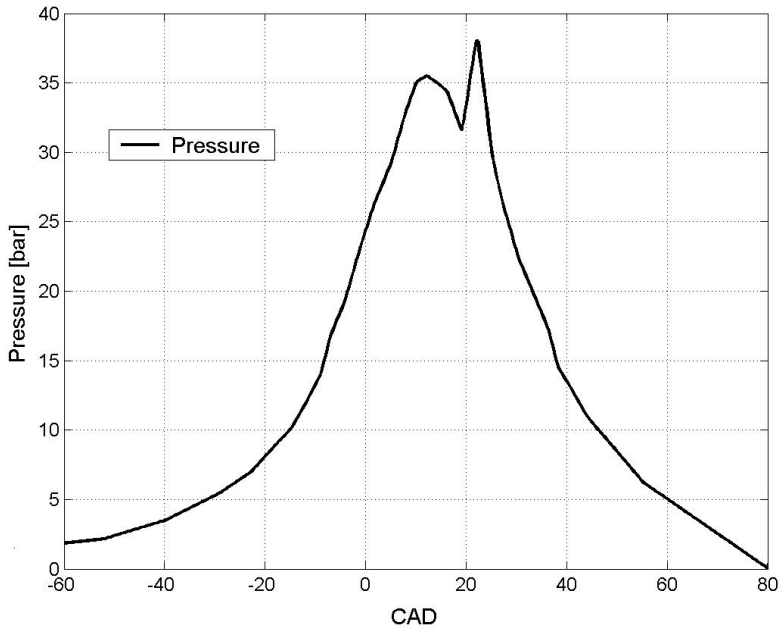

Figure 6.5: Pressure development curve recorded from experimental measurement [109].

The chemical composition is assumed to be a stoichiometric mixture of air and fuel blend with 95 % iso-octane and 5 % n-heptane. A detailed chemical reaction mechanism [40] has been coupled to the pdf model. The chemical reaction mechanism contains 121 species and 1231 chemical reactions. Numerical integration of chemical composition in time for each particle is done using the semi-implicit extrapolation method LIMEX [26, 27] which takes into account order and step size control. The calculation of heat transfer to the cylinder walls and to the surrounding environment applies the statistical model presented earlier in this chapter. The wall temperature has been assumed to be 390 K and remains constant during the entire calculation. The side of the calculation domain defined as the rest of endgas will be assigned isothermal boundary conditions.

6.6.2 Results and discussion

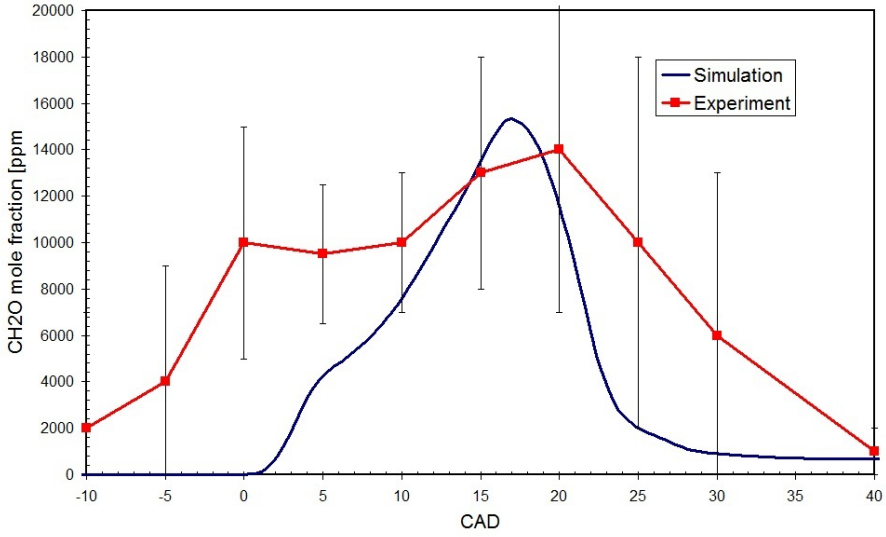

Figure 6.6: CH_2O development curve recorded from experimental measurements [109] and numerical simulations.

For the validation of the calculation, the simulation results obtained from the PDF model were compared to the experimental measurements [109]. For this purpose, the development of formaldehyde CH_2O during the combustion cycle has been used.

In fig 6.6,the mean measurement values of CH_2O from the experiment as well as the simulation results of one combustion cycle are presented. The formation of CH_2O in the simulation begins at TDC and reaches its peak value at 17 ATDC. It

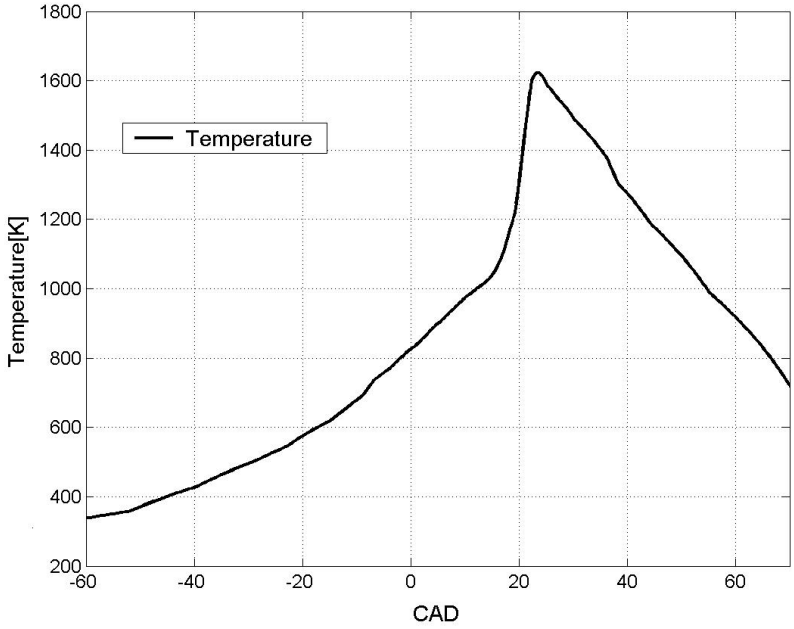

Figure 6.7: Temperature development due to auto-ignition in the endgas.

can be seen that the begin of the generation of CH_2O in the simulation is retarded compared to the experiments. However, starting from 10 ATDC, the simulation results lies within the bounds of the experimental measurements. The peak values of CH_2O in both the simulation and the experiment are very close and are reached nearly at the same position. The Simulation could predict the rest amount of CH_2O with high accuracy. It should be noted here that the experiment data are averaged from a large number of cycles. Therefore, the average measurements can not be reproduced with one simulation cycle. The reason for the differences between the experimental and calculated results could be due to not accounting for some factors such as blowby as well as the sensitivity of the combustion process for certain parameters such the initial temperature or temperature fluctuation. The effect of these parameters will be discussed in details in chapter 8.

The temperature development in the endgas is shown in fig 6.7. As can be seen, the temperature reaches its peak value at the 22 ATDC which corresponds to the time at which knocking occurs.

In fig 6.8, the development of some chemical species is illustrated. Shortly after TDC, C_8H_{18} and C_7H_{16} are decomposed into smaller compounds. Between 0 and 20 ATDC, CO is being formed. Afterwards, CO is being oxidized to produce CO_2 accompanied with high heat release reflected in the sharp temperature rise.

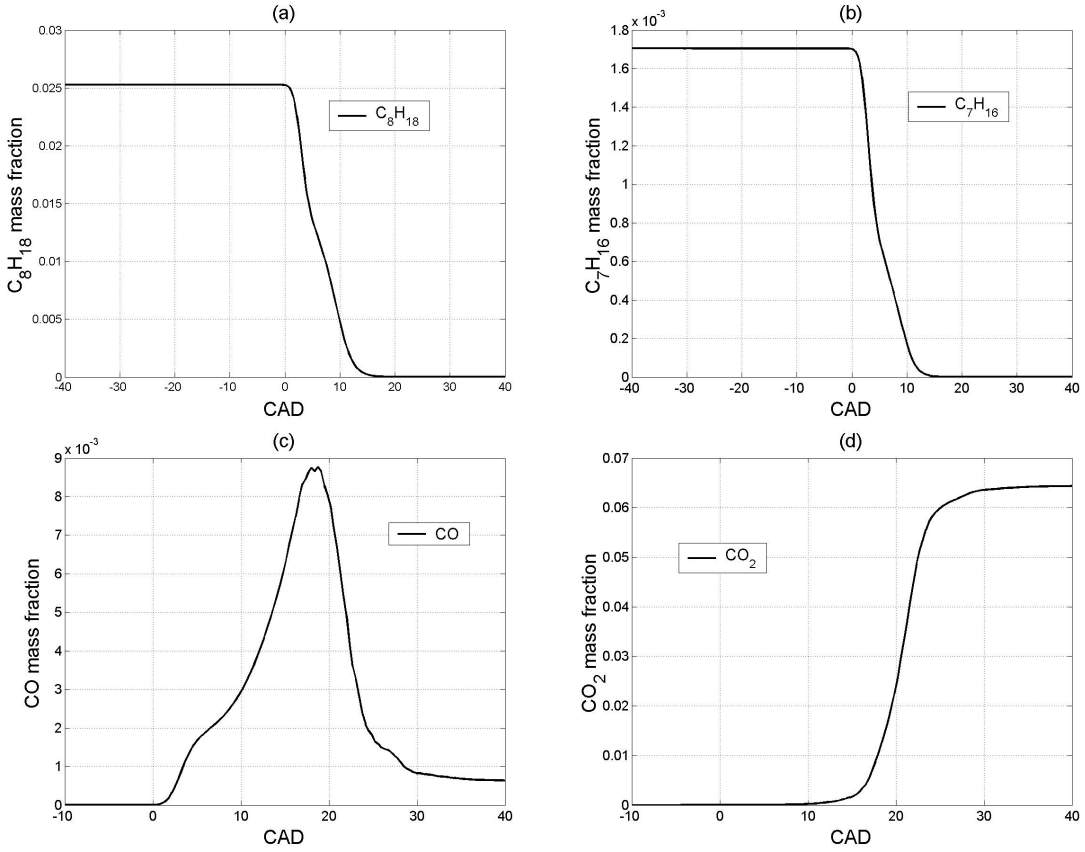

Figure 6.8: Development of the species mass fraction of: (a)C_8H_{18}, (b)C_7H_{16}, (c)CO, (d)CO_2 in the endgas.

Chapter 7

Auto-Ignition in Homogeneous Charge Compression Ignition Engines

The application of the Monte Carlo method for modeling of auto-ignition in internal combustion engines will be extended to cover the modeling of auto-ignition in homogeneous charge compression ignition (HCCI) engines.

For many years, the main types of internal combustion engines have been the spark ignition (SI) and the compression ignition (CI) engines. Spark ignition combustion takes place as a premixed flame propagates in the combustion chamber. This flame is initiated by a spark discharge. The fuel-air mixture in the SI engine is normally stoichiometric. For this reason, the soot emissions of SI engines can be neglected. The main disadvantage of the SI engine is the lower efficiency at partial loading. On the other hand, the CI combustion is characterized by the auto-ignition of the fuel in the combustion chamber due to the increase of the pressure and temperature as a result of the compression of the combustion chamber. CI combustion cycle is less efficient than the SI cycle. However, higher thermal efficiencies can be achieved in CI engines due to the higher compression ratios reached. Diesel combustion is typical for CI combustion in which air flows into the cylinder. The fuel is injected in the combustion chamber after the air is compressed. Then, the fuel droplets break down, evaporate, and mix with the air in the cylinder. Under the high temperature and pressure conditions in the combustion chamber, some spots of mixed fuel and air starts to ignite. Consequently, a further increase in the temperature and pressure of the unburned portions of the fuel-air mixture takes place leading to reducing the ignition delay time as well as reducing the evaporation time for the remaining liquid fuel. However, only a fraction of the fuel will ignite fast

because it is well mixed with air. Other portions of the fuel will not have enough time to reach a homogeneous mixture with air. Due to the lack of enough oxygen in the areas with high fuel concentrations, a high amount of soot is formed. In addition, the temperature in the combustion chamber of a diesel engine may reach 2700 K. Under this high temperature and the globally lean conditions of the diesel combustion, nitrogen oxides (NOx) are formed. Generally, the aim of the optimization of the CI combustion is to achieve a balance between the emissions of NOx and soot [128].

With the increasingly stricter emission regulations and the higher fuel prices, improvements and alternatives to these combustion concepts have been thoroughly investigated. The goal is to improve the efficiency of the SI engine and to reduce the undesired NOx and soot particulate emissions of the CI engine. The above mentioned characteristics and observations of SI and CI combustion systems subsequently lead to the conclusion that the ideal combination would be to develop an engine with the lower emission characteristics of the SI combustion while maintaining the higher thermal efficiency of the CI combustion. The HCCI engine concept has the potential to be the optimized engine solution [20, 45, 78, 121].

7.1 HCCI principle of operation

The homogeneous charge compression ignition operation can be seen as a hybrid operation between the SI and CI operations (see figure 7.1). Generally, a standard HCCI engine is characterized by premixing fuel with air before flowing into the combustion chamber similar to SI-operating engines. At the beginning of the compression stroke, the mixture is heated up. Towards the end of the combustion stroke, combustion is initiated due to auto-ignition similar to CI engines [33] . On the other hand, unlike SI engines, where ignition takes place due to a spark, in HCCI engines auto-ignition occurs as a result of temperature and pressure increase in the combustion chamber during the compression stroke as in the case in CI-operating engines.

Spectroscopic analysis done by Noguchi et al [85] on HCCI combustion showed that ignition occurs at many points simultaneously in the combustion chamber without any observation of flame propagation. They also observed high levels of CH_2O, HO_2, and O radicals before auto-ignition. These species are characteristic for low temperature auto-ignition chemistry. High concentrations of radicals of CH, H, and OH have been observed after ignition. These radicals are characteristic for high tem-

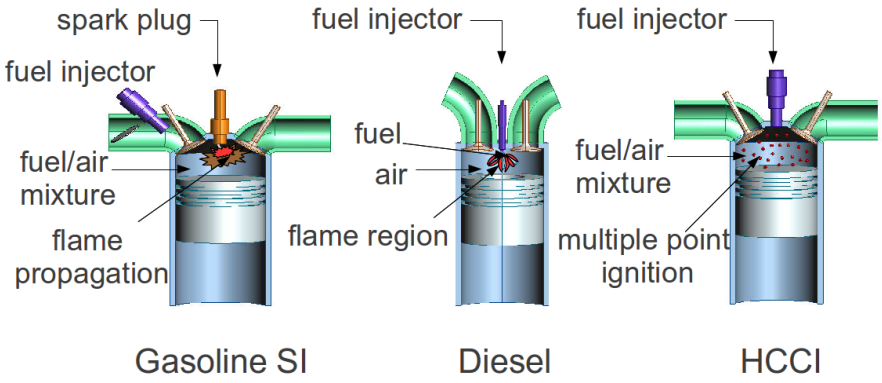

Figure 7.1: Principle of HCCI engines compared to SI and Diesel engines [89].

perature chemistry. Based on the work of Noguchi, Najt and Forster [78] attempted to reach deeper understanding of the physical processes of HCCI combustion. They concluded that HCCI auto-ignition is governed by low temperature chemistry and the main energy release is controlled by the high temperature chemistry which is dominated by CO oxidization. Unlike the SI combustion which is controlled by air mass flow and the flame propagation and the CI combustion which relies on the fuel-air mixture, the combustion process in the HCCI engine is mainly controlled by the chemical kinetics [85, 90, 125]. Therefore, modeling of HCCI combustion requires incorporating detailed chemistry models.

7.2 Advantages of the HCCI engine

In the recent years, the HCCI concept has received a lot of attention due to its numerous benefits. HCCI cycle has proven to produce the same or even higher thermal efficiency compared to the conventional diesel engines while maintaining lower emissions of nitrogen oxide (NOx) and soot particles.

The improved thermal efficiency results from the ability to operate without a throttle which leads to the elimination of pumping loses. SI engines require a stoichiometric mixture to operate. Under partial loading conditions, the spark ignition engine uses a throttle to control the amount of fuel entering the combustion chamber. This leads to a reduction in the net work [116].

In comparison to conventional SI and CI combustion, the combustion duration of HCCI engines is much shorter. Typically, HCCI combustion takes between 10-15 CAD, since no flame propagation is required inside the combustion chamber, where in SI and CI combustion, the heat release duration may take up to 60 CAD [36].

HCCI engines are capable of operating under higher compression ratios similar to CI engines. In SI engines, the compression ratio is limited due to engine knock. Therefore, in SI combustion, it must be ensured that the flame propagating from the spark plug will cover the complete combustion chamber before the onset of auto-ignition occurs in the endgas region. On the other hand, HCCI combustion is not controlled by a flame velocity but it is a set of auto-ignitions taking place at different locations simultaneously in the combustion chamber in a very short time. This means that a HCCI engine can operate under higher compression ratios which leads to an improvement in the thermal efficiency of the engine compared to SI engines.

The improved thermal efficiency is not the only benefit of the HCCI combustion. With regard to emissions, a HCCI engine has a great advantage compared to the conventional engine types. HCCI engines have lower NOx emissions than SI engines. Although three way catalysts are adequate for removing NOx from current-technology SI engine exhaust, low NOx is an important advantage relative to spark-ignition direct-injection technology.

The main challenge for CI engines is to meet the future standards of emissions especially regarding NOx and PM. Minimum flame temperature in a typical CI engine are in the range of 1900-2100 K which is high enough to produce high levels of NOx. Although the air-fuel mixture of a CI engine is globally lean. In some locations where the mixture is not totally homogeneous and at the cylinder walls soot particles are created as a product of incomplete combustion. In contrast to CI engines, HCCI engines have substantially lower emissions of particulate matter (PM) and NOx as a result of the lower combustion temperature and the dilute homogeneous air-fuel mixture [33]. The charge of a HCCI engine can reach higher levels of dilution because no flame propagation is required. The dilution of the charge is done by using a lean air-fuel mixture, by stratification, by using exhaust gas recirculation (EGR) [129], or a combination of these different techniques. The lower combustion temperature and the charge homogeneity of the HCCI engine minimizes the risk of NOx production and eliminates soot emission [34].

Other advantages of the HCCI combustion is its fuel flexibility because of the ability of using a wide variety of fuels ranging between gasoline-like to diesel-like fuels [34, 56]. HCCI engines would likely be less costly because it will be less dependent on emission control systems such as the catalytic converter in case of SI engines or the particle filter in case CI engines [1]. Generally, the HCCI engine can reach much higher part load efficiencies than SI engines with less problem with NO_x and soot

formation compared to Diesel engine [18]

7.3 Limitations of the HCCI engine

Despite the variety of benefits of HCCI engines, they have the drawback of producing high amounts of unburned hydrocarbons (UHC) and CO. In addition the HCCI engines have a small operating range and still exhibits difficulties in controlling the combustion process specially the high pressure peaks resulting from the uncontrolled auto-ignition. In general, the commercial use of the HCCI engine remains to be a real challenge [115].

In the following Chapter, a PDF based engine cycle model developed for HCCI engines will be presented. This model accounts for detailed chemical kinetics without reaction rate closure problems. Turbulent mixing, volume change due to piston movement, blowby, as well as fluid-wall interaction are being considered in the model.

In general, modeling of combustion in internal combustion engines is not an easy task due to the complexity of the combustion system in terms of geometry of the combustion chamber, determination of turbulence parameters and an accurate description of the chemical reaction. On the other hand, it is difficult to find sufficient and reliable experimental data to validate the developed models.

Chapter 8

Modeling of the HCCI Engine Combustion Cycle

As being discussed in chapter 7, the combustion process in the HCCI engine is mainly controlled by the chemical kinetics taking place in the combustion chamber. Therefore, it is crucial to incorporate a detailed chemistry model which includes tens of species and hundreds of chemical reactions. Coupling the detailed chemistry model to a direct numerical simulation model is not feasible because it is computationally highly expensive. The PDF approach is in this case very convenient because the computational effort increases only linearly with the increase of the number of variables, here the chemical species, and not exponentially like in the case of the direct numerical simulation schemes.

8.1 Modeling of a HCCI engine using the hybrid CFD-PDF method

In chapter 3 the theoretical background of the joint probability density function of velocity and scalars and its related models has been discussed. The aim of this section, is to present the implementation of this method to a practical example, in this case a HCCI engine. In general, the hybrid Monte Carlo method consists of two submodels: the Eulerian finite volume and the Lagrangian Monte Carlo PDF. The finite volume part solves the continuity equation, the impulse conservation equation, and the transport equation for the turbulent kinetic energy and turbulent dissipation. The flow field variables are transferred to the PDF submodel in which the JPDF of velocity and scalars is calculated. As a result, the new density field is generated and transferred back to the CFD submodel [131, 112]. The overall model is shown in fig 8.1. Due to the real-life application nature of the work presented

here, additional modeling techniques were adopted in the development of this model in order to meet certain requirements such as reducing the calculation time or improving the assumptions taken for defining the initial conditions of the PDF model. These modeling techniques will be discussed in details in the following sections of this chapter.

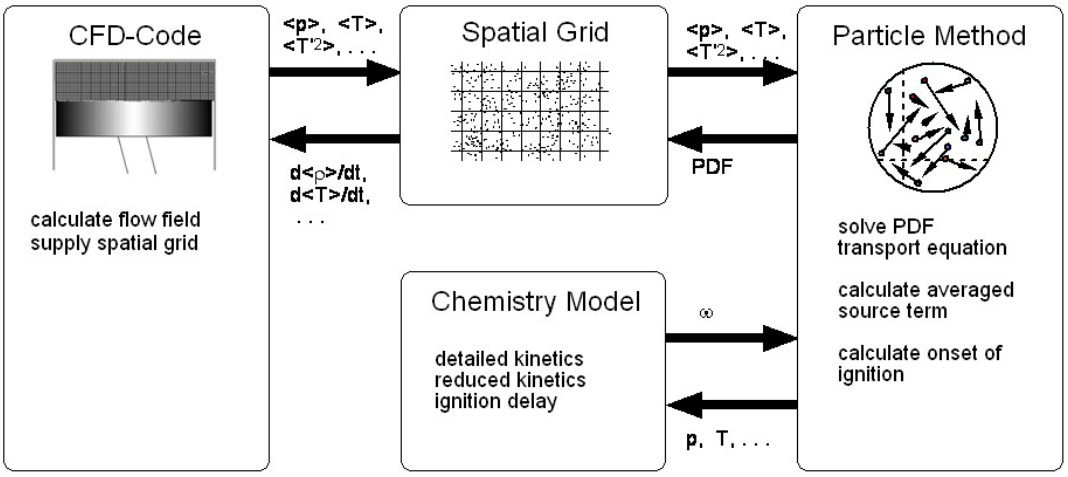

Figure 8.1: Hybrid CFD-PDF method

8.1.1 Modeling of blowby

Blowby denotes the gas leak from the combustion chamber between the compression and expansion strokes. Under the high pressure levels reached during combustion, the fuel-air mixture is forced past the rings into the crankcase. Due to blowby the generated power by the engine is reduced and consequently, the efficiency of the engine as well. Modeling of blowby has been achieved by calculating the mass of the gas mixture flowing outside the combustion chamber using the Sant Vinant Wanzel model for an outflow mass of gas stream for isentropic compressible flows [4]. This model describes the flow of gases in a throttled channel as been shown in fig 8.2.

The formulation of the Saint vinant-Wanzel model reads as follows,

$$\dot{m}_l = \mu_c . A_{geo} . P(t) . \sqrt{\frac{\overline{M}}{R.T}} \cdot \sqrt{\frac{2.\kappa}{\kappa - 1}[(\frac{P_0}{P(t)})^{\frac{2}{\kappa}} - (\frac{P_0}{P(t)})^{\frac{\kappa+1}{\kappa}}]} \tag{8.1}$$

where, κ is the isentropic exponent,

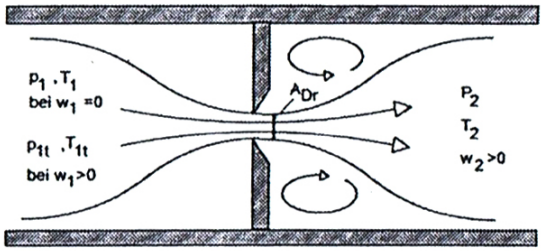

Figure 8.2: Sant Vinant-Wanzel model [4]

$$\kappa = \frac{\overline{C_p}}{\overline{C_p} - R} \tag{8.2}$$

$\dot{m}_l$ is the mass flow rate. P_0, P are the initial and instantaneous pressures and T is instantaneous temperature. $\overline{M}$ the mean molar mass, R the universal gas constant, μ_c a concentration number, and A_{geo} is the geometrical cross section of the ring clearance.

8.1.2 Initial particle distribution

For the initialization of the probability density function, a random distribution function is usually applied to assign the fluctuation values of the initial properties provided that the mean values in the cells are maintained and consistent with the mean values of the finite volume model. The model presented in this work allows to use different grid structures in the CFD and PDF parts of the program. For a sufficient accuracy of a CFD model a much finer grid is required compared to the PDF model which depends on the number of particles in the cell rather than the number of cells, see fig. 8.3.

In this model, it is possible to define a region in the CFD grid containing a group of cells which corresponds to one cell in the PDF grid. It is not necessary that the same number of cells in the CFD grid are assigned for each PDF cell. However, the cells of CFD grid coupled to the PDF grid must be indexed. This index associates the cells on the CFD side with the corresponding cells on the PDF side.

The first step in defining the initial particle properties is to define the initial mean values in the PDF cells. This will be achieved using the mean values of the different variables in the CFD domain. Therefore, assuming unstructured CFD grid and cells, the mean value of the different variables are determined at the center of each cell in the CFD calculation domain. These CFD mean values are transferred

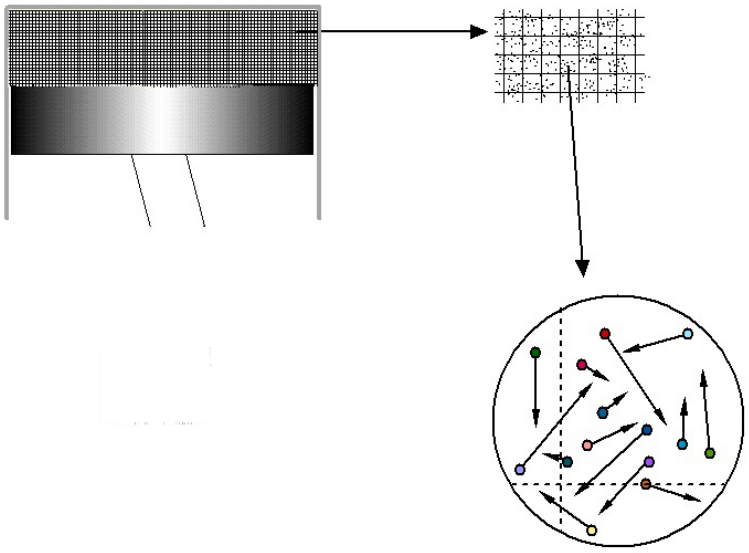

Figure 8.3: CFD vs. PDF grid

to the PDF cells. As being discussed earlier, a group of CFD cells may correspond to one PDF cell. Therefore, from the mean values of the CFD cells having the same index number mentioned above one corresponding PDF cell mean value will be calculated. The calculated mean values of the PDF cell will be defined to be located at the center of the PDF cell.

The next step in defining the initial particle properties is to define the fluctuations or the variance of the particle properties. For the definition of the variance, three methods are implemented in the model. The first and simplest method, can be used when one or only a small number of cells on the CFD side correspond to one PDF cell. In this method the variance of a certain particle property is defined based on experimental results or experience. Using the mean value transferred from the CFD model and the user-defined variance a gaussian distribution of the particle property in the PDF cell can be created as shown in fig 8.4a.

The second method to calculate the variance of a certain particle property can be used when a "sufficient number" of CFD cells corresponding to one PDF cell are provided. In the program, a parameter, which can be set manually by the user, is used to define the "sufficient number" of CFD cells. In this approach, the mean cell values obtained from the CFD grid are not only used to calculate a corresponding PDF cell mean value but also the maximum as well as the minimum values are used to define the variance. In this case, a gaussian distribution will be created. The maximum and minimum values of the means of the CFD cells are used to define the

bounds of the gaussian distribution. In fact, this approach produces two gaussian distributions with the same mean value but with two different variances as shown in fig8.4b.

The third approach is used if the number of CFD cells corresponding to a single PDF cell is large enough , 30 CFD cells for example, to produce a statistical distribution. In this case, the minimum and maximum values will be determined, as has been discussed in the second approach described above, as well as the range of the distribution (maximum value - minimum value) will be calculated. The range of the distribution is equally divided into smaller divisions. The number of divisions can be set by the user. For each division, a division range will be calculated as well. Each division range represents a portion of the overall range of the mean values of the CFD cells. The mean values of the CFD cells are compared with the division ranges and distributed into the different divisions. In this distribution, each division will contain a number of occurrences based on the number of cell mean values laying in the range of this division. Within a division, a gaussian distribution will be created for the contained occurrences. This statistical form will be used for the initial distribution in the PDF cell. The next step is to map the statistical distribution of the CFD mean values on the particles in the PDF cell. The total number of occurrences in the divisions is not necessarily equal to the number of the particles in the PDF cell. Therefore, the distribution are scaled to the number of particles. After building this statistical distribution of the mean values of the CFD cells on the particles in the PDF cell, the particles are distributed in the PDF cell using a random generator. This approach is schematically illustrated in fig8.4c.

8.1.3 Interpolation scheme

As being mentioned earlier in this chapter, at the beginning of each time step, the mean values of the variables are transferred from the CFD grid to the PDF grid are located at the center of the cells. In order to obtained the corresponding values on the grid nodes, the values at the centers are linearly interpolated from the centers of cells sharing this grid points.

In this context, it is very important to mention that interpolating from the center point to the corner points of the grid cells alone is not enough to map the correct values to the particles and vise versa. The reason is that the interpolation step evens up the values between the different cells. Therefore, a modification on the standard interpolation algorithm in the program PDF2DS used as a basis for the

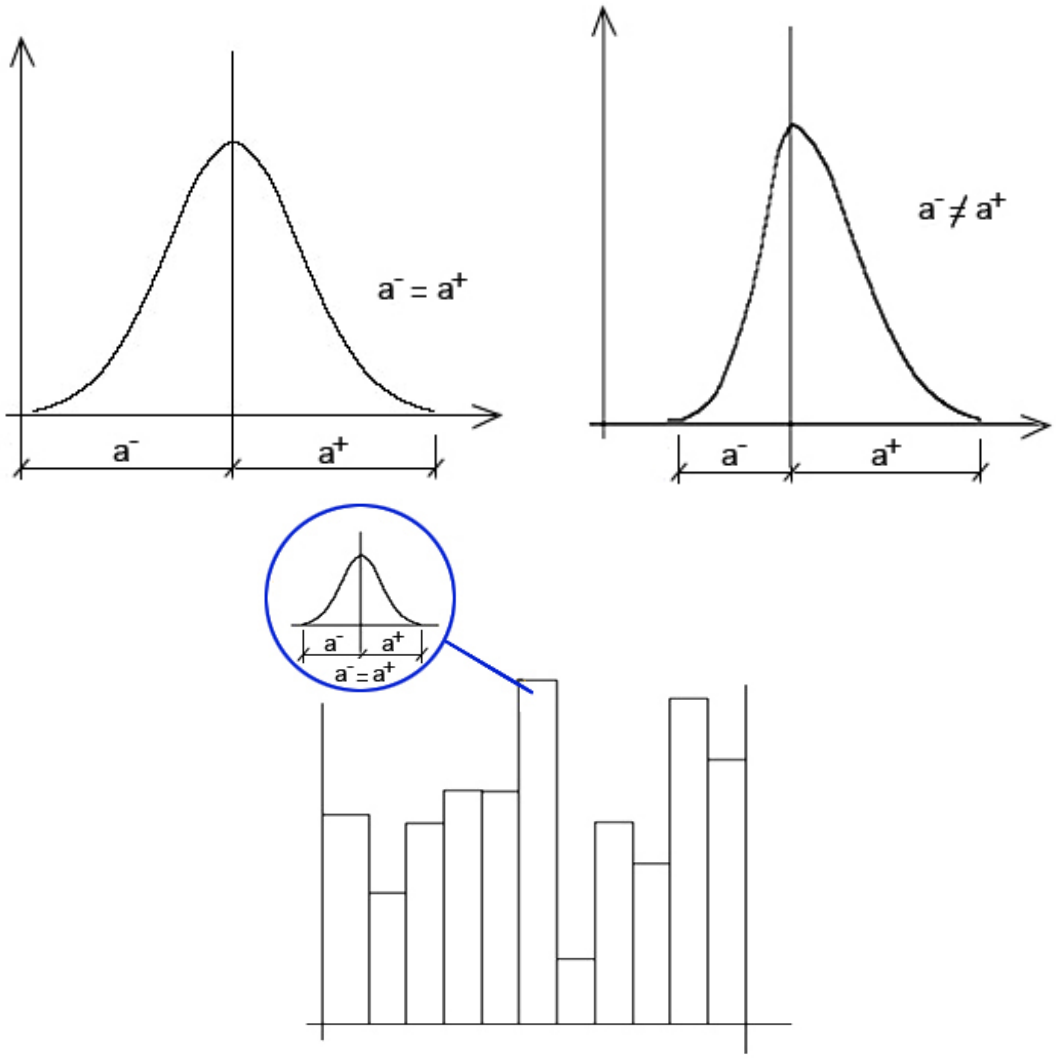

Figure 8.4: Particle initialization approaches

transported PDF calculation has been made in order to avoid this problem. In the interpolation step, not only the values on the corner nodes of the cells are determined by the interpolation but also at the midpoint of the cell as well as at the midpoints between the grid nodes on the edges of the cells. In the interpolation, the cells are divided into four quarters. The position of a particle as in which quarter it is located is determined. The interpolation is executed using the corner nodes of the quarter containing the particle.

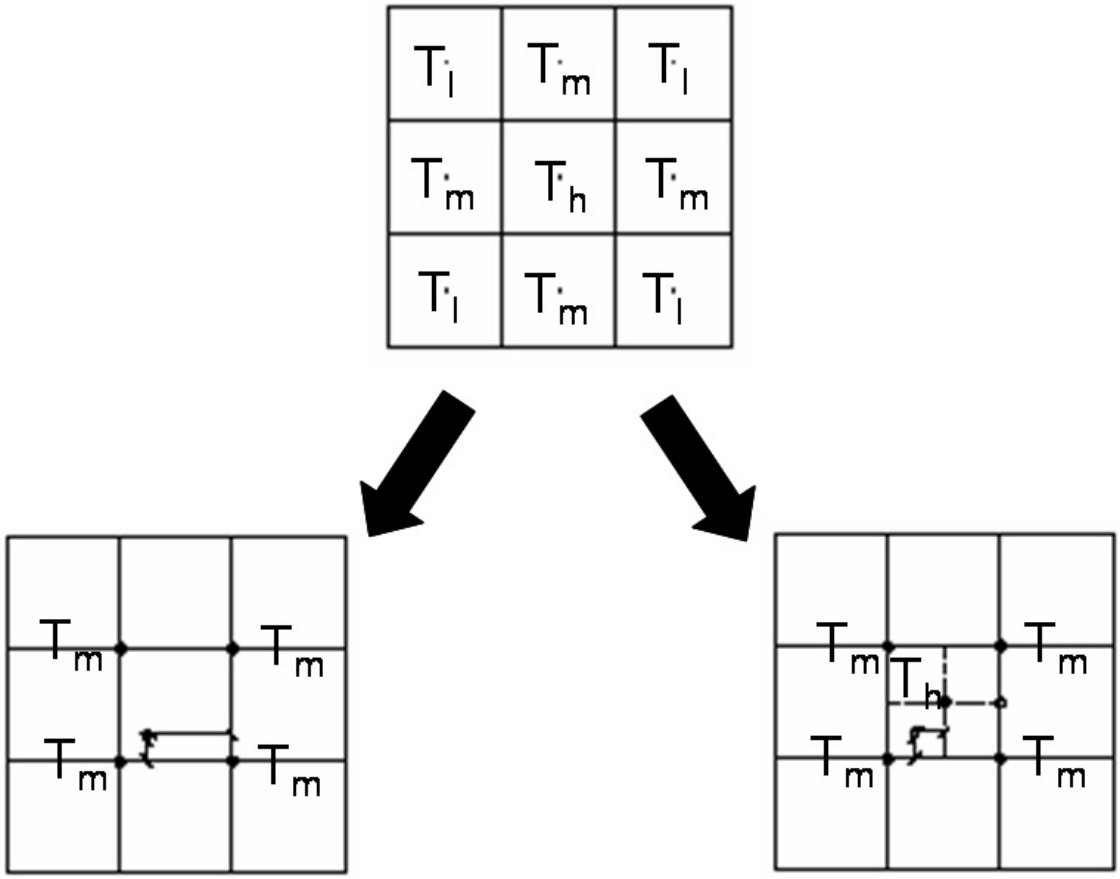

Figure 8.5: CFD PDF interpolation

The example shown in fig 8.5 demonstrates the difference between the original and the improved interpolation approaches. The upper grid shown in fig 8.5 represents a CFD grid with temperature values varying from a maximum temperature T_h and a minimum temperature of T_l. T_m is a temperature laying between T_h and T_l and assumed in this case to equal $(T_h + T_l)/2$. The grid temperatures are assumed to be located at the center of the cells.

Interpolating the temperature values to the cell nodes of the PDF grid shown in

the grid on lower left side of figure 8.5 representing the standard PFD2DS program, will lead to the maximum temperature of the particles located in the middle cell will not exceed T_m. To avoid this problem, the PDF cells are divided into four section in which the cell center temperature of the cell T_h, the temperature on the grid node T_m, and the temperature at the middle of edges of the cell are being included in the interpolation algorithm as shown in the lower right grid of figure 8.5.

8.2 Modeling of a diesel HCCI engine test case

The first test case for the validation of the developed simulation model will be presented in this section. The engine used for this application is a one cylinder research HCCI engine operating with a diesel fuel. The geometrical and operational data of the engine as well as the simulation setup and results will be discussed in details.

8.2.1 Engine data

The experiments were conducted using a one cylinder research engine which is modified variation of the OM611 diesel engine of Daimler AG. The engine design has been modified to allow homogeneous combustion process. In the following table 8.1, a list of the main data of the engine are introduced.

Type	Mercedes-Benz OM611
No. of cylinders	1
Bore diameter	88 mm
Stroke	88.4 mm
Swept volume	$537cm^3$
Con-rod length	149 mm
Engine speed	2000 rpm
Eff. compression ratio	16.0
Swirl	2.7

Table 8.1: Diesel HCCI engine data

For more details about the experimental setup and engine design and operational parameters, please refer to (Haas et al. 2007)[47].

8.2.2 Simulation setup

For this example, a closed computational domain has been defined to represent the combustion chamber. The model will calculate the development of the combustion process during the compression and expansion strokes starting after closing the intake valve (-120 BTDC) and ending before opening the exhaust valve. Therefore, it is assumed that the mass inside the combustion chamber remains constant during the calculation, i.e. blowby effects are neglected. Constant wall temperatures are assumed and set to 390 K. For the calculation of the chemical kinetics a detailed reaction mechanism of n-heptane with 81 chemical species and 300 chemical reactions [41] to represent diesel combustion has been used. In table 8.2, the setup data of the computational model are shown.

Initial temperature	409.5 ±20 K
Initial pressure	1.61 bar
No. of cells in X	10
No. of cells in Y	10
No. of particles/cell	50
Calc. start	120 BTDC
Calc. end	80 ATDC
Time step size	1.0E-5

Table 8.2: Simulation data

For the calculation of the global heat transfer to the surroundings the empirical Hohenberg model for the calculation of the heat transfer coefficient α presented in equation (5.1) has been used [55].

$$\alpha(t) = C_3.V_h^{-0.06}.T^{-0.4}.P^{0.8}.(C_m + C_4)^{0.8} \tag{8.3}$$

where C_3 and C_4 are constants and equal 130 and 1.4 respectively. P and T the instantaneous pressure and temperature, C_m average piston speed, and V_h swept volume

The heat flux through the engine walls can be calculated from the Newton formula [48] for heat transfer

$$\dot{q} = \alpha_w \cdot (T - T_{wall}) \tag{8.4}$$

where T_{wall} and α_w are the average wall temperature, and the heat flux coefficient with the walls of the combustion chamber.

8.2.3 Results and discussion

As can be seen in fig 8.6, the pressure curves obtained from the simulation have been compared to the the experimental measurements of the pressure development during a fired cycle [47, 112]. During the compression stroke, the pressure values in the simulation is slightly underestimated. However, the peak pressure could be accurately predicted by the simulation. In the expansion stroke, the pressure results of the simulation nearly coincides with the experimental measurements.

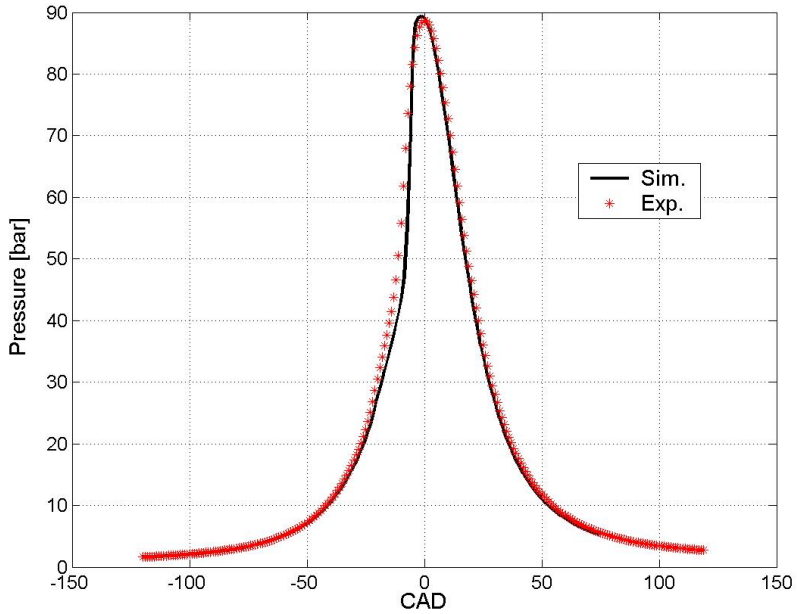

Figure 8.6: Comparison between experimental and simulation pressure curves of a Diesel-HCCI combustion cycle

Figure 8.7 shows the simulation results of the development of the temperature in the combustion chamber. In this figure, the calculated minimum, average and maximum temperature traces in the computational domain are are also shown. At the beginning of the calculation, an initial temperature fluctuation of $\pm 20K$ of the mean temperature in the combustion chamber has been given to the PDF particles. From the analysis of the temperature distribution, the difference between the maximum and average peak temperatures in the domain is around 70 K while between the minimum and average temperature more than 200 K.

The development and fluctuation of different chemical species during the combustion cycle can be seen in fig. 8.8. The decomposition of C_7H_{16} begins at 28 BTDC

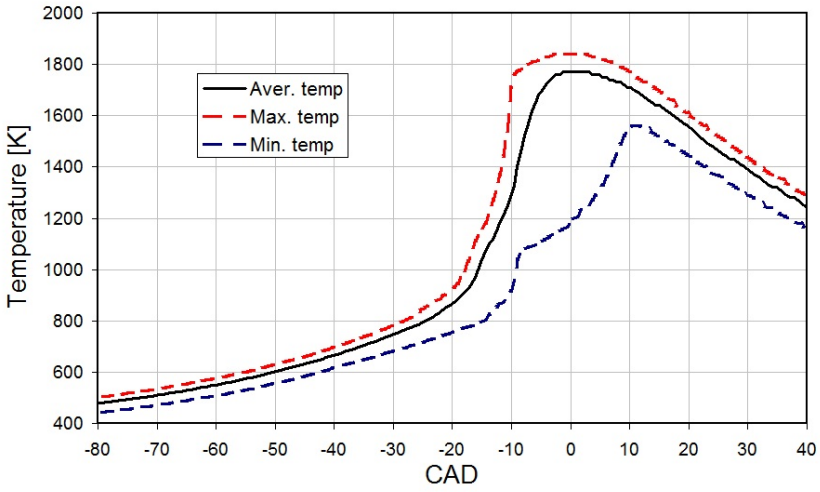

Figure 8.7: Temperature development in the simulation

slightly earlier than C_7H_{16} which takes longer time to be totally decomposed. O_2 is begins to be exhausted with C_7H_{16} and reaches the steady state at nearly the same time of CO at 13 ATDC. It can also be observed that CO is totally consumed and all particles reach the same value of CO_2 at the end of the combustion process which indicates a complete combustion of the fuel has been reached. In addition, the variation of NO developed in the combustion chamber reflects the temperature fluctuation as well. The minimum peak temperature reached is less than 1600 K which is under the value needed to create NO. On the other hand, the maximum temperature higher than 1800 K is enough for the starting the reaction mechanism of NO formation.

8.3 Modeling of a gasoline HCCI engine test case

This section is divided into two parts. The first part will deal with the validation of the developed model. For this purpose, a test case was set up and compared with experimental results of a gasoline-like fueled HCCI engine. The second part of this section will discuss the effect of several operating parameters on the characteristics of the combustion process and the influence of variation of these parameters on pollutant formation.

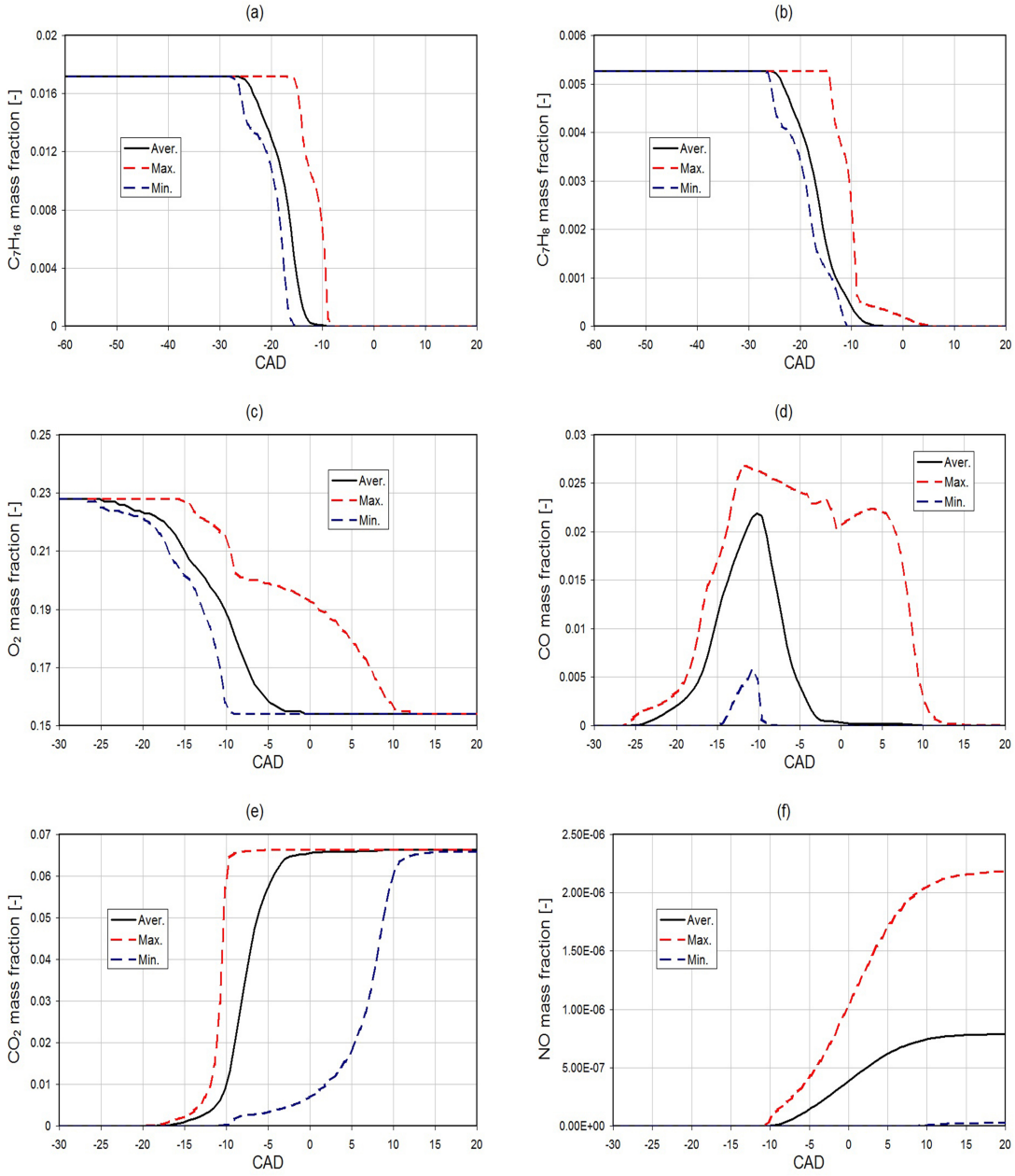

Figure 8.8: The development of chemical speceis during the combustion cylce on:(a)C_7H_{16}, (b)C_7H_8, (c)O_2, (d)CO, (e)CO_2, and (f)NO.

8.3.1 Experimental apparatus

As being stated above, the CFD-PDF model developed will be validated against the experimental results from (Maiwald et al 2005) [75]. For the experiments an air-cooled two-stroke single-cylinder Otto motor of type (L372, ILO) was used. The engine geometry was modified to allow it to operate as a HCCI engine under lean conditions. The fuel is injected in the intake air via a electromagnetic fuel injector with 100 bar pressure. Figure 8.9 shows a schematic diagram of the research engine,

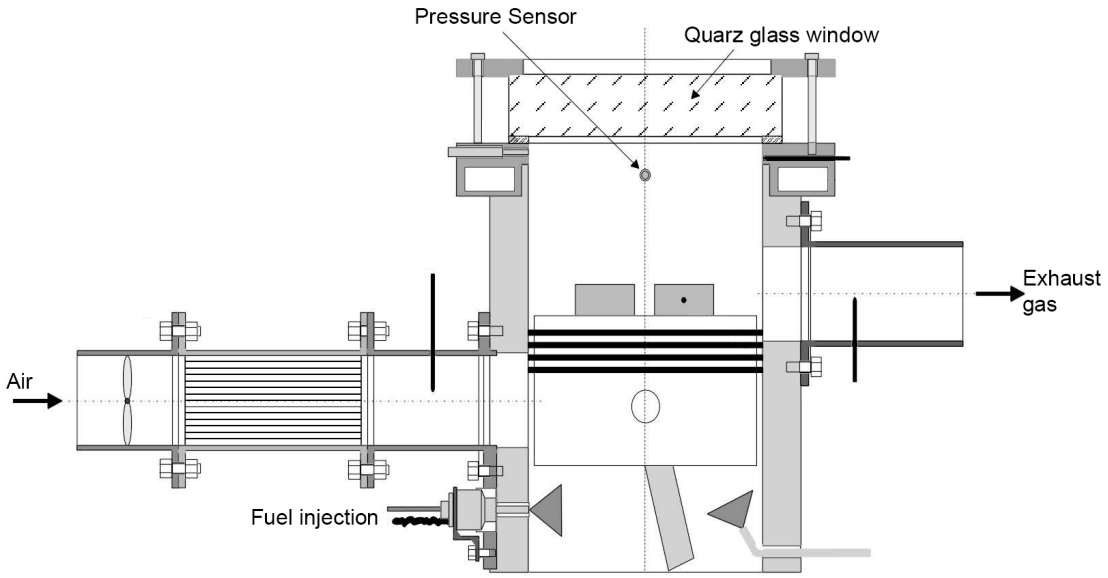

Figure 8.9: Schematic diagram of the two-stroke HCCI motor [75]

and the basic data of the engine are listed in table 8.3

Type	ILO 372, modified 2-stroke HCCI
No. of cylinders	1
Bore	80 mm
Stroke	73.84 mm
Swept volume	$371.16cm^3$
Con-rod length	148 mm
Engine speed	1000 rpm
Geo. compression ratio	ca. 20.7
Eff. compression ratio	ca. 9.0
Fuel	Iso-octane/Aceton (4:1)

Table 8.3: HCCI engine data

8.3.2 Simulation setup

For this case study, the 2D hybrid CFD-PDF model has been adopted. The model incorporates a detailed chemical reactions mechanism for iso-octane with 81 chemical species and around 796 chemical reactions developed by V. Golovichev [42].

The simulation considers only the interval after closing the intake valve and opening the exhaust valve. Therefore, particles are allowed to move between the cells but no particles are allowed to enter or leave the calculation domain. All boundaries of the domain have the same temperature of 390 K and remains constant during the entire simulation time.

Due to optical accessability, the real HCCI engine used for making these experiments was equipped with only one piston ring. Therefore, it is justified to assume a high amount of blowby taking place during the engine operation. The assumed blowby value for the present case study is 3 % [75]. Table 8.4 summarizes the main simulation data.

Initial temperature	561 ±15 K
Initial pressure	1.686 bar
No. of cells in X	10
No. of cells in Y	10
No. of particles/cell	50
Calc. start	100 BTDC
Calc. end	100 ATDC
Time step size	1.0E-5

Table 8.4: Simulation data

For the calculation of the heat transfer to the walls, the stochastic heat transfer sub-model described in the previous chapter has been adopted in this example. To determine the value of the heat transfer parameter, a simulation of an engine cycle running with air only has been conducted. The pressure curves resulting from the simulations of the air cycles were compared with corresponding pressure measurements of the engine. The value of the heat transfer parameter was modified until a best possible result was achieved. The resulting heat transfer parameter obtained from the air cycle simulation has been adopted in the computation with the fuel-air mixture cycle. Figure 8.10 shows the air cycle pressure curves obtained from the experiment, the PDF simulation, and a deterministic simulation using the Hohenberg model for the heat transfer coefficient [75, 131].

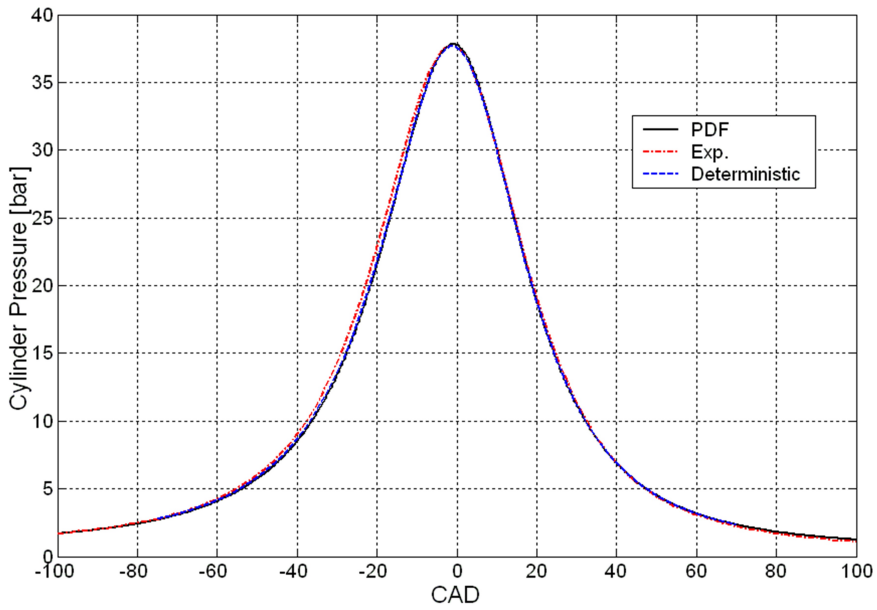

Figure 8.10: Pressure curves of an HCCI idle-run cycle

8.3.3 Results and discussion

The pressure measurements recorded from the experiments have been compared with the pressure curve obtained from the simulation after optimizing the heat transfer parameter for the simulation as shown in fig. 8.11. During the compression phase as well as the expansion phase, the pressure is slightly underestimated by the simulation. However, during the combustion phase,the pressure peak value and the combustion duration could be accurately estimated. In General, it can be said that a very good agreement between the experimental and the simulation results could be achieved. Figure 8.12 shows the temperature development in the simulation during the combustion cycle. A peak temperature of 1800 K has been reached.

In figure 8.13 , the temperature distribution in the calculation domain is shown. As can be seen, the temperature increases during the compression phase. The temperature rises until it reaches the level required for auto-ignition. Due to temperature fluctuation in the computational domain, hot spots start to appear at the locations where particle with higher temperatures exists. It can be seen that hot spots are located in the inner side of the domain while the areas near the boundaries of the domain do not ignite completely due to the effect of the heat transfer to the boundaries. After the combustion phase is completed, the temperature in the computational domain starts to drop down due to the volume expansion of the the gas mixture in the domain as well as the heat transfer to the surroundings.

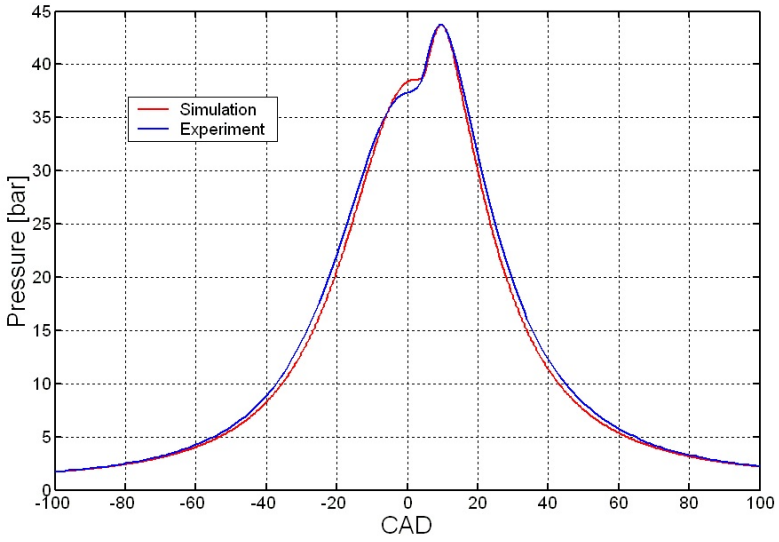

Figure 8.11: Comparison between experimental and simulation results of an HCCI engine

Figure 8.14 shows the distribution of C_8H_{18} in the domain. It has been assumed that fuel is initially homogeneously distributed in the domain. Therefore, no change in the concentration of C_8H_{18} can be observed and the temperature is high enough to start the chemical reactions. Short before TDC, C_8H_{18} begins to be exhausted in the chemical reactions. At the corners of the domain, high concentrations of C_8H_{18} remains which did not take part in the oxidization process due to the low temperature of the particles in these areas.

The CO distribution shown in figure 8.15, confirms the behavior described above. At the inner side of the domain, a low amounts of CO exist due to the oxidization of CO to CO_2 as can be seen in fig 8.16. Near the boundaries of the domain higher amounts of CO remain not oxidized due to the lower temperature of the particles in this area.

8.3.4 Sensitivity study

In this section the influence of the variation of different operation parameters on the combustion process and pollution formation will be presented. This sensitivity study will focus on the effect of the following parameters:

- initial temperature of the air-fuel mixture,
- fluctuation of initial temperature,

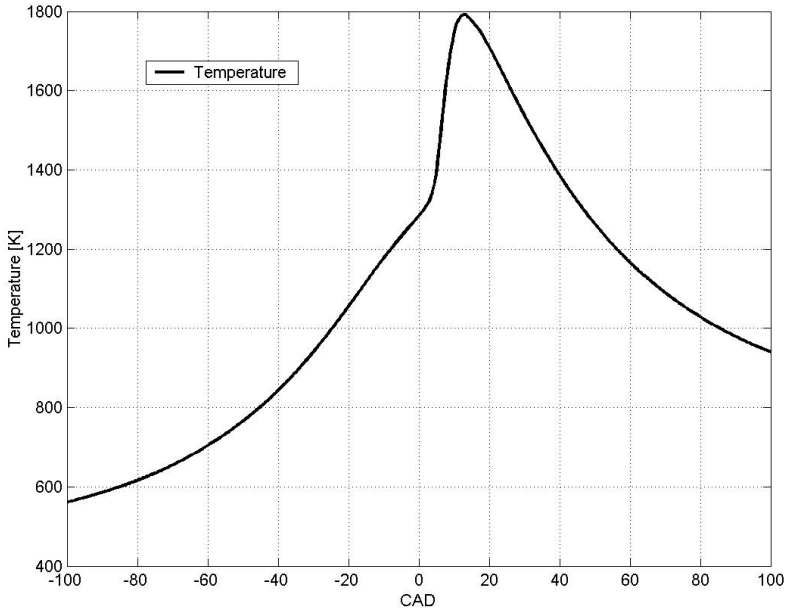

Figure 8.12: Comparison between experimental and simulation results of an HCCI engine

- exhaust gas recirculation (EGR),
- fluctuation of the initial fuel mass fraction,
- engine speed,
- air-fuel ratio,
- cylinder wall temperature,
- heat transfer coefficient,

In the following analysis, the effect of these operational parameters on ignition delay time, combustion duration, peak temperatures and pressures, amount of heat released during the combustion, and the formation of NO_x, UHC, and CO_2 will be discussed.

8.3.4.1 Initial temperature

The study of the effect of the variation of the mean initial temperature of the air-fuel mixture on the combustion characteristics will be presented in this section. Three

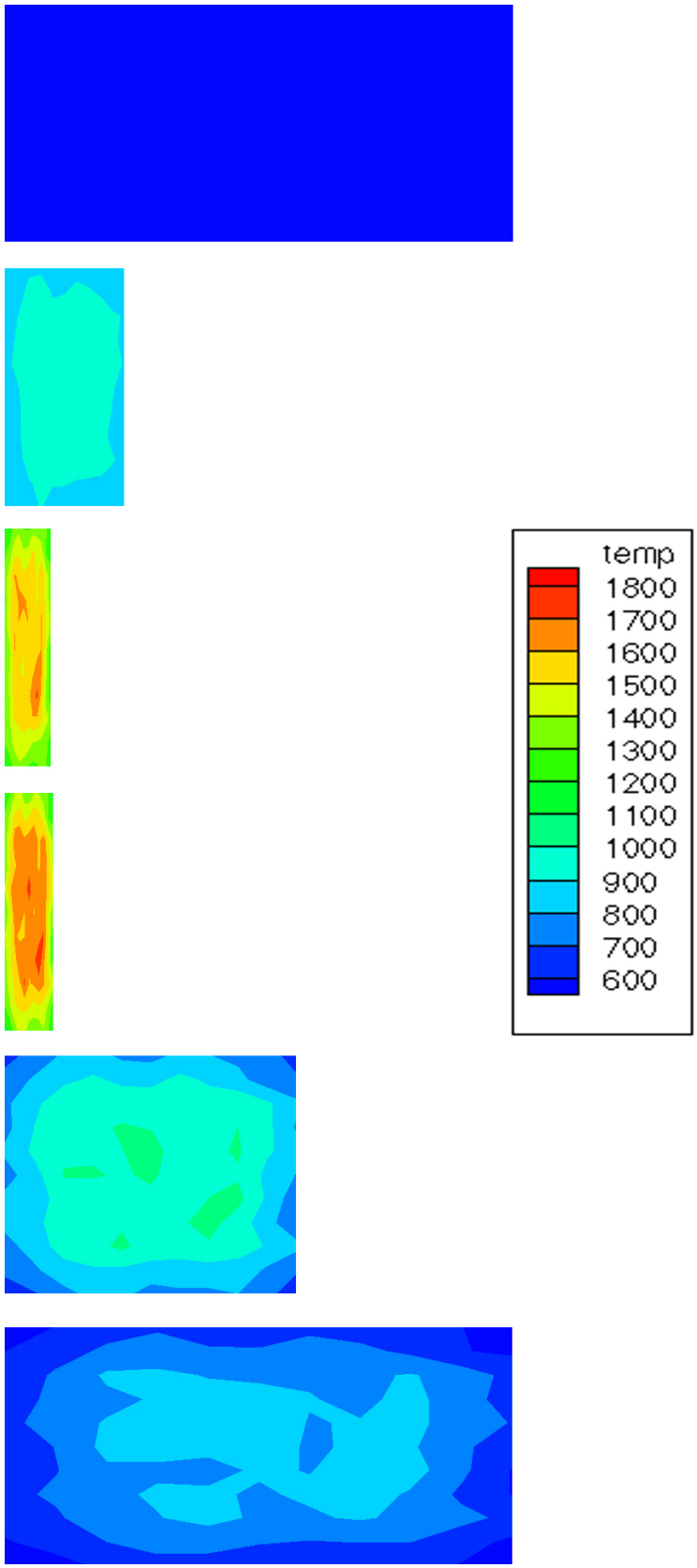

Figure 8.13: Temperature development during auto-ignition in HCCI engine

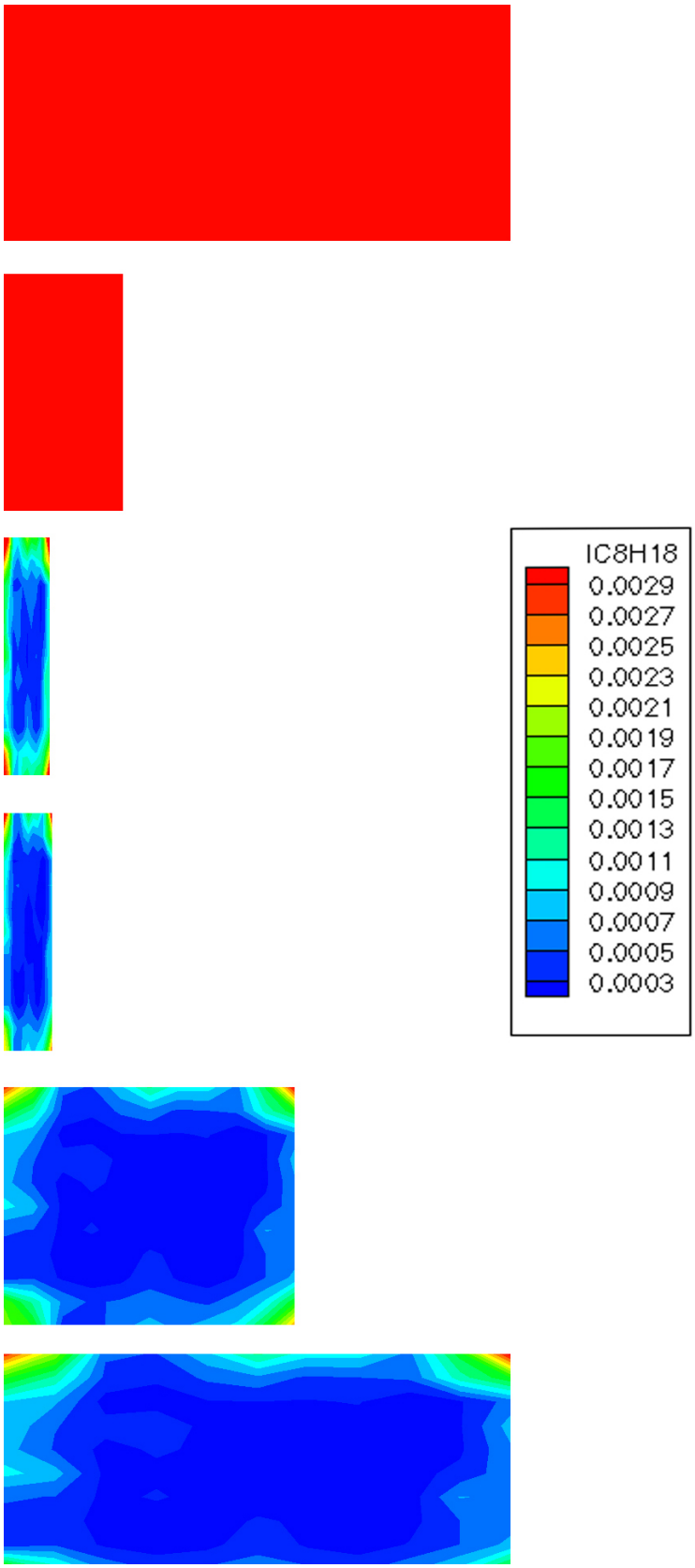

Figure 8.14: Development of C_8H_{18} mass fraction during auto-ignition in HCCI engine

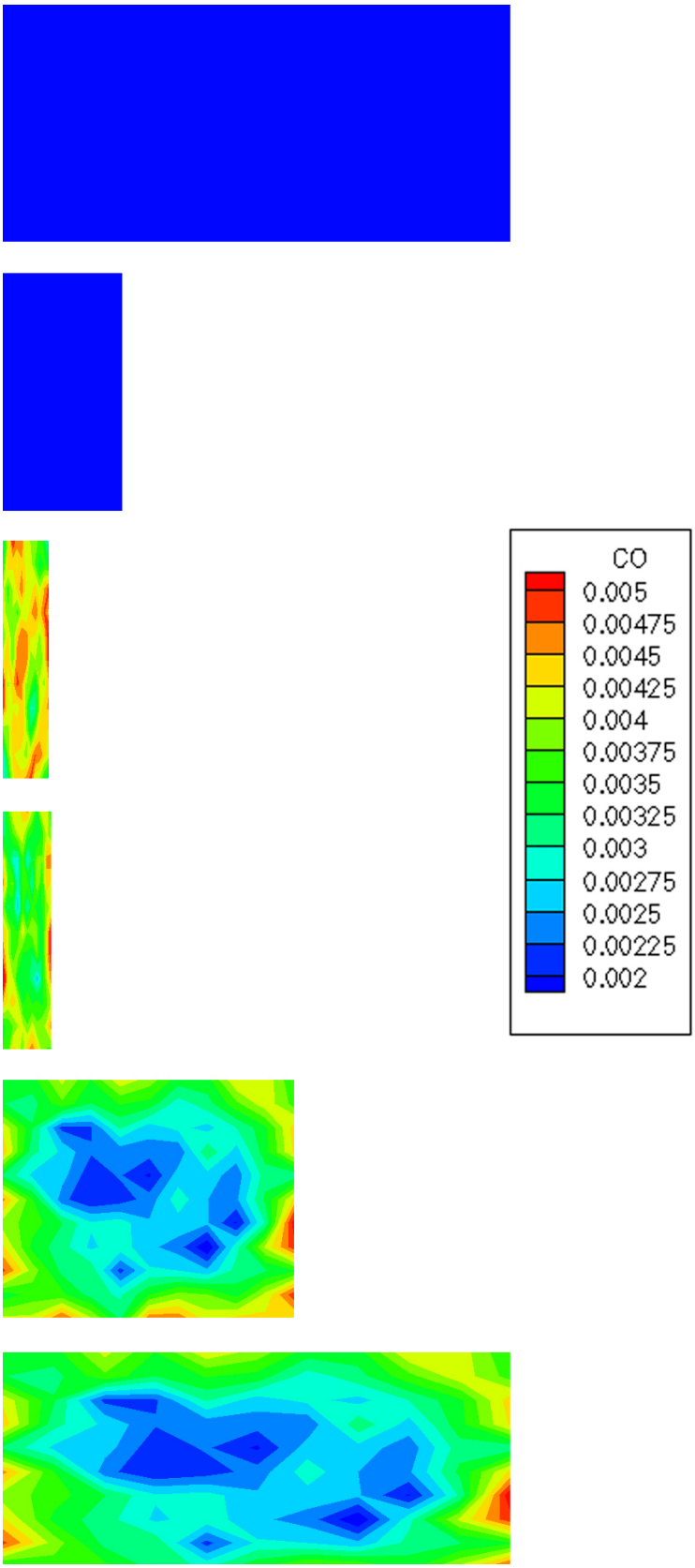

Figure 8.15: Development of CO mass fraction during auto-ignition in HCCI engine

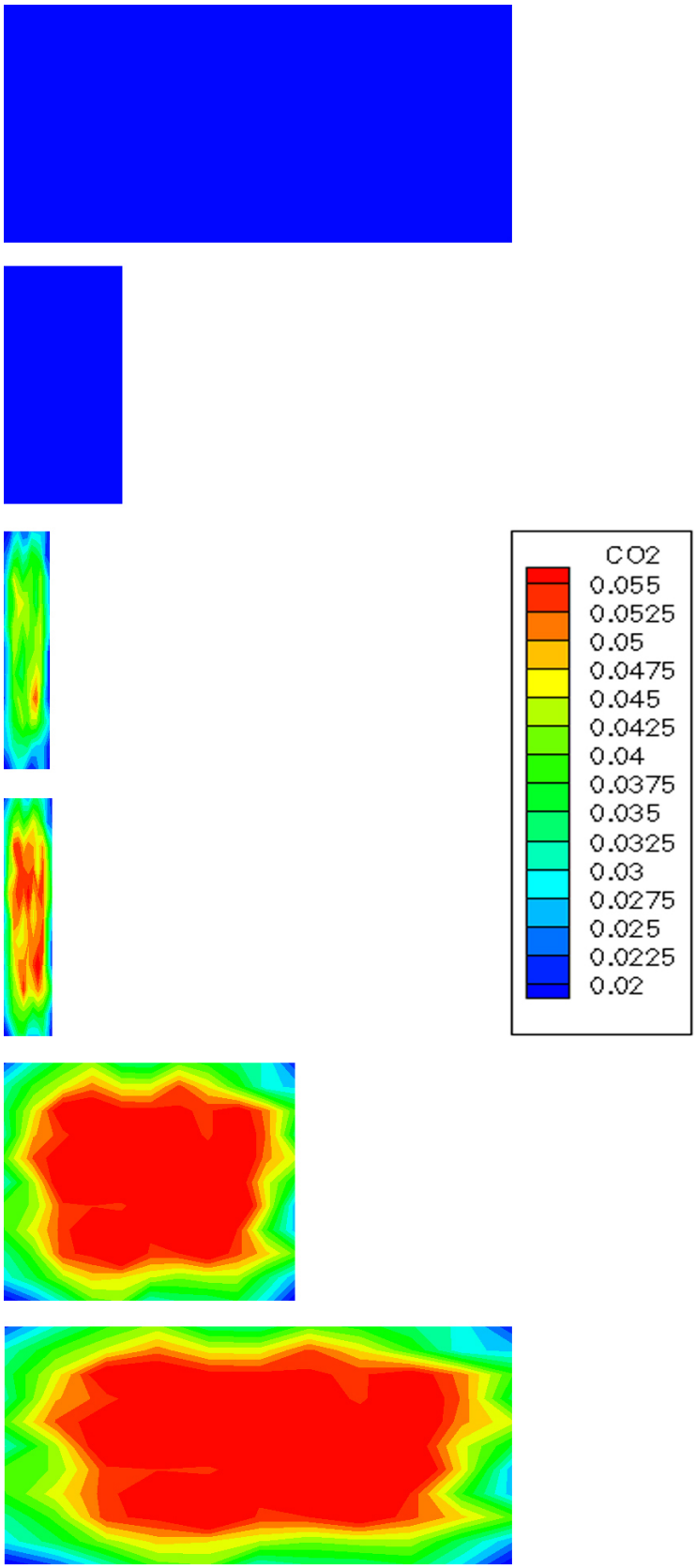

Figure 8.16: Development of CO_2 mass fraction during auto-ignition in HCCI engine

temperature variations have been simulated with initial temperatures at 100 BTDC equal to 561 , 563, and 565 K respectively.

The graphs in figure 8.17, show the effect of the variation of the mean initial temperature on the combustion process. Figure 8.17a describes the pressure development in the combustion chamber. As can be seen, the curves of the three variations follow the same route till short before TDC (nearly at 5 BTDC). At this point, the curve representing the highest initial temperature T_{ini} 565 K takes a steeper slope followed by the curve of T_{ini} of 563 K and finally T_{ini} of 561 K. In addition, it can be seen from the graph that the higher the initial temperature, the higher the pressure gradients as well as the maximum pressure reached in the combustion chamber. However, the end-pressure reached after combustion takes place is nearly the same in all cases. High pressure gradients are not desired due to the noise accompanied with the sudden pressure increase and because of the damage that may occur to engine components.

The influence of changing the initial temperature of the mixture on the temperature development is illustrated in fig 8.17b in which the same behavior as in the pressure curves can be recognized. The higher the initial temperature, the earlier the ignition delay time, and the higher the maximum temperature. Fig 8.17c compares the heat release rates of the different cases. As can be seen, the small variation of the initial temperature of only 2 K has a significant effect on the heat release rate. Increasing the initial temperature from 563 K to 565 leads to an increase in the heat release of around 30% and reducing the initial temperature from 563 K to 561 k reduces the heat release by around 40%. Moreover, the combustion duration increases with the increase of the initial temperature of the mixture.

The effect of the mean initial temperature variation on the formation of unburned hydrocarbons (UHC), carbon dioxide (CO_2), and nitrogen oxides (NO_x) is illustrated in fig 8.17d, 8.17e, and 8.17f respectively. Fig 8.17d does not show a significant change in the amount of UHC remaining in the rest gas. However, it can be seen that increasing the initial temperature will lead to a lower amount of UHC in the rest-gas due to increasing the efficiency of the combustion. This is also confirmed by fig 8.17e which describes the development of CO_2. Higher initial temperatures will lead to higher amounts of CO_2 produced because the chemical reactions are accelerated. On the other hand, the formation of NO_x mainly depends on the temperature of the combustion. In the three variations studied here, the peak temperature ranges between 1680 K for T_{ini} of 561 K and 1740 K in the case of T_{ini} of 563 K. These higher temperatures lead to the formation of thermal

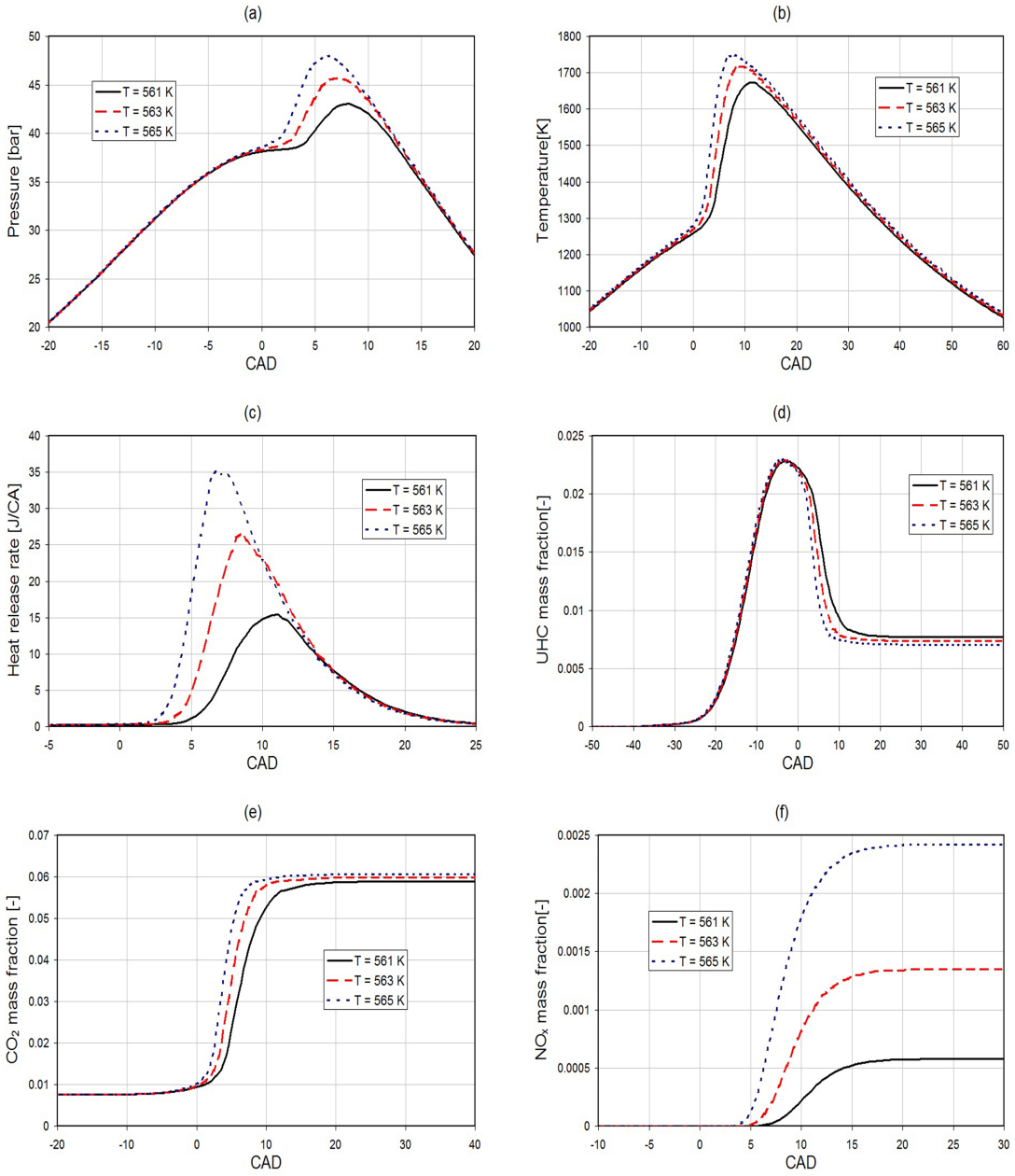

Figure 8.17: The effect of the variation of the initial temperature of the air-fuel mixture on:(a)pressure, (b)temperature, (c)heat release rate, (d)unburned hydrocarbons, (e)carbon dioxide, and (f)nitrogen oxides.

NO_x. Although, the variation in the initial temperature is not significant, a drastic difference in the amount of NO_x produced can be realized. Increasing the initial temperature by only 2 degrees has led to generating more than twice the amount of NO_x.

8.3.4.2 Initial temperature fluctuations

In this study, the variation of the initial temperature fluctuation will be considered. It is evident that in a HCCI engine, the temperature is only globally homogeneous inside the combustion chamber. Local temperature fluctuations are observed. For this study, three different examples with different initial temperature fluctuations were compared. The fluctuations assigned for these examples are ±7 K, ±15 K, and ±20 K respectively. The average temperature of 561 K is kept constant.

In figure 8.18a, the effect of varying the temperature fluctuations on pressure development in the combustion chamber is shown. Comparing the pressure curves of the three test cases, it can be seen that two contradicting factors influence the pressure rise. The first factor is the fluctuation level. Increasing the fluctuation level leads to a reduction in the maximum pressure and the pressure gradient. The other factor is ignition timing which is the crank angle at which ignition takes place, or, in other words, the compression level at which ignition occurs. Applying on our case study, in the ±7 K fluctuation case, the ignition begins at 4 ATDC while in the ±15 case the ignition starts at 1 BTDC. This means, in the first variation, ignition starts at a lower compression level in the combustion chamber which reduces the pressure rise. On the other hand, due to the lower fluctuation level of the ±7 K, higher pressure peak values can be reached compared to the other cases. The comparison between ±15 K and ±20 K shows that the pressure in the second case is slightly higher than the first one. The reason for this behavior is the fact that the influence of the fluctuation on pressure rise decreases with the increase of fluctuation level itself while the effect of the compression level remains the same. In addition, increasing the temperature fluctuation affects the start of the ignition as well. The higher the fluctuation level the earlier the combustion begin. The reason lies in the fact that higher fluctuations means that the maximum initial temperature in the combustion chamber is higher than the other two cases. This means the particles with the maximum temperatures will reach the temperature needed to start the ignition earlier. Also, pressure curves for the higher fluctuations starts to fall earlier compared to the ones with lower fluctuations.

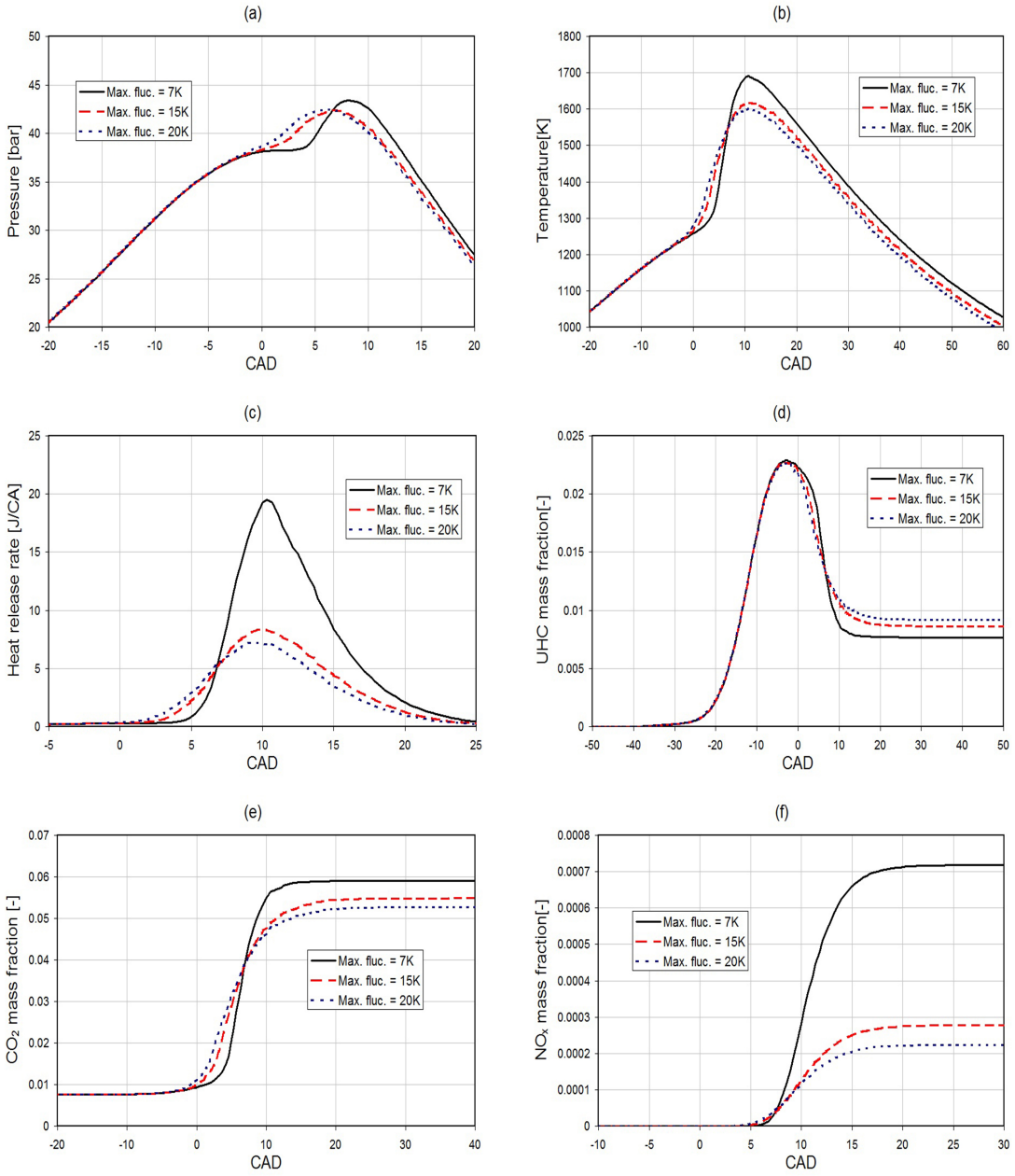

Figure 8.18: The effect of the variation of the initial temperature fluctuation on:(a)pressure, (b)temperature, (c)heat release rate, (d)unburned hydrocarbons, (e)carbon dioxide, and (f)nitrogen oxides.

Figure 8.18b shows the temperature development for the three cases. The behavior of the temperature curves is similar to the pressure curves. in fig 8.18c the heat release level is illustrated. Comparing the curves, it can be observed that when the fluctuation level is small, the heat will be released during a smaller time duration.

Figure 8.18d shows the UHC produced by the different temperature fluctuations. As can be seen, reducing the fluctuation level has a positive effect on the UHC production level. Figure 8.18e shows the amount of CO_2 produced in each case. As expected, in contrary to UHC, higher levels of CO_2 are reached when reducing the fluctuation level. Figure 8.18f, shows the correlation between the variation of the initial temperature fluctuation and NO_x formation. Increasing the fluctuation leads to a reduction of the peak combustion temperature and consequently the amount of NO_x generated.

8.3.4.3 Exhaust gas recirculation

In this section, the influence of the exhaust gas recirculation (EGR) will be analyzed. In general, there are two methods to use exhaust gases to control the combustion process in HCCI engines: the recycled exhaust gas (external EGR) and the trapped exhaust gas (internal EGR). The recycled exhaust gas method introduces cooled exhaust gases into the cylinder. This can be achieved by passing the EGR gases through an EGR cooler before they are mixed with the fresh charge in the cylinder. On the other hand, trapped exhaust gas method retains some of the burned gases into the cylinder using a negative valve overlap. This case study will concentrate on the recycled exhaust gas approach by comparing variations with different amounts of EGR.

For the current case study, variations with different amounts of EGR ranging from 0% up to 40% of the mass of the mixture have been simulated. The EGR is assumed to be completely mixed with the fresh gas. The temperature of the EGR is the same as the temperature of the initial air-fuel mixture. This means the heating effect of the EGR will not be considered in this analysis. The composition of the EGR includes the main gaseous chemical species of the burned mixture meaning H_2O, CO_2, CO, and N_2. Table 8.5 lists the EGR components considered in the simulation and their corresponding concentrations and heat capacities.

The result of the simulation is illustrated in fig 8.19. The pressure trace is shown in fig 8.19a. As can be seen, introducing EGR in the combustion chamber leads to a reduction in the peak pressure and pressure gradient as well as a delayed

combustion. It is noted that up to EGR level of 10%, auto-ignition could be achieved. At 20% EGR level incomplete auto-ignition (misfire) can be observed. Beyond the 20% EGR level, auto-ignition does not take place. Similarly, The temperature development curves in fig 8.19b show clearly that the higher the EGR level, the lower the maximum temperature reached during the combustion cycle. In fig 8.19c, the effect of EGR on heat release rate is also shown. Increasing the EGR level leads to a delay in the ignition time and a reduction in the amount of heat released. The combustion duration remains nearly unchanged for the cases where auto-ignition was completed.

In order to understand the results described above, a deeper analysis of the EGR effect is required. Introducing EGR in the combustion chamber replaces some of the inlet air and hence causes a substantial reduction in the oxygen concentration. This reduction in the amount of oxygen or air due to the existence of EGR is called the dilution effect. The other effect of EGR is the so called heat capacity effect. The chemical species H_2O and CO_2 which exist with high amounts in the burned gases have higher specific heat capacity values. Replacing some of O_2 by EGR including high amount of H_2O and CO_2 will increase the total amount of the heat capacity of the inlet charge. There is another factor affecting auto-ignition called the chemical effect. Active radicals such as OH or H contained in the EGR accelerate the chemical reactions leading to higher pressure and temperature peaks. In the current case study, no active radicals are included in the EGR composition, hence the chemical effect will not be further investigated.

Components of EGR	mass fraction (%)	C_p@1000K $KJ.Kg^{-1}.K^{-1}$
CO_2	25.0	1.234
H_2O	5.0	2.288
$N2$	70.0	1.167

Table 8.5: EGR composition introduced into the simulation model.

Dilution hardly affects the begin of combustion. Although, some of the oxygen has been replaced by EGR, the mixture still contains enough oxygen to start the auto-ignition. On the other hand, the heat capacity effect is the main factor responsible for the delay in the ignition timing. This can be understood by analyzing the effect of the temperature at the end-of-compression phase. For the same number of moles of the mixture at the same initial conditions, the charge with burned gases

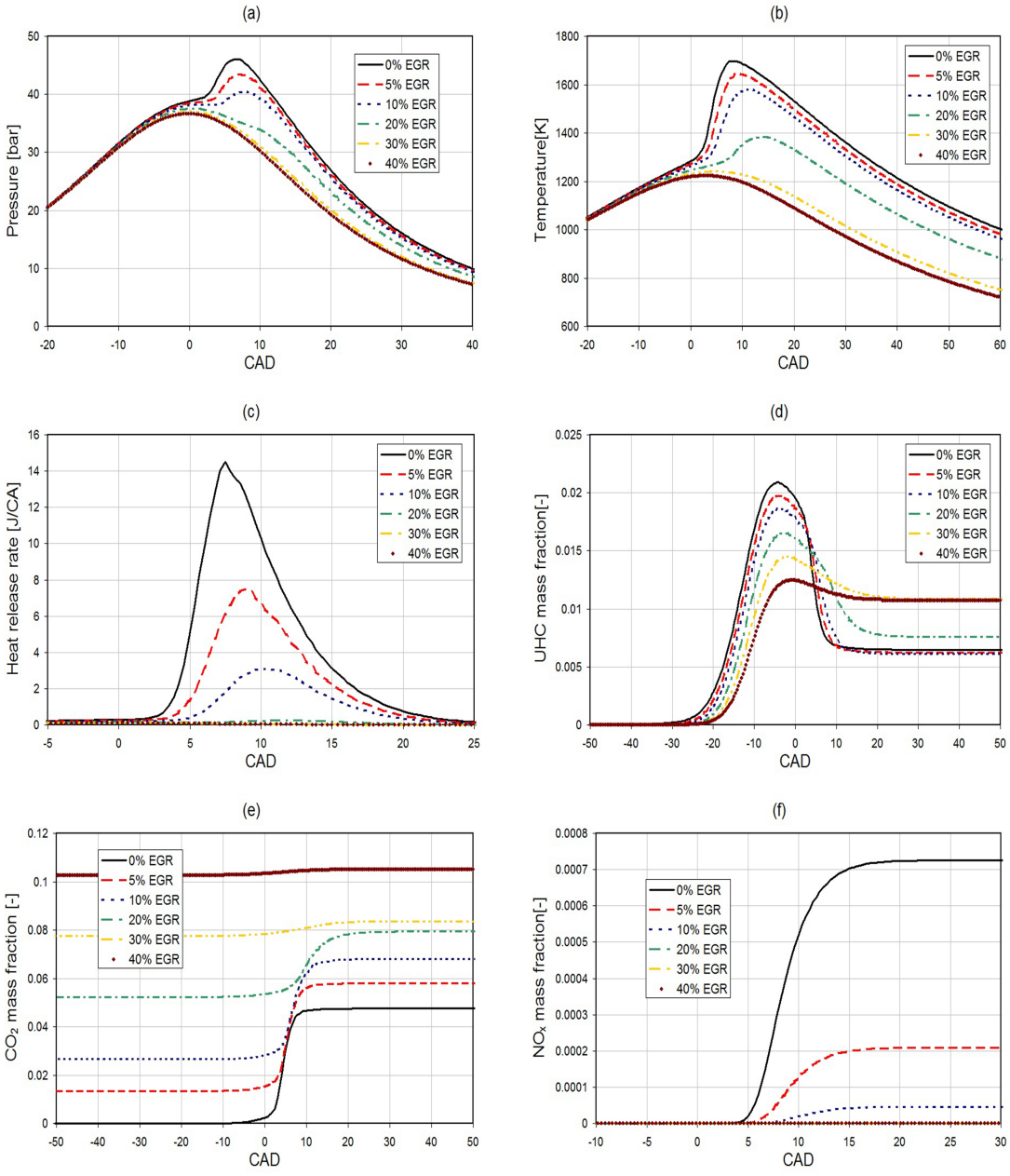

Figure 8.19: The effect of the variation of EGR on:(a)pressure, (b)temperature, (c)heat release rate, (d)unburned hydrocarbons, (e)carbon dioxide, and (f)nitrogen oxides.

including H_2O and CO_2 will reach a lower temperature at the end of the compression. Due to the high dependency of auto-ignition on temperature, the mixture with EGR will need more time until the chemical reactions reach the level at which auto-ignition takes place. Principally, both dilution and heat capacity effects increase the combustion duration. This effect could only be slightly registered in the current study. Similarly, dilution and heat capacity effects are both responsible for the reduction of the heat release rate.

The effect of EGR on the formation of emissions such as UHC, CO_2, and NO_x can be seen in figure 8.19d, 8.19e,and 8.19f respectively. Increasing EGR level from 0% to 10% reduced the intermediate peak value of the UHC. However, no significant change in the amount of UHC at the end of the combustion cycle. With 20% EGR level, complete combustion was not achieved which leads to to higher amount of UHC at the end of combustion cycle. Starting from 30% EGR level, auto-ignition was not possible. Therefore, significantly high amounts of UHC remain in the exhaust gas at the end of the cycle.

In fig 8.19e, it can be seen that increasing the EGR level causes a decrease of the amount of CO_2 produced from the combustion process. However, the total mass fraction of CO_2 increases. This can be explained by analyzing one of the EGR variations, such as 20% EGR and comparing the results to the 0% EGR. When on EGR is used, the resultant mass fraction of the CO_2 is approximately 5% of the products of the combustion process. A 20% EGR brings 5% CO_2 of the total mixture. Assuming complete combustion, additional 4% may be added to the amount of CO_2. This means that the maximum possible amount of CO_2 in the products of the combustion process may reach 9%. In the current simulation with 20% EGR, the amount of CO_2 in the products is 8%.

NO_x formation is shown in fig8.19. As can be seen, introducing an amount of 5% EGR reduced the maximum temperature from 1700 K to around 1650 K and led to an enormous decrease in the amounts of NO_x. Increasing the EGR level to 10%, reduced the temperature further to 1580 K as well as with a further NO_x reduction. Starting from EGR level of 20%, the maximum temperature is too low for NO_x formation.

8.3.4.4 Fluctuation of initial fuel mass fraction

In this section, the influence of the variation of the mass fraction of the fuel in the inlet charge will be discussed. Normally, for HCCI engines, lean conditions

are preferred. However, applying lean conditions in this case will mean that the excess of oxygen in the calculation will lead to a complete burning of the regions or particles having excess in the fuel concentration. Therefore, it has been seen that adopting lean conditions in this case will not serve the purpose of this study which is to illustrate the effect the fluctuation of the initial fuel mass fraction in the inlet charge on auto-ignition characteristics. For this reason and in order to isolate the effect of the fluctuation of the fuel mass fraction, it has been decided to adopt stoichiometric conditions for the current study.

In the current study, a range of variations ranging from 0% to 20% maximum deviation from the mean value of the fuel mass fraction in the fresh gas has been tested. The fluctuations are randomly distributed on the particles in the computational domain and the overall fluctuation takes the form of a standard gaussian distribution. Figure 8.20 shows the results of this sensitivity study. As can be seen from figure 8.20a, which describes the pressure development during the combustion cycle, increasing the maximum deviation of fuel mass fraction causes a decrease in pressure rise. Comparing the pressure curves of the different cases, it can noted that a 1% max. deviation does not have a significant effect on the pressure curve. With 5% max deviation, a slight drop in the peak pressure is realized. A further increase in the max. deviation to 10% and 20% leads a significant reduction in the peak pressure value and the steeper drop of the pressure curve afterwards.

The development of the temperature can be seen in figure 8.20b which shows a similar behavior as in the pressure curves. The peak temperature varies between 1770 K when there is no fluctuation assigned to the fuel mass fraction and 1695 K with 20% maximum fluctuation. As been mentioned earlier, stoichiometric conditions are applied for this case which led to these high temperature values. Considering the heat release rates shown on fig 8.20c, a pre-ignition phase takes place before the begin of the main combustion phase. The heat release rate curves do not show any delay in ignition while increasing the maximum fluctuation as well as no change in the combustion duration. On the other hand, increasing the maximum deviation leads to a decrease in the amount of heat released.

From the previous results it can be stated that there is a negative correlation between maximum fluctuation of fuel mass fraction on one side and pressure, temperature, and heat release rate on the other side. Under stoichiometric conditions, the maximum values of peak pressures and temperatures and heat release rates can be reached. Introducing some fluctuation in the computational domain means some of the particles will have excess fuel while others will have a shortage in the amount

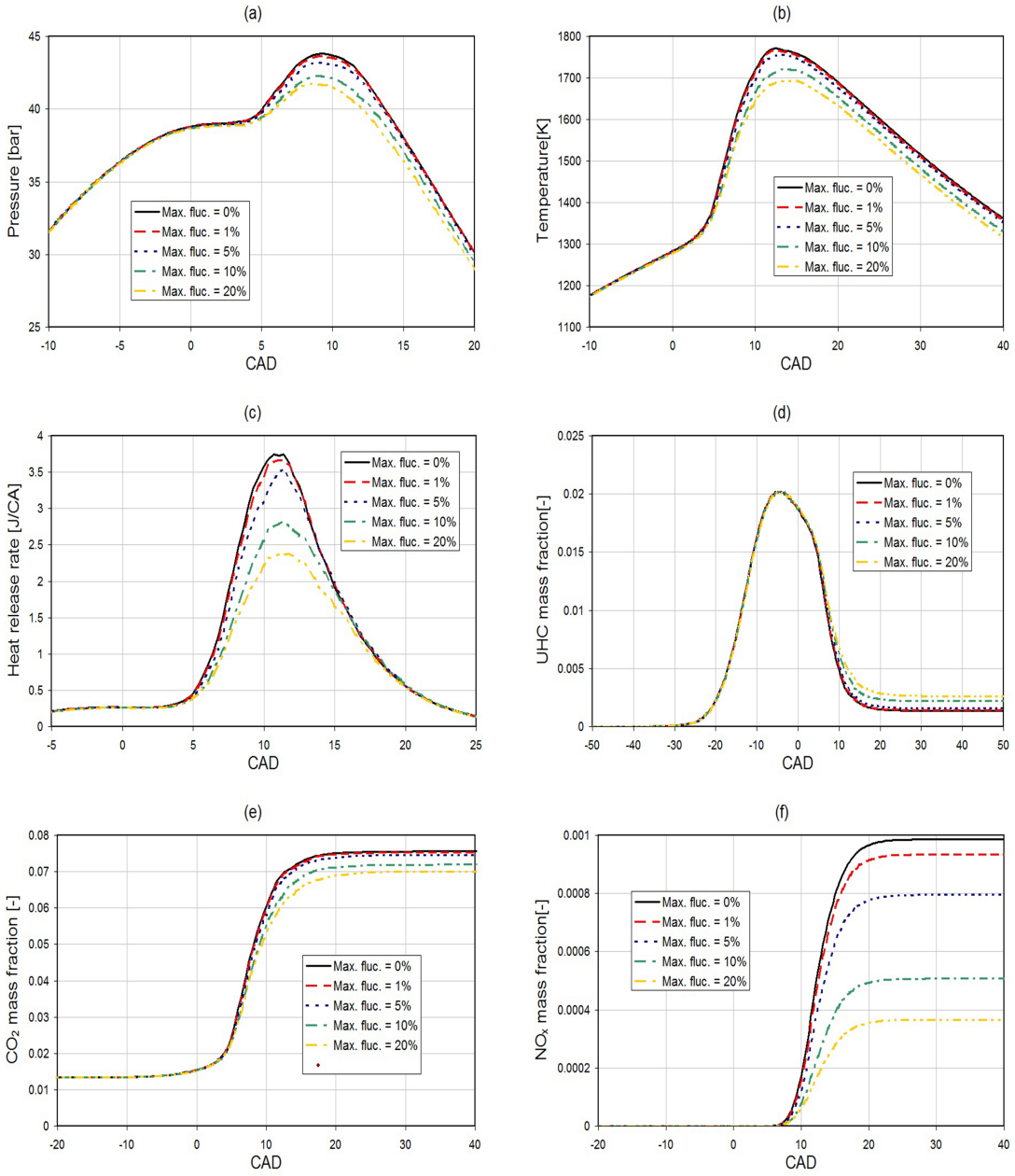

Figure 8.20: The effect of the variation of the fluctuation of the initial fuel mass fraction on:(a)pressure, (b)temperature, (c)heat release rate, (d)unburned hydrocarbons, (e)carbon dioxide, and (f)nitrogen oxides.

of fuel. This means the particles with excess fuel (rich mixture) will not have a complete combustion. on the contrary, the particles with a shortage in fuel (lean mixture) will have a combustion temperature lower than of the stoichiometric combustion. Diffusion processes reduce the difference between the different particles but does not eliminate them.

The effect of the fluctuation of the fuel mass fraction on the formation of UHC, CO_2, and NO_x is shown in figure 8.20d, figure 8.20e, and figure 8.20f respectively. It can be noticed from the graphs that for all cases, the same peak value of UHC is reached. However, increasing the fluctuation level leads to an increase in the amount of UHC produced at the end of cycle. On the contrary, the amount of CO_2 is reduced with the increase in the fluctuation level. The same effect can be seen on NO_x development due to the decrease in the combustion temperature.

8.3.4.5 Engine speed

The aim of this section is to analyze the effect of engine speed on auto-ignition characteristics. In this study, five variations have been calculated with engine speeds of 500, 800, 1000, 1100, and 1500 rpm respectively. The variation of engine speed influences the amount of heat transferred to the boundaries of the combustion chamber as well as the balance between the chemical reactions and physical processes taking place during combustion.

On figure 8.21a the pressure development for the different cases is presented. As can be seen, the highest value of pressure rise has been achieved with the slowest engine speed (the 500-rpm variation). Increasing engine speed has led to a reducing in the pressure rise and delays the begin of the ignition. As the engine speed increased to 1500 rpm engine, no auto-ignition takes place.

The same behavior is observed on figure 8.21b showing the temperature curves for the different variations. Increasing the engine speed from 500 to 1100 rpm results in a reduction of the peak temperature of more than 100 K. In addition, when comparing heat release rates shown in figure 8.21c, it can be seen that there is a significant difference in the amount of heat produced by the different variations. The slower the engine speed, the higher the heat released during combustion. Also, increasing engine speed results in a reduction in the combustion duration. In the case with 1500 rpm, there is no heat released because of misfire.

As being mentioned above, three factors govern the development of the combustion process: heat transfer to the boundaries, the chemical reactions, and diffusion

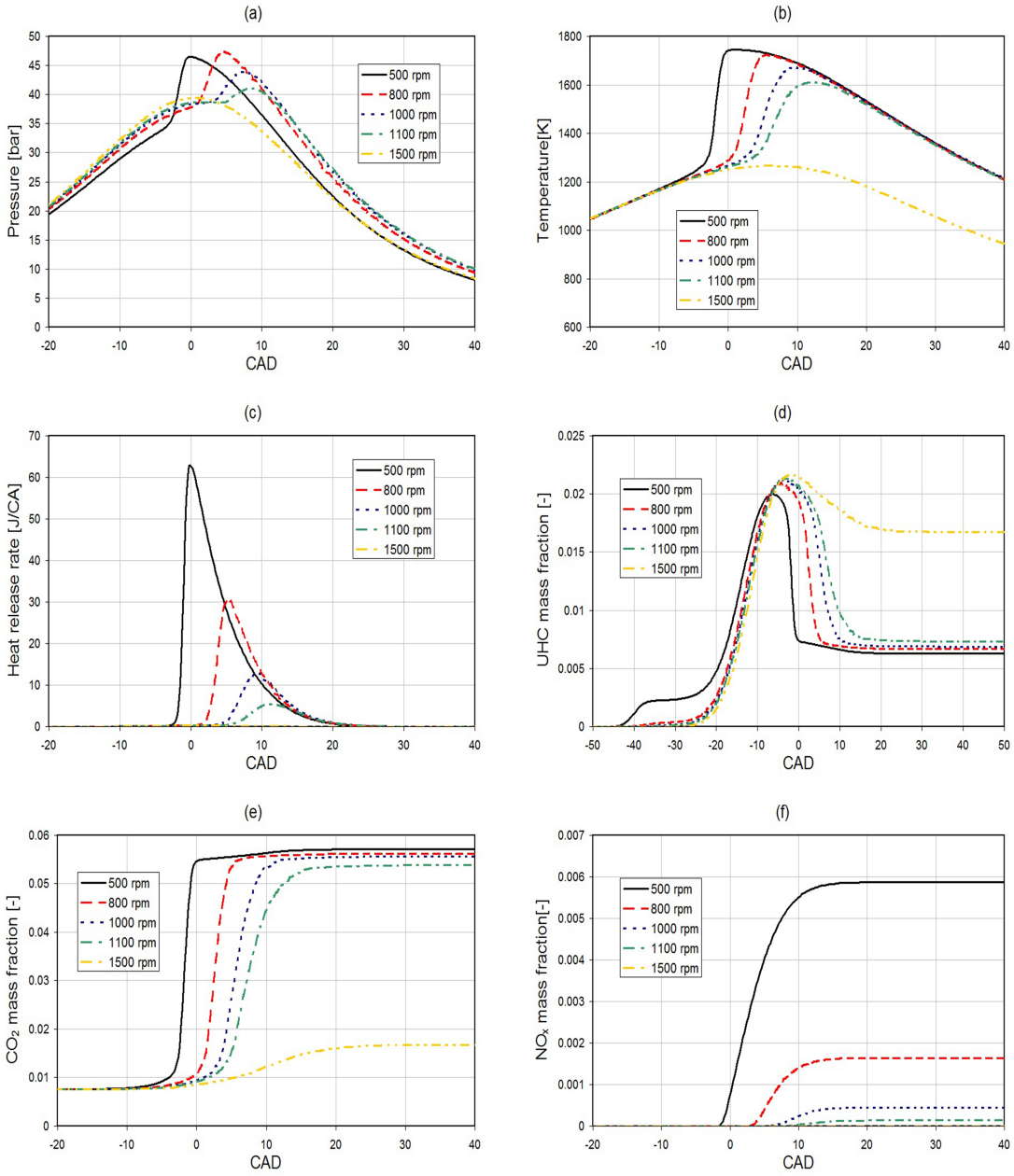

Figure 8.21: The effect of the variation of the engine speed on:(a)pressure, (b)temperature, (c)heat release rate, (d)unburned hydrocarbons, (e)carbon dioxide, and (f)nitrogen oxides.

and mixing processes. Considering the temperature curves, it can be seen that until the ignition begins, all curves follow the same route. This means, regardless how long the compression phase takes (the 500-rpm variation takes triple the time of the 1500-rpm variation), there is no significant effect registered on the temperature development. This leads to the conclusion that before auto-ignition begins, heat transfer to the boundary does not play a significant role (the influence of heat transfer to the boundaries will be discussed in details later on in this chapter). Reducing engine speed, enables the chemical reactions to have enough time to complete the combustion process. On the other hand, increasing engine speed leads to increasing the flow velocity inside the combustion chamber. A higher flow velocity may not give the chemical species enough time to react and progress the chemical reactions as in variation 1500 engine speed.

Finally, the UHC, CO_2, and NO_x are shown in figure 8.21d, figure 8.21e, and figure 8.21f respectively. Increasing engine speed leads to higher amounts of UHC due to the incomplete combustion and higher NO_x production due to the low combustion temperature while reduces the amounts of CO_2 generated due to the shorter time available for the progress of chemical reactions.

8.3.4.6 Air-fuel ratio

In this section, the effect of varying air/fuel ratio on auto-ignition will be treated. For this case study, three lean mixture variations were calculated with air/fuel ratios of 2.9, 3.2, and 3.5 respectively.

As can be seen from figure 8.22a, the pressure curves of the three variations show that increasing the air/fuel ratio causes a reduction in the pressure rise as well as a delay in the begin of auto-ignition.

The peak temperature in figure 8.22b is slightly reduced by increasing the air/fuel ratio as well. On the other hand, the heat release rate curves in figure 8.22c show no significant difference. The lower the air-fuel ratio, the earlier the begin of the heat release.

In figure 8.22d, the effect of air/fuel ratio on the production of UHC is illustrated. The curve representing the value of 2.9 air/fuel ratio reaches the highest peak value of UHC during combustion and produces the highest amount of UHC at the end of the combustion cycle. Increasing the air/fuel ratio reduces the peak value during combustion and the amount remains at the end of the combustion cycle.

Figure 8.22e shows the considers the development of CO_2 under the three vari-

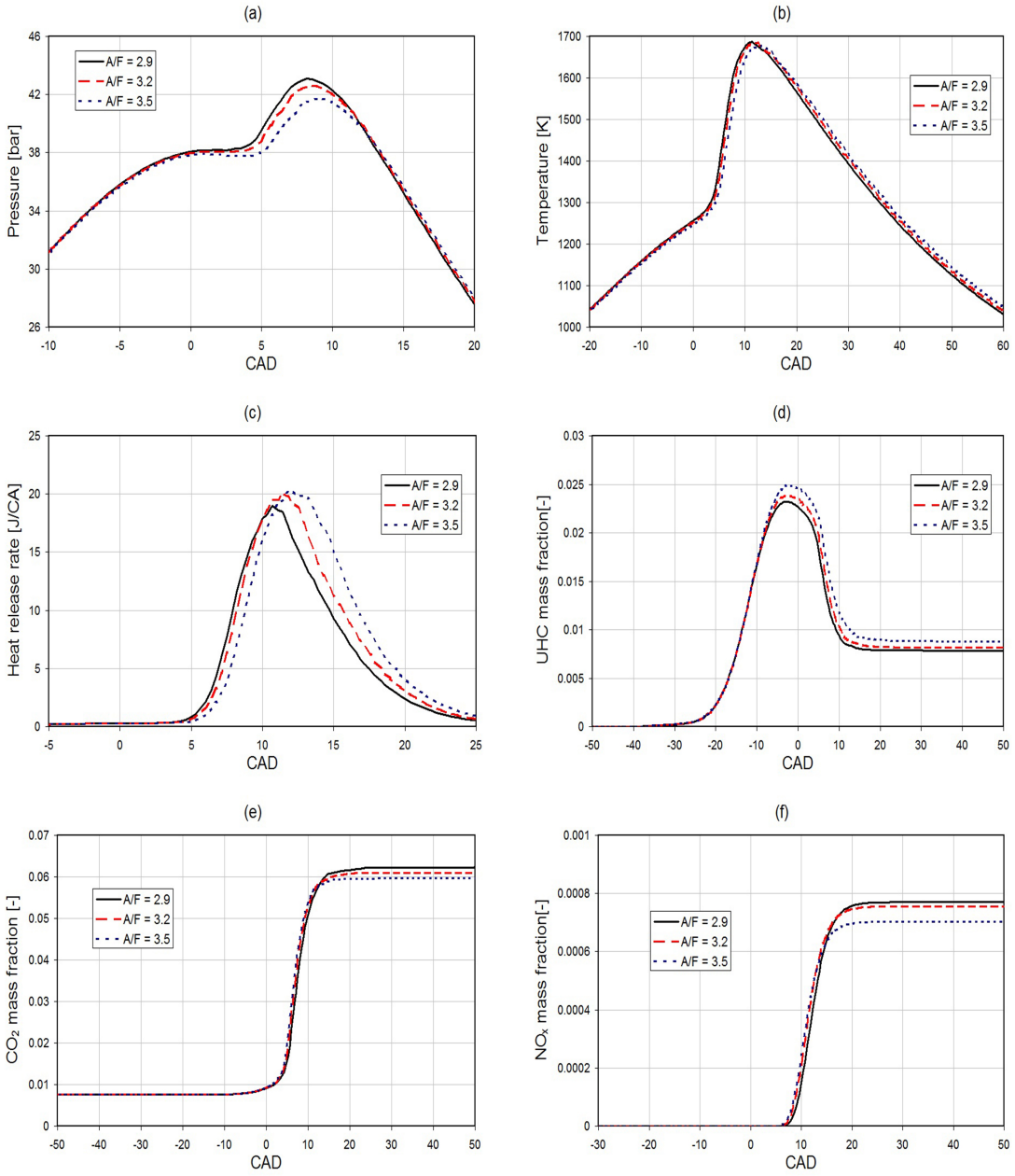

Figure 8.22: The effect of the variation of air-fuel ratio on:(a)pressure, (b)temperature, (c)heat release rate, (d)unburned hydrocarbons, (e)carbon dioxide, and (f)nitrogen oxides.

ations. The higher the air/fuel ratio, the lower the amount CO_2 in the exhaust gas.

The effect on the formation of NO_x can be seen in figure 8.22f. In this case, on the contrary to CO_2, as being discussed above, increasing air/fuel ratio leads to a reduction in the temperature and eventually to the amount of NO_x produced at the end of the combustion cycle.

8.3.4.7 Cylinder wall temperature

This section will discuss the effect of the temperature of the boundaries of combustion chamber. In this study, four variations were calculated with wall temperatures of 330 K, 350 K, 370 K, and 390 K. In all variations, the same temperature has been assigned to all boundaries of the computational domain and it remains constant during the entire calculation time. As can be seen in figure 8.23a, only slight differences in the pressure rise could be observed. The curve representing the case of 390 K wall temperature achieves the highest pressure peak. This means that the higher the wall temperature, the higher the peak pressure reached. The same observations mentioned above applies as well to figure 8.23b showing the temperature curves. In addition, from the heat transfer rate curves shown in figure 8.23c, it can be noted that increasing wall temperature increases the heat released in the combustion chamber. Higher wall temperatures means lower heat transfer to the cylinder walls which enables the particles near the boundary to maintain high temperature gained due to the compression of the combustion chamber as well as chemical reactions. This allows the boundary layer particles to ignite which increases the amount of heat released during combustion. No significant change in ignition delay time or in the combustion duration could be realized between the calculated variations of wall temperature.

From the previous results, it can be concluded that the variation of the temperature of combustion chamber should not have a significant influence on the combustion cycle. Although, a 50 K difference between the highest and the lowest wall temperatures, the influence on heat flux to the walls is negligible. As can be seen from equation 8.5, due to the big difference between the temperature of mixture inside the combustion chamber and the wall temperature,which may reach 1600 K, the effect of 50 K difference will not be significant for the heat flux and eventually will have a minimal effect on the combustion progress inside the cylinder.

$$q = \alpha_w A(T_g - T_w) \tag{8.5}$$

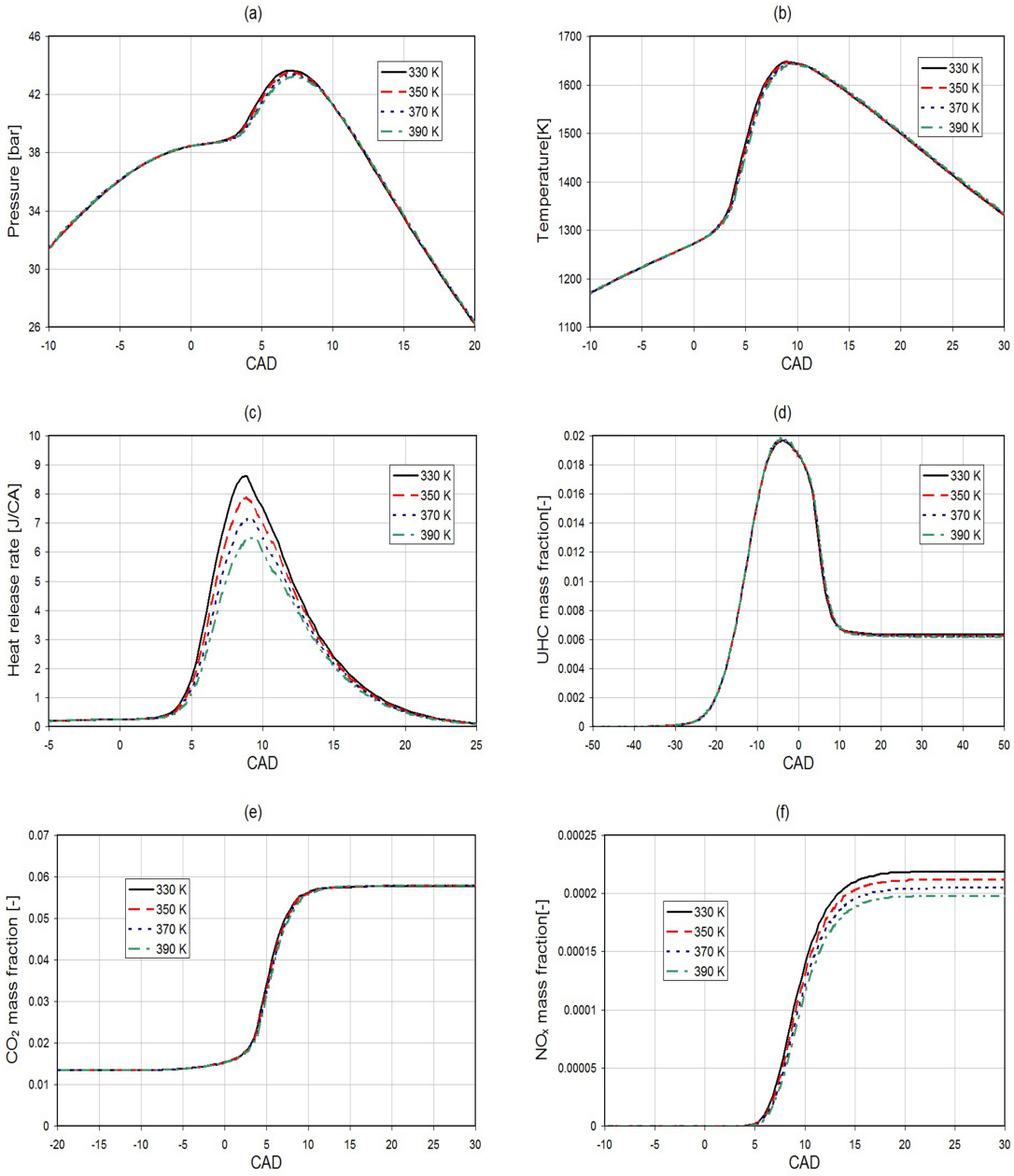

Figure 8.23: The effect of the variation cylinder wall temperature on:(a)pressure, (b)temperature, (c)heat release rate, (d)unburned hydrocarbons, (e)carbon dioxide, and (f)nitrogen oxides.

where q is the heat flux, α_w the heat transfer coefficient, A is the heat transfer surface area, T_g, and $T_{w)}$ is the wall temperature of the combustion chamber.

In figure 8.23d and 8.23e, the curves representing UHC and CO_2 development are nearly identical. Also, as being shown in figure 8.23f, the higher the wall temperature, the higher the amount of NO_x produced.

8.3.4.8 Heat transfer coefficient

As being mentioned earlier in this chapter, a statistical sub-model for calculating the heat transfer to the cylinder walls has been developed and implemented in the this program, see equations 6.4 and 6.5. For this model a parameter has been defined to control the decay of the temperatures of the particles in the boundary layer due to heat transfer to the cylinder walls.

In this section the effect of the variation of the heat transfer parameter α_w will be discussed. A series of four variations have been calculated using α_w values ranging from 0.1 to 0.7. The pressure curves in figure 8.24a show the effect of increasing this parameter on the pressure development. As can be seen, the higher the value of α_w, the lower the pressure rise and the pressure curve starts to fall earlier.

In figure 8.24b, the temperature curves are shown. Again, it can be noted that the variation of this parameter has a significant effect on the temperature during and after auto-ignition. The heat transfer rate curves in figure 8.24c show no delay in the auto-ignition caused by varying the heat transfer parameter. On the other hand, the amount of heat release is reduced by increasing the α_w parameter. Also, increasing α_w leads to an increase in the combustion duration.

finally, figure 8.24d show that increasing α_w leads to an increase in the amounts of UHC produced at the end of the cycle, although the maximum values reached during auto-ignition remain the same. On the other hand, figure 8.24e shows that more CO_2 is produced when α_w is increased. In figure 8.24f the amount of NO_x vary drastically by changing the value of the wall heat transfer coefficient α_w due to the high dependency of NO_x formation on temperature.

8.3.4.9 General remarks on the sensitivity analysis

The sensitivity study presented above discussed the influence of the variation of certain parameters on the combustion process. The observations from this study can be summarized in the the following points:

- Increasing the initial temperature of the fuel-air mixture leads to an increase in

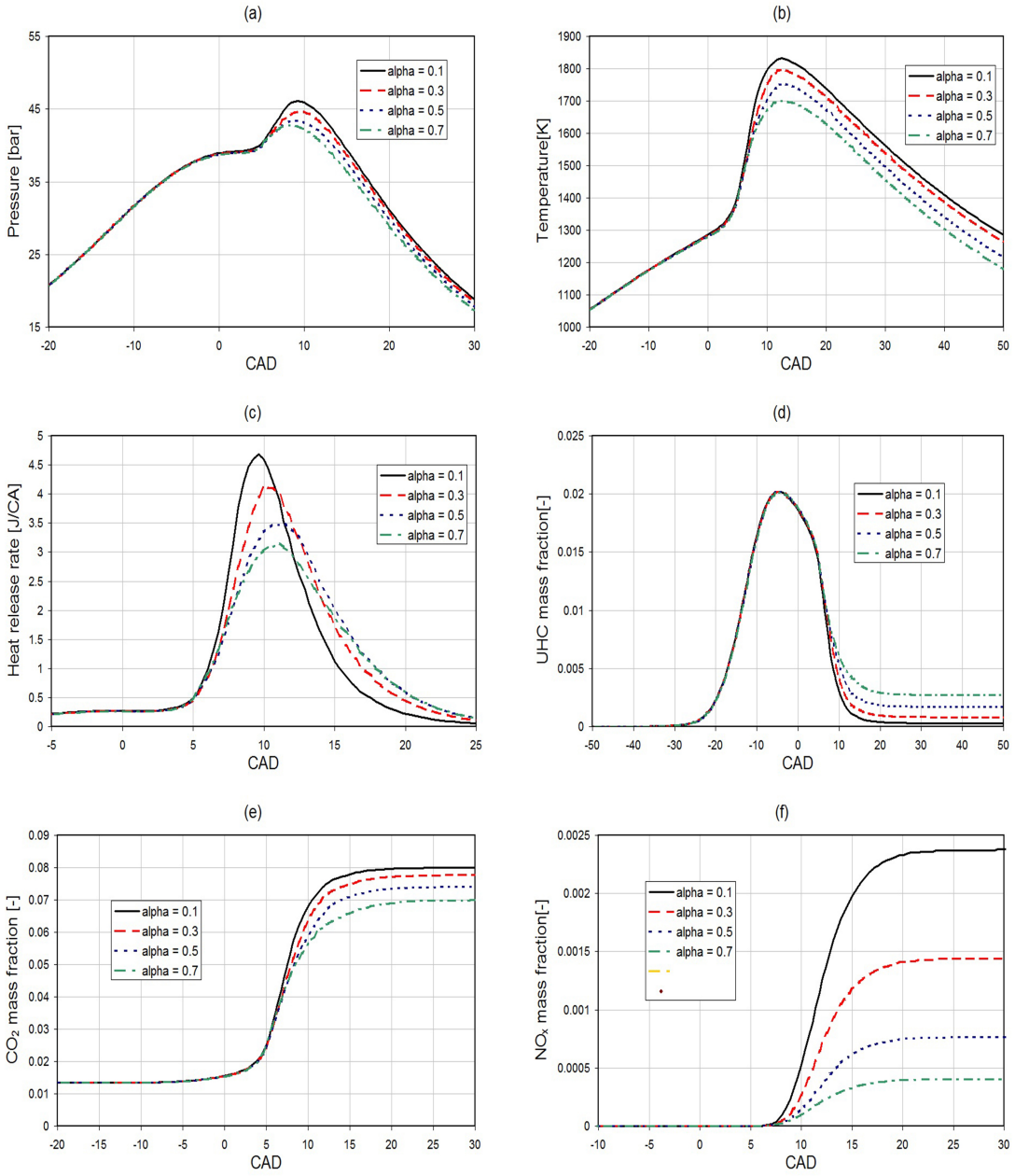

Figure 8.24: The effect of the variation of the heat transfer coefficient on:(a)pressure, (b)temperature, (c)heat release rate, (d)unburned hydrocarbons, (e)carbon dioxide, and (f)nitrogen oxides.

the peak combustion pressure and temperature. The amount of the produced UHC is reduced while the amount of CO_2 and NO_x increase due to the higher temperature

- Increasing the fluctuation of the initial temperature leads to a reduction in the peak combustion pressure and temperature as well as a reduction in the CO_2 and NO_x formed. On the other hand, the amount of the UHC increases.
- Increasing the amount of internal EGR at the beginning of the combustion cycle leads to a a reduction in the peak combustion pressure and temperature as well as a reduction in the NO_x formed. The amounts of the UHC are increased in the exhaust gases. The amount of CO_2 is also increased due to increasing the global EGR percentage in the initial mixture.
- Increasing the fluctuation of the initial fuel mass fraction leads to decreasing the pressure and temperature rise, an increase in the UHC generated, and a reduction in CO_2 and NO_x produced.
- Increasing engine speed reduces the peak pressure and temperature due to the short mixing time. Consequently, the amount of UHC is increased in the exhaust gases while the amounts of CO_2 and NO_x are reduced.
- Increasing the air-fuel ratio shows a decreases the peak pressure and temperature as well as the amounts of UHC, CO_2, and NO_x produced.
- The temperature of the walls of combustion cylinder has no significant influence on the generated pressure and temperature or on the evolution of the different chemical species.
- Finally, increasing the heat transfer coefficient leads to reducing the peak pressure and temperature as well as the amounts of CO_2, and NO_x formed during the combustion process. On the other hand, the amounts of UHC are increased.

Generally, it can be said that controlling the pressure and temperature rise as well as pollution formation in the HCCI engine can be achieved by controlling the analyzed parameters. However, in the practice, it is still difficult to exactly control some of these parameters such as the fluctuation of the intake temperature or the fuel mass fraction. It is more convenient to control the amount of EGR in the combustion chamber or the air-fuel ratio.

Chapter 9

Conclusion and Perspectives

9.1 Summary of work

The work presented in this study aims at developing a numerical model for the simulation of auto-ignition in internal combustion engines. The developed model is based on the hybrid CFD-PDF method in which the Lagrangian Monte Carlo algorithm is used for the solving the joint probability mass density function of velocity and scalars. In this method, the solution is obtained by solving the stochastic differential equations of the mathematical particles. The evolution of the particle velocity is obtained using the Langevin model. Micro-mixing is calculated via the modified curl's method. The main benefit of the Monte Carlo approach is that the method allows for an exact treatment of the chemical kinetics. Coupled to the lagrangian Monte Carlo, is an Eulerian finite volume model used to solve the mean field quantities such as velocity, turbulent kinetic energy, and dissipation and the mean pressure field.

In the presented numerical model, the following features have been included:

- Simulating fluctuations of temperature and mixture fraction in the cylinder.
- Local temperature inhomogeneities due to the thermal interaction between combustion chamber boundaries and the particles in the boundary layer.
- Volume change due to piston movement.
- Flexible initialization of particle properties model:
  - single particle (homogeneous reactor)
  - two-particle model
  - multi-particle model

  - symmetrical gaussian distribution
  - non-symmetrical gaussian distribution
  - statistical distribution based on finite-volume mean field values

- Mass loss due to blow-by effect.

- Calculation of independent sub-domains (Monitoring points) simultaneously.

The Onset of auto-ignition depends mainly on the chemical kinetics and the ignition delay time depends on the temperature and pressure history. Therefore, detailed chemical reaction mechanisms have been coupled to the developed model.

For the validation of the numerical model, experimental measurements with different engine types and fuels have been used. The first test case is a two-stroke SI engine. A one-zone multi-cell model is used to simulate auto-ignition in the unburned gas region. The pressure measurements have been submitted to the calculation model and the CH_2O concentrations were used to validate the model. A good agreement between the experimental measurements and the simulation results is observed.

The second test case incorporates a four-stroke diesel-modified HCCI engine. For this test case, a hybrid CFD-PDF model has been implemented. However, a global Woschni heat transfer model is used for the calculation of the thermal interaction with the cylinder walls. Excellent agreement of the pressure evolution results obtained from the simulation and experimental measurements is achieved.

The final test case represents a two stroke HCCI engine operating with a gasoline fuel. For the calculation of combustion process in this case, the hybrid CFD-PDF model have been used including a local boundary layer model for the calculation of heat transfer to the boundaries. The heat transfer coefficient is determined by comparing the idle-cycle measurements to the simulations. The pressure development results of the simulation of a combustion cycle is compared to the experimental measurements. A very good agreement was achieved.

The latter study is extended to incorporate a sensitivity analysis of different operational parameters of the HCCI engine. The parameters analyzed by the study include,

- initial fuel-air mixture temperature,

- fluctuation of initial temperature of the mixture,

- exhaust gas recirculation,

- fluctuation of the initial fuel mass fraction,
- engine speed,
- air-fuel ratio of the mixture,
- cylinder wall temperature,
- heat transfer parameter.

The influence of the previous parameters on some features of the combustion process, such as pressure and temperature rise, heat release rate, and pollutant formation, has been examined. The results are discussed in details in chapter 8. In table 9.1, the correlation between the study parameters and the discussed features of combustion process are presented, where the signs (+) and (-) show whether a positive or a negative correlation has been observed by the simulations.

parameter	press./ temp. rise	UHC	CO_2	NO_x
init. A/F mixture temp.	(+)	(−)	(+)	(+)
variance of init. temp.	(−)	(+)	(−)	(−)
EGR	(−)	(+)	(+)	(−)
variance of init. fuel mass frac.	(−)	(+)	(−)	(−)
engine speed	(−)	(+)	(−)	(−)
A/F ratio of the mixture	(−)	(−)	(−)	(−)
cylinder wall temperature	(+)	(−)	(+)	(+)
heat transfer coefficient	(−)	(+)	(−)	(−)

Table 9.1: Summary of sensitivity analysis results.

9.2 Future work

The work presented in this dissertation is characterized by being an application-oriented model. However, for an industrial application, some modeling features have to be further developed. The calculation of the combustion processes in industrial IC engines with complex geometries requires that the Monte Carlo model should be upgraded from a two-dimensional to a three-dimensional model in order to be capable of accurately describing the complex 3D-flow behavior in the combustion chamber. The Monte Carlo method is characterized by the slow conversion.

Therefore, incorporating adaptive particle schemes in the computational model in order to accelerate the calculation time while maintaining the solution accuracy.

In addition to the above, the parallelization of the Monte Carlo code will lead to a significant reduction in the calculation time. When calculating turbulent reactive flow with detailed chemistry mechanism, around 90 % of the machine computing time is consumed in calculating the update of the chemical source term which is executed for each particle independently. Therefore, it is fairly simple to parallelize this step with shared memory programming on Multi-processor computers.

The future development of the transported pdf method is expected to focus on improving the turbulence models by coupling the Monte Carlo method to a Large-eddy simulation model [106, 120, 87]. Moreover, There is research work ongoing in developing mixing model which consider the localness in scalar space and in the combination in micro mixing and chemical reactions [127]. Finally, heat transfer by radiation plays an important role in IC engines. Incorporating radiation in the transported-pdf method will be a significant step for the commercial application of this method.

References

[1] Homogeneous charge compression ignition (hcci) technology. Technical report, US Department of Energy, 2001.

[2] J. Abraham, F. A. Williams, and F. V. Bracco. A discussion of turbulent flame structure in premixed charges. *SAE Paper 850345 in Engine Combustion Analysis: New Approaches*, page 156, 1985.

[3] W. R. B. E. Launder, A. Morse and D. B. Spalding. The prediction of free shear flows - a comparison of the performance of six turbulence models. In *Proc. of NASA Conf. on Free Shear Flows*, 1972.

[4] M. Bargende. *Berechnung und Analyse innermotorischer Vorgnge bei Verbrennungsmotoren*. Institut fr Kraftfahrwesen und Verbrennungsmotoren Universitt Stuttgart, 1997.

[5] J. A. Barnard. *Flame and Combustion*. Chapman and Hall, 1985.

[6] R. A. Baurle, A. T. Hsu, and H. A. Hassan. Assumed and evolution PDF's in supersonic turbulent combustion calculations. *AIAA Journal of Propulsion and Power*, 11:1132–1138, 1995.

[7] R. Bender, U. Maas, S. Boeckle, J.Katzenwadel, C. Schulz, and J. Wolfrum. Monte-Carlo-PDF-simulation and Raman/Rayleigh-measurement of a turbulent premixed flame. *accepted for presentation on the 17$^{\text{th}}$ International Colloquium on the Dynamics of Explosions and Reactive Systems*, 1999.

[8] S. W. Benson. The kinetics and thermochemisty of chemical oxidation with application to combustion and flames. *Prog. Energy Combust.Sci.*, 7:125–134, 1981.

[9] P. G. Beretta, M. Rashidi, and J. C. Keck. Turbulent flame propagation and combustion in spark ignition engines. *Combust. Flame*, 52:217–245, 1983.

[10] R. W. Bilger. Nonpremixed turbulent reacting flows. In *Topics in Applied Physics, 44*, page 65. Springer-Verlag, 1980.

[11] R. Bird, W. Stewart, and E. Lightfoot. *Transport Phenomena*. Wiley Interscience, New York, 1960.

[12] R. Borghi. In C. Bruno and C. Casci, editors, *Recent Advances in aeronautical science*. Pergamon, London, 1984.

[13] R. Borghi. Turbulent combustion modelling. *Prog. Energ. Comb. Sci.*, 14:245–292, 1988.

[14] P. Bradshaw, T. Cebeci, and J. H. Whitelaw. *Engineering calculation methods for turbulent flow*. Academic Press, London, 1981.

[15] C. Chevalier. *Entwicklung eines detaillierten Reaktionsmechanismus zur Modellierung der Verbrennungsprozesse von Kohlenwasserstoffen bei Hoch- und Niedertemperaturbedingungen*. PhD thesis, Institut für Technische Verbrennung, Universität Stuttgart, 1993.

[16] C. Chevalier, J. Pitz, J. Warnatz, C. Westbrook, and H. Melenk. Hydrocarbon ignition: automatic generation of reaction mechanisms applications to modeling of engine knock. In *24*$^{\text{th}}$ *Symposium (International) on Combustion*, volume 93. The Combustion Institute, Pittsburgh, PA, 1990.

[17] C. Chevalier, J. Warnatz, and H. Melenk. Automatic generation of reaction mechanisms for the description of oxidation of higher hydrocarbons. *Ber, Bunsenges. Phys. Chem.*, 94:1362, 1990.

[18] M. Christensen. *HCCI Combustion - Engine Operation and Emission Characteristics*. PhD thesis, Lund Institute of Technology, 2002.

[19] M. Christensen and B. Johansen. Influence of mixture quality on homogeneous charge compression ignition. *SAE Paper 982454*, 1998.

[20] M. Christensen, B. Johansen, and P. Einewall. A homogeneous charge compression ignition (hcci) using iso-octane, ethanol, and natural gas - a comparison with spark ignition operation. *SAE Paper 972874*, 1997.

[21] C. Ciccarelli. *Mech 435 Internal Combustion Engines*. 2009.

[22] G. Comte-Bellot and S. Corsin. *J. Fluid Mech.*, 18:353–378, 1964.

[23] S. M. Correa. A direct comparison of pair-exchange and IEM models in premixed combustion. *Combustion and Flame*, 103:194–206, 1995.

[24] S. M. Correa and S. B. Pope. Comparison of a Monte Carlo PDF/finite-volume mean flow model with bluff-body Raman data. In *24*$^{\text{th}}$ *Symposium (International) on Combustion*, pages 279–285. The Combustion Institute, Pittsburgh, PA, 1992.

[25] R. L. Curl. Dispersed phase mixing: 1. theory and effects in simple reactors. *A.I.Ch.E. Journal*, 9:175–181, 1963.

[26] P. Deuflhard, E. Hairer, and J. Zugck. *Numerical Mathematics*, 51:501, 1987.

[27] P. Deuflhard and U. Nowak. Extrapolation integrators for quasilinear implicit ode's. In P. Deuflhard and B. Enquist, editors, *Large Scale Scientific Computing. Progress in Scientific Computing Vol. 7*. Birkhäuser, Boston, Basel, Stuttgart, 1987.

[28] C. Dopazo. Relaxation of initial probability density functions in the turbulent convection of scalar fields. *Phys. Fluids*, 22:20–30, 1979.

[29] C. Dopazo. Recent developments in pdf methods. In P. A. Libby and F. A. Williams, editors, *Turbulent Reacting Flows*, pages 375–474. Academic Press, New York, 1994.

[30] C. Dopazo and E. E. O'Brien. An approach to the autoignition of a turbulent mixture. *Acta Astronaut*, 1:1239, 1974.

[31] A. Douaud and P. Eyzat. Digitap-an online aquisition and processing system for instantaneous engine data-applications. *SAE paper 770218*, 1977.

[32] P. Eckert, S. Kong, and R. Reitz. Modeling autoignition and engine knock under spark ignition conditions. *SAE International*, 2003.

[33] edit by Hua Zhao. *HCCI and CAI engines for the automotive industry*. Woodhead publishing limited, 2007.

[34] K. Epping, S. Aceves, and R. Bechtold. The potential of hcci combustion for high efficiency and low emissions. *SAE paper 2002-01-1923*, 2002.

[35] V. Eswaran and P. S. B. Direct numerical simulations of the turbulent mixing of a passive scalar. *Phys. Fluids*, 31:506–520, 1988.

[36] S. B. Fiveland and D. N. Assanis. Development of a two-zone hcci combustion model accounting for boundary layer effects. *SAE paper 2001-01-1028*, 2001.

[37] B. V. Gendenko. *The Theory of Probability*. 1962.

[38] M. D. Gerty. Effects of operating conditions, compression ratio, and fuel reformate on si engine knock limits, 2005.

[39] Glassman. *Combustion I.* Academic Press, 1977.

[40] V. Golovitchev. http://www.tfd.chalmers.se/ valeri/mech.html. Technical report.

[41] V. Golovitchev. http://www.tfd.chalmers.se/ valeri/mech.html. Technical report, 1997.

[42] V. Golovitchev. http://www.tfd.chalmers.se/ valeri/mech.html. Technical report, 2004.

[43] G. Goyal, J. Warnatz, and U. Maas. Numerical studiesof hotspot ignition in h_2-o_2 and ch_4-air mixtures. *Twenty-Third Symposium (International) of Comustion / The Combustion Institute*, pages 1767–1773, 1990.

[44] E. G. Groff and F. A. Matekunas. The nature of turbulent flame propagation in homogeneous spark-ignited engine. *SAE paper 800133*, 89, 1980.

[45] M. Gunthner. *Untersuchung der Eigenschaften und Kontrollmöglichkeiten der homogen komprissionsgezündeten Verbrennung von Ottokraftstoffen*. PhD thesis, Universität Karlsruhe, 2004.

[46] H. N. Gupta. *Fundamentals of Internal Combustion Engines*. PHI Learning, 2006.

[47] S. Haas. *Experimentelle und theoretische Untersuchun homogener und teilhomogener Dieselbrennverfahren*. PhD thesis, Institut für Verbrennungsmotoren und Kraftfahrwesen der Universität Stuttgart, 2007.

[48] H. D. Häder. *Thermodynamik*. Springer Verlag, 2000.

[49] D. C. Haworth and S. B. Pope. A generalized lagenvin model for turbulent flows. *Physics of Fluids*, 29:387–405, 1986.

[50] D. C. Haworth and S. H. E. Tahry. Probability density function approach for multidimensional turbulent flow calculations with application to in-cylinder flows in reciprocating engines. *AIAA Jour.*, 29:208, 1991.

[51] J. B. Heywood. *Internal Combustion Engine Fundamentals.* MC Graw-Hill, 1988.

[52] J. B. Heywood and F. R. Vilchis. Comparison of flame development in a spark-ignition engine fueled by propane and hydrogen. *Combust. Sci. Technol.*, 38:313–324, 1984.

[53] J. O. Hinze. *Turbulence, 2nd ed.* McGraw Hill Book Company, 1975.

[54] J. O. Hirschfelder and C. F. Curtiss. *Theory of Propagation of Flames. Part I: General Equations*, page 121. Williams and Wilkins, Baltimore, 1949.

[55] G. Hohenberg. Berechnung des gasseitigen wärmeüberganges in dieselmotoren. *MTZ*, 41, 1980.

[56] T. W. R. III and T. J. Callahan. Homogeneous charge compression ignition of diesel fuel. *SAE paper 961160*, 1996.

[57] J. Janicka, W. Kolbe, and W. Kollmann. Closure of the transport equation of the probability density function of turbulent scalar fields. *J. of Non-Equilibrium Thermodynamics*, 4:47–66, 1979.

[58] Jayesh and Z. Warhaft. Probability distribution of a passive scalar in grid-generated turbulence. *Phy. Rev. Letters*, 67:3503–3506, 1991.

[59] W. Jones and P. Musonge. Closure of the Reynolds stress and scalar flux equations. *Phys. Fluids*, 31:3589, 1989.

[60] W. P. Jones. Models for turbulent flows with variable density and combustion. In W. Kollmann, editor, *Prediction Methods for Turbulent Flows*, pages 379–421. Hemisphere Publishing Corp., Washington DC, 1980.

[61] J. L. L. K. S. Choi. *In IUTAM Symp on Turbulence and Chaotic Phenomenain Fluids*, 1983.

[62] C. J. Keck. Turbulent flame structure and speed in spark ignition engines. *Preceedings of the Nineteenth Internatiional symposium on Combustion*, The Combustion Institue:1451–1466, 1982.

[63] P. E. Kloeden and E. Platen. Numerical solution of stochastic differential equations. 48:271, 1991.

[64] W. Kovarik. Ethyl-leaded gasoline: how a classic occupational disease became an international public health disaster. *Int. J. Occup. Environ. Health*, 11:Int J Occup Environ Health, 2005.

[65] K. K. Kuo. *Principles of Combustion.* John Wiley and Sons, 1986.

[66] B. E. Launder and D. B. Spalding. The numerical computation of turbulent flows. *Computer Methods in Applied Mathematics and Engineering*, 3:169–289, 1974.

[67] B. E. Launder and D. B. Spalding. *Mathematical Models of Turbulence.* Academic Press, London, 1975.

[68] W. Lee and H. J. Schaefer. Analysis of local pressures, surface temperatures, and engine damage under knock conditions. *SAE Paper 830508*, 92, 1983.

[69] W. R. Leppard. Individiual-cyllinder knock occurance and intensity in multicylinder engines. *SAE paper 820074*, 1982.

[70] P. A. Libby and F. A. Williams, editors. *Turbulent Reacting Flows.* Academic Press, New York, 1994.

[71] S. B. P. M. S. Anand and H. C. Mongia. Pressure algorithm for elliptic flow calculations with the pdf method. *In NASA, Lewis Research Center, Computational Fluid Dynamics Symposium on Aeropropulsion*, pages 347–362, 1991.

[72] U. Maas. *Verwendung von Wahrscheinlichkeitsdichtefunktions-Methoden zur Modellierung turbulenter reaktiver Strömung.* PhD thesis, Institut für technische Verbrennung der Universität STuttgart, 1997.

[73] U. Maas and J. Warnatz. Ignition processes in hydrogen-oxygen mixtures. *Combustion and Flame*, 74:53, 1988.

[74] B. F. Magnussen and B. H. Hjertager. On mathematical models of turbulent combustion with special emphasis on soot formation and combustion. In *16*th *Symposium (International) on Combustion*, pages 719–729. The Combustion Institute, Pittsburgh, PA, 1976.

[75] O. Maiwald. *Experimentelle Untersuchungen und mathematische Modellierung von Verbrennungsprozessen in Motoren mit homogener Selbstzndung*. PhD thesis, Universität Karlsruhe, 2005.

[76] L. J. McCabe, F. B. Fitch, and H. V. Lowther. Future trends in automotive fuels and engine oils. *SAE Paper 830935*, 92:678–679, 1983.

[77] A. Monin and A. Yaglom. *Statistical Fluid Dynamics*. MIT Press, Cambridge, 1971.

[78] P. Najt and D. E. Forster. Compression ignited homogeneous charge combustion. *SAE paper 830264*, 1983.

[79] Y. Nakagawa, M. Nakai, and K. Hamai. A study of the relationship between cycle-to-cycle variations of combustion and heat release delay in spark ignition engine. *Bull. JSME*, 25 no. 199:54–60, 1982.

[80] Y. Nakajama, M. Onoda, T. Nagai, and K. Yoneda. Consideration for evaluation knock intensity. *JSAE rev.*, 9:27–35, 1982.

[81] M. Nau. *Berechnung turbulenter Diffusionsflammen mit Hilfe eines Verfahrens zur Bestimmung der Wahrscheinlichkeitsdichtefunktion und automatischer reduzierter Reaktionsmechanismen*. PhD thesis, Fakultät Energietechnik, Universität Stuttgart, 1997.

[82] M. Nau, W. Neef, U. Maas, E. Gutheil, and J. Warnatz. Computational and experimental investigation of a turbulent non-premixed methane flame. In *26*th *Symposium (International) on Combustion*, page 83. The Combustion Institute, Pittsburgh, PA, 1996.

[83] M. Nau, A. Wölfert, U. Maas, and J. Warnatz. Applications of a combined pdf/finite volume scheme on turbulent methane diffusion flames. In *Proc. 8th International Symposium on Transport Phenomena in Combustion*. San Francisco, 1995.

[84] T. V. Nguyen and S. B. Pope. Monte Carlo calculations of turbulent diffusion flames. *Combustion Science and Technology*, 42:13–45, 1984.

[85] M. Noguchi, T. Tanaka, and Y. Takeuchi. A study on gasoline engine combustion by observation of intermediate reactive products during combustion. *SAE paper 790840*, 1979.

[86] A. T. Norris and S. B. Pope. Modeling of extinction in turbulent diffusion flames by the velocity-dissipation-composition PDF method. *Combustion and Flame*, 100:211–220, 1995.

[87] J. W. Norris and J. R. Edwards. Large-eddy simulation of high-speed, turbulent diffusion flames with detailed chemistry. In *AIAA Paper 97-0370*. American Institute of Aeronautics and Astronautics, 1997.

[88] E. E. O'Brien. The probability density function (pdf) approach to reacting turbulent flows. In F. A. Williams and P. A. Libby, editors, *Turbulent Reacting Flows*, page 185. Springer Verlag, Berlin, 1980.

[89] R. Ogink. *Computer Modeling of HCCI Combustion*. PhD thesis, Chalmers University of Technology, 2005.

[90] S. Onishi, S. H. Jo, K. Shado, P. D. Jo, and S. Kato. Active thermo-atmosphere combustion (atac)- a new combustion process for internal combustion engine. *SAE paper 790501*, 1979.

[91] J. Pan and C. G. W. Sheppard. A theoritical and experimental of the modes of end gas autoignition leading to knock in s.i. engines. *SAE Paper 942060*, 1994.

[92] D. J. Patterson. Cylinder pressure variations present a fundamental combustion problem. *SAE paper 660129*, 75, 1966.

[93] T. W. J. Peeters. *Numerical modelling of turbulent natural-gas diffusion flames*. PhD thesis, Delf University of Technology, 1995.

[94] N. Peters. Laminar diffusion flamelet models in nonpremixed turbulent combustion. *Prog. Energy Combust. Sci.*, 10:319–339, 1984.

[95] N. Peters. Laminar flamelets concepts in turbulent combustion. In *21st Symposium (International) on Combustion*, page 1231. The Combustion Institute, Pittsburgh, PA, 1986.

[96] S. Pischinger. *Verbrennungsmotoren.* VKA, RWTH Aachen, 2000.

[97] W. Pitz, J. Warnatz, and C. Westbrook. Simulation of auto-ignition over a large temperature range. *Proc. Comb. Inst.*, 22:893, 1989.

[98] S. B. Pope. The probability approach to the modeling of turbulent reacting flows. *Combust. Flame*, 27:299–312, 1976.

[99] S. B. Pope. A Monte Carlo method for the PDF equations of turbulent reacting flow. *Combustion Science and Technology*, 25:159–174, 1981.

[100] S. B. Pope. Transport equation for the joint probability density function of velocity and scalars in turbulent flow. *Physics of Fluids*, 24:588–596, 1981.

[101] S. B. Pope. An improved turbulent mixing model. *Combust. Science and Technology*, 28:131–145, 1982.

[102] S. B. Pope. PDF methods for turbulent reactive flows. *Prog. Energy Combust. Sci.*, 11:119–192, 1985.

[103] S. B. Pope. Application of the velocity-dissipation PDF model to inhomogeneous turbulent flow. *Phys. Fluids A*, 3:1947–1957, 1991.

[104] S. B. Pope. *Turbulent Flows.* Cambrige University Press, 2000.

[105] S. B. Pope and Y. L. Chen. The velocity-dissipation probability density function model for turbulent flows. *Physics of Fluids A*, 2:1437–1449, 1990.

[106] W. C. Reynolds. The potential and limitions of direct and large eddy simulations. In J. L. Lumley, editor, *Whither Turbulence? Turbulence at the Crossroads*, pages 313–343. Springer-Verlag, Berlin, 1989.

[107] W. Rodi. *Turbulence Models and Their Application in Hydraulics - A State of the Art Review.* IAHR, Delft, The Netherlands, 1980.

[108] P. Ronney. *Energy and Propulsion*, 2008.

[109] R. Schiessel. *Untersuchung innermotorischer Verbrennungsprozesse mit laserinduzierter Fluoreszenz.* PhD thesis, Universität Stuttgart, 2001.

[110] D. Schmidt. *Motorische Verbrennung und Abgase.* IVK, Universität Stuttgart, 2011.

[111] H. Schulte and M. Wirth. Internal combustion engine for the future. *Ford Motor Company*.

[112] P. Siwaborworn, A. Zoweil, K. Hein, S. Shafiquzzaman, and D. Schmidt. Hybrid modelling of hcci engine combustion. Poster, 32nd Symposium on Combustion, Montreal, 2008.

[113] D. B. Spalding. Mixing and chemical reaction in steady confined turbulent flames. *The combustion institute*, 1976.

[114] G. Stahl and J. Warnatz. Numerical investigation of time-dependent properties and extinction of strained methane- and propane-air flamelets. *Combustion and Flame*, 85:285–299, 1991.

[115] R. H. Stanglmaier and C. Roberts. Homogeneous charge compression ignition (hcci): benefits, compromise, and future engine applications. *SAE paper 01-3682*, 1999.

[116] R. Stone. *Introduction to Internal Combustion Engines*. SAE, 1999.

[117] S. Subramaniam and S. B. Pope. A mixing model for turbulent reactive flows based on euclidean minimum spanning trees. *Combust. Flame*, 115:487–514, 1998.

[118] S. Tavoularis and S. Corrsin. Experiments in nearly homogeneous turbulent shear flow with a uniform mean termperature gradiant. *J. Fluid Mech.*, 104:311–347, 1981.

[119] C. F. Taylor. *The Internal Combustion Engine in Theory and Practice*. MIT Press, 1968.

[120] D. Thévenin, E. van Kalmthout, and S. Candel. In J. P. Chollet, P. R. Voke, and L. Kleiser, editors, *Direct and Large Eddy Simulation II*, pages 343–354. Kluwer Academic Publishers, 1997.

[121] H. R. Thring. Homogeneous charge compression ignition (hcci) engines. *SAE paper 892068*, 1989.

[122] H. M. und Ebenhausen. Euler- and lagrange-monte-carlo-pdf-simulation turbulenter strömungs-, mischungs, und verbrennungsvorgänge. Technical Report 414, VDI Verlag, 2001.

[123] H. K. Versteeg and W. Malalasekera, editors. *An introduction to computational fluid dynamics - The finite volume method*. Academic Press, New York, 1995.

[124] J. Warnatz, U. Maas, and R. Dibble. *Combustion*. springer, 2001.

[125] C. K. Westbrook. Chemical kinetics of hydrocarbon ignition in practical combustion systems. *Proceedings of the Combustion Institute*, 28:1563–1577, 2000.

[126] D. C. Wilcox. *Turbulence modeling for CFD*. DCW Industries Inc., 1993.

[127] H. A. Wouters. *Lagrangian models for turbulent reactive flows*. PhD thesis, Ph.D. thesis, Technical university of Delft, 1998.

[128] M. Yao, Z. Zheng, and H. Liu. Progress and recent trends in homogeneous charge compression ignition (hcci) engines. *Progress in Energy and Combustion Science*, 33:398–437, 2009.

[129] M. F. Yao, B. Zhang, and Z. Zheng. Effects of exhaust gas recirculation on combustion and emissions of a homogeneous charge compression ignition engine fueled with primary reference fuels. pages 197–213, 2007.

[130] P. K. Yeung and S. B. Pope. Lagrangian statistics from direct numerical simulation of isotropic turbulence. *J. of Fluid Mechanics*, 207:531–586, 1989.

[131] A. Zoweil, D. Schmidt, and U. Maas. Pdf simulation of auto-ignition in ic engines. Poster, 31st Symposium on Combustion, Heidelberg, 2006.

Danksagung

Mein Dank gilt allen, die mir bei der Erstellung dieser Arbeit direkt und indirekt beigestanden haben.

Mein besonderer Dank gilt dabei:

Prof. Dr. Ulrich Maas für seine Betreung und seine außerordentliche Hilfsbereitschaft in allen Fragen und auftretenden Problemen sowie für die kritische Durchsicht der Arbeit mit gewinnbringenden Vorschlägen und Anregungen.

Prof. Dr. Ulrich Spicher für das meiner Arbeit entgegengebrachte Interesse und für die Übernahme des Mitberichts.

Dr. Dietmar Schmidt für die interessanten Diskussionen, die mich auf neue Ideen und Wege brachten und für die kritische Durchsicht meiner Arbeit.

Zu guter Letzt möchte ich meiner Frau und meinen Eltern, sowie meiner ganzen Familie, danken, die mir mit außerordentlicher Hilfsbereitschaft zur Seite standen.